



AFRL-AFOSR-UK-TR-2013-0048



Active Reconfigurable Metamaterial Unit Cell Based on Non-Foster Elements

**Silvio Hrabar
Igor Krois
Ivan Bonic
Aleksandar Kiricenko
Damir Muha**

**University of Zagreb
Faculty of Electrical Engineering and Computing
Unksa 3
Zagreb, HR-10000 CROATIA**

EOARD Grant 12-2081

Report Date: October 2013

Final Report from 9 July 2012 to 8 July 2013

Distribution Statement A: Approved for public release distribution is unlimited.

**Air Force Research Laboratory
Air Force Office of Scientific Research
European Office of Aerospace Research and Development
Unit 4515 Box 14, APO AE 09421**

REPORT DOCUMENTATION PAGE

Form Approved OMB No. 0704-0188

Public reporting burden for this collection of information is estimated to average 1 hour per response, including the time for reviewing instructions, searching existing data sources, gathering and maintaining the data needed, and completing and reviewing the collection of information. Send comments regarding this burden estimate or any other aspect of this collection of information, including suggestions for reducing the burden, to Department of Defense, Washington Headquarters Services, Directorate for Information Operations and Reports (0704-0188), 1215 Jefferson Davis Highway, Suite 1204, Arlington, VA 22202-4302. Respondents should be aware that notwithstanding any other provision of law, no person shall be subject to any penalty for failing to comply with a collection of information if it does not display a currently valid OMB control number.

PLEASE DO NOT RETURN YOUR FORM TO THE ABOVE ADDRESS.

1. REPORT DATE (DD-MM-YYYY) 14 October 2013			2. REPORT TYPE Final Report	3. DATES COVERED (From – To) 9 July 2012 – 8 July 2013	
4. TITLE AND SUBTITLE Active Reconfigurable Metamaterial Unit Cell Based on Non-Foster Elements			5a. CONTRACT NUMBER FA8655-12-2081		
			5b. GRANT NUMBER Grant 12-2081		
			5c. PROGRAM ELEMENT NUMBER 61102F		
6. AUTHOR(S) Silvio Hrabar (PI) Igor Krois Ivan Bonic Aleksandar Kiricenko Damir Muha			5d. PROJECT NUMBER 5d. TASK NUMBER 5e. WORK UNIT NUMBER N/A		
7. PERFORMING ORGANIZATION NAME(S) AND ADDRESS(ES) University of Zagreb Faculty of Electrical Engineering and Computing Unska 3 Zagreb, HR-10000 CROATIA			8. PERFORMING ORGANIZATION REPORT NUMBER N/A		
9. SPONSORING/MONITORING AGENCY NAME(S) AND ADDRESS(ES) EOARD Unit 4515 APO AE 09421-4515			10. SPONSOR/MONITOR'S ACRONYM(S) AFRL/AFOSR/IOE (EOARD)		
			11. SPONSOR/MONITOR'S REPORT NUMBER(S) AFRL-AFOSR-UK-TR-2013-0048		
12. DISTRIBUTION/AVAILABILITY STATEMENT Distribution A: Approved for public release; distribution is unlimited.					
13. SUPPLEMENTARY NOTES					
14. ABSTRACT <p>Most research in metamaterials (artificially enhanced materials which modify the permittivity and permeability of electromagnetic wave propagation in order to "steer" EM waves in novel ways) involve "passive" metamaterials in a negative (permittivity and permeability less than zero) or plasmalike (permittivity and permeability between 0 and 1) regime. Unfortunately, negative and plasmalike metamaterials exhibit high dispersion of EM energy at some wavelengths, thus giving them a very narrow operating bandwidth. This research builds on the investigators' previous report showing that it is possible to overcome these dispersion-energy constraints by incorporating "non-Foster" elements (active electronic circuits employing positive feedback), with the most important goal of the project to develop an experimental demonstrator of a reconfigurable active metamaterial unit cell that can be either double-positive or epsilon (permittivity) near zero (DPS-ENZ) or either double-positive or mu (permeability) near zero (DPS-MNZ), with other goals being the increase of operating frequency to microwave region, development of "negative inductance" for MNZ/MENZ metamaterials, tunable non-Foster cells, and interfacing cells with free space for scattering applications such as cloaking. The project succeeds in understanding "negative capacitance" and its role in metamaterials, investigates the basic physics of negative non-Foster tank circuits, designs, simulates, and builds prototypes of active ultra-broadband ENZ unit cells as well as prototypes of "negative-inductor" MNZ unit cells.</p>					
15. SUBJECT TERMS EOARD, metamaterials, plasmalike metamaterials					
16. SECURITY CLASSIFICATION OF:			17. LIMITATION OF ABSTRACT SAR	18. NUMBER OF PAGES 119	19a. NAME OF RESPONSIBLE PERSON Victor Putz
a. REPORT UNCLAS	b. ABSTRACT UNCLAS	c. THIS PAGE UNCLAS			19b. TELEPHONE NUMBER (Include area code) +44 (0)1895 616021

FINAL REPORT FOR CONTRACT FA8655-12-1-2081

**Active Reconfigurable Metamaterial Unit Cell Based on
Non-Foster Elements**

by

**Silvio Hrabar
Igor Krois
Ivan Bonic
Aleksandar Kiricenko
Damir Muha**

SUBMITTED BY: Prof. Silvio Hrabar
Faculty of Electrical Engineering and Computing
University of Zagreb
Unska 3
Zagreb, HR-10000, Croatia

14 October 2013

Figure 1-1 a) A concept of volumetric metamaterial, b) A concept of transmission-line-based metamaterial	10
Figure 1-2 (a) Behavior of a fictitious dispersionless metamaterial, Solid –Epsilon-Near-Zero (ENZ) or Mu- Near-Zero (MNZ) metamaterial, Dashed - Epsilon-NeGative (ENG) or Mu–NeGative (MNG) metamaterial, (b) Behavior of realistic metamaterial with Lorentz dispersion model (ω_p and ω_s stand for angular frequencies of ‘parallel resonance’ and ‘series resonance’, respectively).....	11
Figure 1-3 Susceptances of positive (solid line) and negative (dashed line) reactive elements	12
Figure 1-4 Equivalent circuits of a differential section of different 1D ENZ metamaterials, (a) Passive ENZ metamaterial, (b) Active ENZ metamaterial developed in [66,73]	12
Figure 1-5 a) Transmission-line model of 1D active MNZ metamaterial, (b) Transmission-line model of 1D active MENZ metamaterial (C_n and L_n stand for the negative capacitor and the negative inductor, respectively).....	13
Figure 1-6 Examples 2D anisotropic active non-Foster metamaterials, a) ENZ, b) MNZ, c) MENZ	14
Figure 3-1 (a) Dispersion of a susceptance of various capacitor types. C_p (positive capacitor): solid blue curve, C_n (negative capacitor): dashed red curve. (b) Evolution of a model of negative capacitor. C_{p2} is a additional stabilizing (‘swamping’) capacitor used for ENZ effect	23
Figure 3-2 An example of the general operating principle of negative non-Foster impedance, based on a current negative impedance converter (INIC)	23
Figure 3-3 a) OpAmp-based RF negative capacitor, b) 1D ENZ metamaterial based on a transmission line loaded with three negative capacitors ([74])	24
Figure 3-4 Measurement results of an active 1D non-Foster ENZ metamaterial [74], Solid– real part, Dashed – imaginary part	25
Figure 3-5 a)Experimental realization of a low-frequency negative capacitor demonstrator, b)Simulated input capacitance, c) Simulated input conductance	28
Figure 3-6: a) Experimental integrator circuit with positive capacitor C_p and negative capacitor C_n , excited by a sinusoidal signal. b) Measured waveforms at C_p : voltage (dashed blue) and current (solid green). c) Measured waveforms at C_n : voltage (dashed blue) and current (solid green).	29
Figure 3-7: Measured waveforms on experimental integrator circuit with positive capacitor (C_p) and negative capacitor (C_n), excited by a signal with rectangular waveform a) Input voltage (doted blue), output voltage (dashed blue) for the integrator with a positive capacitor, current (solid green) that flows into the positive capacitor (C_p) b) Input voltage (doted blue), output voltage (dashed blue), the current that flows into positive capacitor C_p (C_p solid green) and current that flows out from the negative capacitance C_n (dotted red).....	30
Figure 3-8 a) Experimental circuit for investigation of negative capacitance boosting phenomenon b) Measured input voltage (doted blue), output voltage (dashed blue) for integrator with a positive capacitor, current (solid green) that flows into the positive capacitor (C_p) c) Measured input voltage (dotted blue), output voltage (dashed blue,), the voltage on negative capacitor C_n (dot- dashed), the current through the positive capacitor C_p (solid green) and the current that flows out from the negative capacitance C_n (dotted red).....	31
Figure 3-9 Values of negative capacitance extracted from the time-domain measurements. Dots (blue): raw data, Dotted green curve: 4 th order polynomial fit	32

Figure 3-10 Phasor diagram for a negative capacitor. a) ideal case with zero-valued time delay (there is no phase shift in dependent voltage source) b) realistic case with finite time delay (there is a phase shift in dependent voltage source)	33
Figure 3-11 One-pole analysis a) Equivalent input conductance G , b) Equivalent input capacitance C_n , c) Equivalent input capacitance C_n plotted in logarithmic scale that prompts a flat frequency response across wide bandwidth. ($fp_1 = 250$ kHz)	34
Figure 3-12 Two-pole analysis a) Equivalent input conductance G_n , b) Equivalent input capacitance C_n , c) Equivalent input capacitance C_n plotted in logarithmic scale that prompts a flat frequency response across wide bandwidth. ($fp_1 = 250$ kHz, $fp_2 = 1$ MHz)	35
Figure 3-13 Three -pole analysis a) Equivalent input conductance G_n , b) Equivalent input capacitance C_n ($fp_1 = 250$ kHz, $fp_2 = 1$ MHz, $fp_3 = 3$ MHz)	36
Figure 3-14 Results of SPICE simulation of input impedance of LM1875-based negative capacitor a) equivalent input conductance G_n , b) equivalent input capacitance C_n	36
Figure 3-15 The 'boosting' of the negative capacitance. a) G_n and C_n of a 'boosted' negative capacitor , b) G_n and C_n of a 'regular' negative capacitor	37
Figure 3-17 (a) Measured capacitance and conductance of the negative capacitor (low frequency demonstrator) with connected 'swamping' positive capacitor C_p (b) Extracted values of the input capacitance and input conductance for low-frequency demonstrator	38
Figure 3-16 Measured capacitance and conductance of the 'swamping' positive capacitor C_p	38
Figure 3-18 Measurements in the frequency-domain, (a) Experimental set-up (b) Extracted effective permittivity (real part: solid-blue, imaginary part: dashed-red) ,(c) Extracted index of refraction (real part-solid-blue, imaginary part: dashed-red, the lossless approximation: dotted-black), (d) Extracted phase velocity (dashed-red) and the group velocity (solid-blue) [80].	41
Figure 3-19 Measurements in time-domain, (a) Experimental set-up (b) Time-domain waveforms, (input signal: dashed-black, output signal with ENZ off: dashed-blue, output signal with ENZ on: solid-red), (c) FFT spectra (input signal: dashed-black, output signal with ENZ off: dotted -blue, output signal with ENZ on: solid-red).[80]	43
Figure 3-21 Input impedance of an ordinary (positive) series RLC circuit, (blue: R, magenta: X)	45
Figure 3-20 Ordinary (positive) series RLC circuit driven by a generator with positive internal resistance	45
Figure 3-22 An idea of a stable negative non-Foster RLC circuit driven by a generator	46
Figure 3-23 Input impedance of a stable negative non-Foster RLC circuit, (blue: R, magenta: X)	46
Figure 3-24 a) Circuit diagram of the negative non-Foster RLC circuit b) - Photograph of the manufactured negative non-Foster RLC circuit	48
Figure 3-25 , (a) – Measured imaginary part of the impedance of the negative RLC circuit (b) - Measured real part of the impedance of negative RLC circuit	49
Figure 4-1 Circuit diagram of the initially designed negative capacitor demonstrator (100 kHz – 450 MHz)	54
Figure 4-2 PCB layout of the initially designed negative capacitor demonstrator (100 kHz – 450 MHz)	55
Figure 4-3 Photograph of the initially designed negative capacitor demonstrator (100 kHz – 450 MHz)	55
Figure 4-4 Circuit diagram of the initially designed negative capacitor demonstrator (100 kHz – 450 MHz) with parasitic effects included	56
Figure 4-5 Measurements of the initially designed negative capacitor demonstrator a) generated capacitance (solid black – simulations, dashed red - measurements) (measured	

with an ZVA 40VNA) b) generated capacitance (solid black – simulations, dashed red - measurements) (measured with the help of an ZVL 8 VNA) c) generated conductance (solid black – simulations, dashed red - measurements) (measured with an ZVL 8 VNA)	57
Figure 4-6 Circuit diagram of the improved design of the negative capacitor demonstrator (100 kHz – 700 MHz) with included parasitic effects	58
Figure 4-7 PCB layout of the improved design of the negative capacitor demonstrator (100 kHz – 700 MHz)	58
Figure 4-8 Measurements of the improved design of the negative capacitor demonstrator a) generated capacitance (solid black – simulations, dashed red - measurements) (measured by an ZVA 40 VNA) b) generated capacitance (solid black – simulations, dashed red - measurements) (measured with the help of an ZVL 8 VNA) c) generated conductance (solid black – simulations, dashed red - measurements) (measured with an ZVL 8 VNA)	59
Figure 4-10 Simulated input impedance of the Kolev’s circuit, a): imaginary part , b) real part	61
Figure 4-9 Kolev-Meunier’s circuit	61
Figure 4-11 Simulated negative inductance of the Kolev’s circuit	62
Figure 4-12 Schematic diagram of the manufactured prototype of a negative inductor circuit based on Kolev’s topology	62
Figure 4-13 Photograph of the manufactured prototype	63
Figure 4-14 Measurements of the reflection coefficient of the Kolev’s circuit. Blue: the stabilizing inductor 39 nH, red: the circuit shunted with the stabilizing inductor, magenta: de-embedded reflection coefficient)	64
Figure 4-15 Input impedance of the measured negative inductance circuit.....	64
Figure 4-16 Real and imaginary part of the input impedance of the Kolev’s circuit.....	65
Figure 4-17 Simulated and measured equivalent inductance.....	65
Figure 4-18 Realistic equivalent circuit of the manufactured negative inductor	66
Figure 4-19 Imaginary part of the input impedance. Blue: calculation from the equivalent circuit , red: measurements	66
Figure 4-20 Realistic negative inductor L with a series positive inductor L_1	67
Figure 4-21 Poles of the manufactured negative inductor L_2 with a series positive inductor L_1	67
Figure 4-22 A realistic negative inductor L_2 with a parallel positive inductor L_1	68
Figure 4-23 Loci of poles of a manufactured negative inductor L_2 shunted with a positive inductor L_1	68
Figure 4-24 OPAMP transconductance amplifier circuit as a replacement for a MOSFET device	69
Figure 4-26 AC equivalent circuit of the designed negative inductance	70
Figure 4-25 The response of the transconductance amplifier	70
Figure 4-27 Designed negative inductance circuit based on four OPamps	71
Figure 4-28 Simulated S_{11} of the negative inductance circuit based on four OPamps	71
Figure 4-29 Simulated input impedance of the negative inductance circuit based on four OPamps. a) imaginary part, b) real part.....	72
Figure 4-30 Simulated equivalent negative inductance	72
Figure 4-31 The prototype of the negative inductance circuit based on four OPamps	73
Figure 4-32 Measured S_{11} of the negative inductance circuit based on four OPamps. Blue: circuit power off, red: circuit power on, magenta: de-embedded S_{11} , circuit power on). ..	73
Figure 4-33 De-embedded inductance and resistance of the negative inductance circuit based on four OPamps. a) inductance, b) resistance	73

Figure 4-34 Circuit diagram of the design of the negative inductance demonstrator (100 kHz – 700 MHz).....	74
Figure 4-35 Photograph of the design of the negative inductance demonstrator (100 kHz – 700 MHz).....	75
Figure 4-36 Measurements of the design of the negative inductance demonstrator a) generated inductance (solid black – simulations, dashed red - measurements) (measured with the help of an ZVL 8 VNA) b) generated resistance (solid black – simulations, dashed red - measurements) (measured with the help of an ZVL 8 VNA).....	76
Figure 4-37 Tuning of the negative capacitance: Method I	77
Figure 4-38 Achieved range of the equivalent permittivity: Method I	78
Figure 4-39 Tuning of the negative capacitance: Method II.....	78
Figure 4-40 Achieved range of the equivalent permittivity: Method II.....	79
Figure 4-41 Tuning of the negative capacitance: Method III	79
Figure 4-42 Achieved range of the equivalent permittivity: Method III	80
Figure 4-43 Tuning of the negative inductance	80
Figure 4-44 Achieved range of the equivalent permeability.....	80
Figure 4-45 Circuit diagram of the AD8099 based tunable negative capacitor.....	81
Figure 4-46 Simulated input capacitance of the AD8099 based tunable negative capacitor ..	82
Figure 4-47 Measured net capacitance of the AD8099 based tunable negative capacitor	82
Figure 4-48 Measured input resistance of the AD8099 based tunable negative capacitor (the DC bias is varied, red: 0V, blue: 5V, green: 10V)	83
Figure 4-49 Circuit diagram of the tunable negative capacitor (100 kHz – 700 MHz) with parasitic effects included	84
Figure 4-50 Simulations of the tunable negative capacitor ($V_{BIAS} = 10$ V) a) generated capacitance b) generated conductance.....	85
Figure 4-51 Simulations of the tunable negative capacitor ($V_{BIAS} = 7$ V) a) generated capacitance b) generated conductance.....	86
Figure 4-52 Simulations of the tunable negative capacitor ($V_{BIAS} = 5$ V) a) generated capacitance b) generated conductance.....	87
Figure 4-53 Simulations of the tunable negative capacitor ($V_{BIAS} = 4$ V) a) generated capacitance b) generated conductance.....	88
Figure 4-54 Simulations of the tunable negative capacitor ($V_{BIAS} = 3$ V) a) generated capacitance b) generated conductance.....	89
Figure 4-55 Simulations of the tunable negative capacitor ($V_{BIAS} = 2$ V) a) generated capacitance b) generated conductance.....	90
Figure 4-56 Circuit diagram of the tunable negative inductor (100 kHz – 700 MHz)	92
Figure 4-57 The photograph of the tunable negative inductor (100 kHz – 700 MHz)	92
Figure 4-58 Measurements of tunable negative inductor ($V_{BIAS} = 0.8$ V) a) generated inductance (solid black – simulations, dashed red - measurements) b) generated resistance (solid black – simulations, dashed red - measurements)	93
Figure 4-59 Measurements of tunable negative inductot ($V_{BIAS} = 1$ V) a) generated inductance (solid black – simulations, dashed red - measurements) b) generated resistance (solid black – simulations, dashed red - measurements)	94
Figure 4-60 Measurements of tunable negative inductot ($V_{BIAS} = 2$ V) a) generated inductance (solid black – simulations, dashed red - measurements) b) generated resistance (solid black – simulations, dashed red - measurements)	95
Figure 4-61 Measurements of tunable negative inductot ($V_{BIAS} = 3$ V) a) generated inductance (solid black – simulations, dashed red - measurements) b) generated resistance (solid black – simulations, dashed red - measurements)	96

Figure 4-62 Measurements of tunable negative inductot ($V_{BIAS} = 4$ V) a) generated inductance (solid black – simulations, dashed red - measurements) b) generated resistance (solid black – simulations, dashed red - measurements)	97
Figure 4-63 Measurements of tunable negative inductot ($V_{BIAS} = 5$ V) a) generated inductance (solid black – simulations, dashed red - measurements) b) generated resistance (solid black – simulations, dashed red - measurements)	98
Figure 4-64 Floating NIC with two FET's.....	100
Figure 4-65 A simplified circuit of CMOS negative capacitor.....	101
Figure 4-66 Simulated input capacitance of a CMOS negative capacitor (green; $C=-10$ pF, blue; $C=-5.5$ pF, red $C=-1$ pF).....	101
Figure 4-67 Simulated input capacitance of a CMOS negative capacitor (green; $5x(-1$ pF), blue; green; $10x(-0.5$ pF), red green; $50x(-0.5$ pF).....	102
Figure 4-68 Interfacing of the transmission-line non-Foster metamaterial with free-space via ‘antenna’ layer	103
Figure 4-69 Stacking the transmission line non-Foster metamaterials with ‘flarings’	104
Figure 4-70 An idea of $2 \frac{1}{2}$ D non-Foster metamaterial	104
Figure 4-71 The bandwidth comparison between a passive cloak and a cloak based on non-Foster metamaterials.....	105
Table 3-1 Stability criteria for driven positive/negative LC tank circuit [73]	44

TABLE OF CONTENTS

CHAPTER 1 INTRODUCTION	9
CHAPTER 2 PROJECT OBJECTIVE AND REALIZED OUTCOMES.....	16
CHAPTER 3 BACKGROUND PHYSICS OF PRACTICAL NON-FOSTER METAMATERIALS	21
3.1. PREVIOUS WORK: THE UNCLEAR ISSUES OF PHYSICS OF NON-FOSTER ELEMENTS.....	22
3.2. INVESTIGATION OF BASIC PHYSICS OF NEGATIVE CAPACITOR IN TIME DOMAIN.....	27
3.2.1 <i>Construction and initial testing of a low-frequency demonstrator.....</i>	27
3.2.2 <i>Direct observation of negative capacitance</i>	28
3.2.3 <i>Capacitance decrease phenomenon (ENZ phenomenon).....</i>	29
3.2.4 <i>Negative capacitance boosting phenomenon</i>	30
3.3. IMPROVEMENT OF MODEL OF NEGATIVE CAPACITOR.....	32
3.3.1 <i>One-pole model of the negative capacitor.....</i>	33
3.3.2 <i>Two-pole model of the negative capacitor</i>	35
3.3.3 <i>Three-pole model of the negative capacitor</i>	36
3.4. PHENOMENON OF SIMULTANEOUS SUPERLUMINAL PHASE AND GROUP VELOCITIES	39
3.4.1 <i>Investigation in frequency domain</i>	39
3.4.2 <i>Investigation in time domain</i>	42
3.5 FEASIBILITY OF NON-FOSTER ENG/MNG METAMATERIAL	44
3.5.1 <i>An idea of stable negative RLC tank circuit</i>	46
3.5.2 <i>Negative RLC tank circuit RF demonstrator</i>	47
3.5. SUMMARY.....	50
CHAPTER 4 TOWARDS MORE VERSATILE NON-FOSTER METAMATERIALS	51
4.1 PREVIOUS WORK: TECHNOLOGICAL CONSTRAINTS OF STATE-OF-THE ART NON-FOSTER METAMATERIALS	52
4.2 INCREASE OF THE MAXIMAL OPERATING FREQUENCY: NEGATIVE CAPACITOR DEMONSTRATOR	54
4.2.1. <i>Initial design based on OpAmp(100 kHz - 450 MHZ).....</i>	54
4.2.2. <i>Improved design based on OpAmp (100 kHz - 700 MHZ)</i>	58
4.2.3. <i>The ENZ unit cell.....</i>	60
4.3 INCREASE OF THE MAXIMAL OPERATING FREQUENCY: NEGATIVE INDUCTOR DEMONSTRATOR.....	60
4.3.1 <i>Design based on Kolev's circuit with FETs (1 MHz – 50 MHz)</i>	60
4.3.2. <i>Design based on Kolev's circuit with OPamps (1 MHz – 10 MHz).....</i>	69
4.3.3. <i>Design based on an Opamp (100 kHz - 700 MHz).....</i>	74
4.3.4. <i>The MNZ unit cell.....</i>	76
4.4. ADDING TUNEABILITY/RECONFIGURABILITY FEATURE.....	77
4.4.1. <i>Basic ideas.....</i>	77
4.4.2. <i>OP-amp-based tunable negative capacitor (1 MHz- 40 MHz).....</i>	81
4.4.3. <i>OP-amp-based tunable negative capacitor (100 kHz- 700 MHz)</i>	83
4.4.4. <i>OP-amp-based tunable negative inductor (100 kHz- 700 MHz).....</i>	91
4.4.5. <i>Tunable/reconfigurable DPS-ENZ and DPS-MNZ unit cells.....</i>	99
4.5. TOWARDS A MICROELECTRONIC NON-FOSTER METAMATERIAL UNIT CELL.....	99
4.6. TOWARDS VOLUMETRIC NON-FOSTER METAMATERIALS INTERFACED TO FREE- SPACE	102
4.7. SUMMARY.....	105
CHAPTER 5 CONCLUSIONS AND FUTURE WORK.....	107
CHAPTER 6 BIBLIOGRAPHY.....	110

Chapter 1 INTRODUCTION

Introduction

Metamaterials are artificial structures, engineered to provide unusual electromagnetic properties not found in naturally occurring materials. There are two common design strategies: the volumetric metamaterials and the transmission line metamaterials.

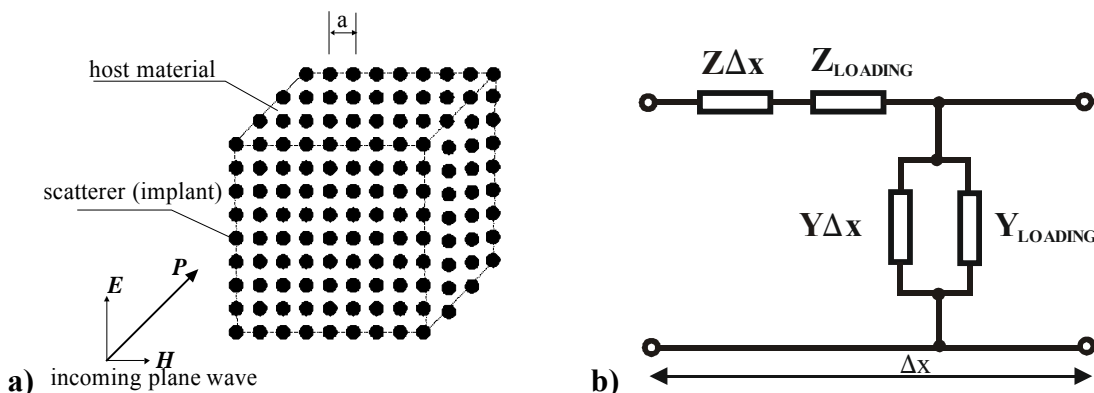


Figure 1-1 a) A concept of volumetric metamaterial, **b)** A concept of transmission-line-based metamaterial

Volumetric metamaterials (Figure 1-1(a)) are based on an array of electrically small electromagnetic scatterers (inclusions) embedded into a dielectric host material, at mutual distance that is a small fraction of the wavelength. If an electromagnetic (EM) wave impinges on this structure, all the local fields scattered from the particular inclusions will change the original field distribution. This process is, in principle, very similar to the mechanism of electric or magnetic polarization in ordinary, continuous materials. Therefore, the structure behaves as a hypothetical continuous material with new (homogenized) values of constitutive parameters (permittivity ϵ and permeability μ). These values are *generally different* from the parameters of the host material and the inclusions. In this way, it is possible to obtain the permittivity and permeability values that are not available in Nature.

The second approach in construction of metamaterials uses an ordinary transmission line that is periodically loaded with series and/or shunt lumped reactive elements (Figure 1-1(b)). If the mutual distance between the loading elements is much smaller than the wavelength, the additional reactive elements modify the distributed impedance and

admittance (and therefore, effective permeability and effective permittivity). This is the main idea of the so-called transmission-line metamaterials. Furthermore, it is possible to extend this simple approach to 2D metamaterials [66].

There are several classes of metamaterial. Apart from familiar **Double-Positive** materials (**DPS**), there are also materials with **Single-Negative** (**SNG**) and **Single-Near-Zero** (**SNZ**) behavior. This class comprises **Epsilon-Negative** (**ENG**) and **Mu-Negative** (**MNG**) materials, as well as **Epsilon-Near-Zero** (**ENZ**) and **Mu-Near-Zero** (**MNZ**). Finally, there are also classes of **Double-Negative** (**DNG**) and **Double-Near-Zero** (**DNZ**) or **Mu-and-Epsilon-Near-Zero** (**MENZ**) metamaterials [1-4].

The majority of proposed applications of metamaterials are based on ‘negative’ ($\epsilon_r < 0$, $\mu_r < 0$, i.e. ENG, MNG, DNG) or ‘plasma-like’ ($0 < \epsilon_r < 1$, $0 < \mu_r < 1$, i.e. ENZ, MNZ) metamaterials (ϵ_r and μ_r being relative permittivity and permeability, respectively) [5-15]. It would be very convenient if these metamaterials were dispersionless and, therefore, of broadband nature (Figure 1-2 (a)). However, it is well known that all ‘negative’ and ‘plasma-like’ metamaterials exhibit pronounced dispersion (Figure 1-2 (b)), accompanied with a narrow operating bandwidth [16]. This is the inherent drawback of all known passive metamaterials, which is critical in many applications. A typical example is the anisotropic cloak, in which the dispersion limits the fractional operating bandwidth to a value smaller than 1% [12-14].

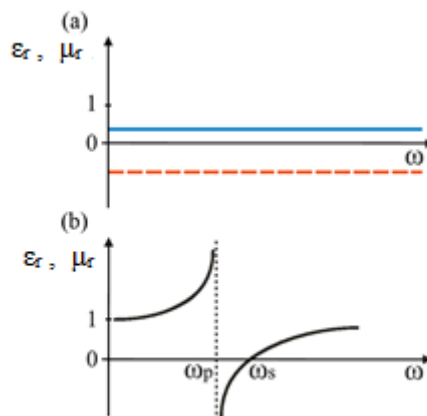


Figure 1-2 (a) Behavior of a fictitious dispersionless metamaterial, **Solid** –Epsilon-Near-Zero (ENZ) or Mu-Near-Zero (MNZ) metamaterial, **Dashed** - Epsilon-NeGative (ENG) or Mu-NeGative (MNG) metamaterial, **(b)** Behavior of realistic metamaterial with Lorentz dispersion model (ω_p and ω_s stand for angular frequencies of ‘parallel resonance’ and ‘series resonance’, respectively).

Pronounced dispersion of any passive material, relative constitutive parameters of which are smaller than one is a very basic issue associated with causality i.e. with dispersion constraints [6,7], that are valid for any material (or metamaterial)[16]:

$$\frac{\partial[\epsilon_r(\omega)]}{\partial\omega} > 0, \quad \frac{\partial[\mu_r(\omega)]}{\partial\omega} > 0. \quad (1.1)$$

Here, ϵ_r and μ_r are relative permittivity and permeability, respectively. The circuit theory analogue of (1.1) is Foster’s reactance theorem [17]:

$$\frac{\partial[X(\omega)]}{\partial\omega} > 0, \quad \frac{\partial[B(\omega)]}{\partial\omega} > 0. \quad (1.2)$$

Here, X and B stand for the reactance and susceptance, respectively.

In our recent report (Broadband Epsilon-Near-Zero (ENZ) and Mu-Near-Zero (MNZ) Active Metamaterial, FA 8655-10-1-3030, EOARD and AFRL, August 2011 [73]) we showed that it is possible to overcome the basic dispersion-energy constraints (and, therefore, to overcome the inherent narrowband operation) of passive metamaterials by incorporation of the so-called non-Foster elements into standard transmission-line-based structures. Non-Foster elements are actually electronic circuits. These circuits employ positive feedback and generate either negative capacitance or negative inductance that violate Foster's theorem [25-47]. The susceptances of these 'negative' elements read:

$$B_{L_n} = -j \frac{1}{\omega L_n} = +j \frac{1}{\omega |L_n|}, \quad B_{\bar{C}} = j\omega C_n = -j\omega |C_n|. \quad (1.3)$$

The dispersion curves of negative elements are inverse to their counterparts of the ordinary elements (Figure 1-3)

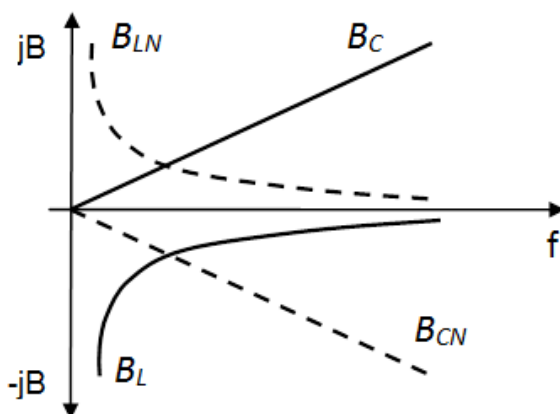


Figure 1-3 Susceptances of positive (solid line) and negative (dashed line) reactive elements

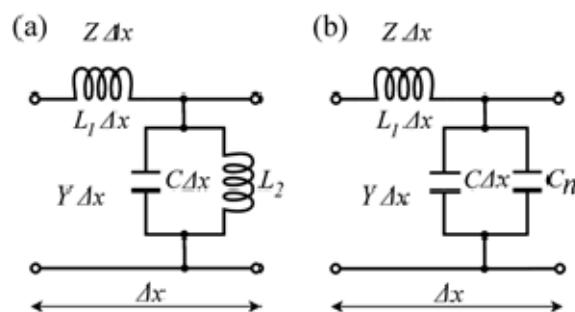


Figure 1-4 Equivalent circuits of a differential section of different 1D ENZ metamaterials, (a) Passive ENZ metamaterial, (b) Active ENZ metamaterial developed in [66,73]

The basic principle of non-Foster metamaterial is briefly explained in Figure 1-4. A typical one-dimensional (1D) implementation of an ENZ (or ENG) metamaterial uses a transmission line periodically loaded with lumped inductances (Figure 1-4 (a)). Here, Z and Y stand for the distributed impedance and admittance of the line, respectively. This equivalent circuit describes a well-known wire medium [5]. The resonator in Figure 1-4 (a) is actually a tank circuit formed by the line shunt capacitance $C\Delta x$ (C being the distributed capacitance

and Δx being the line segment length) and the lumped inductor L_2 . This circuit obeys the Drude dispersion model (i.e. Lorentz model with $\omega_p=0$, Figure 1-2):

$$\varepsilon_r(\omega) = \left[\frac{1}{\varepsilon_0} \left(C - \frac{1}{\omega^2 L_2 \Delta x} \right) \right]. \quad (1.4)$$

Within the narrow band above the resonant frequency, the expression in square brackets in (1.4) has a value smaller than one, which shows the ENZ behavior ($0 < \varepsilon_r < 1$). It is important to stress that all known passive metamaterials (Split-Ring-Resonator-based [2,3], wire-based [8], Complementary-Split-Ring-Resonator-based [4], transmission-line-based [3], ‘fishnet’-based [10] etc.) behave very similarly and, inevitably, also exhibit dispersion.

In [66,73] we proposed a novel equivalent circuit of an active non-Foster metamaterial (Figure 1-4 (b)). It is rather similar to that of a passive metamaterial (Figure 1-4 (a)). The important difference is that the lumped inductor L_2 is replaced with an artificial *negative* capacitor C_N ($C_N < 0$) (as mentioned before, this is actually an electronic circuit that employs positive feedback and generate negative capacitance [30]). A new CC_N ‘tank circuit’ in Figure 1-4 (b) does not have the usual resonant behavior and the equivalent permittivity is *not dependent* on the frequency:

$$\varepsilon_r(\omega) = \left[\frac{1}{\varepsilon_0} \left(C - \frac{|C_N|}{\Delta x} \right) \right]. \quad (1.5)$$

Thus, if $(|C_N|/\Delta x) < C$, the equivalent permittivity will show an ENZ behavior ($0 < \varepsilon_r < 1$) that is entirely dispersionless.

In [66] we have developed several negative capacitors in 2-40 MHZ RF range, in 50-100 MHz RF range and in 1-2 GHz microwave range with appropriate 1D and 2D ENZ unit cells, extracted effective permittivity and verified broadband operation. We have also developed an entire three-cell 1D active ENZ metamaterial that has a fractional dispersion bandwidth of 200% (more than four octaves). In addition, this line supports counter-intuitive superluminal phase and group velocities [73,80,81]. All of the prototypes were ‘hand-crafted’ and based on low-cost FET, BJT and OPAMP components. Achieved bandwidth varied from one octave (1-2 GHz) to more than four octaves (2-40 MHZ). This is significantly better than the bandwidth of *any* passive metamaterial available at present and, to the best of our knowledge, this is the first experimental demonstration of a non-Foster broadband, dispersion-less ENZ metamaterial. In addition, in [73] a possible extension of this approach to MNZ and MENZ metamaterials was highlighted (Figure 1-5).

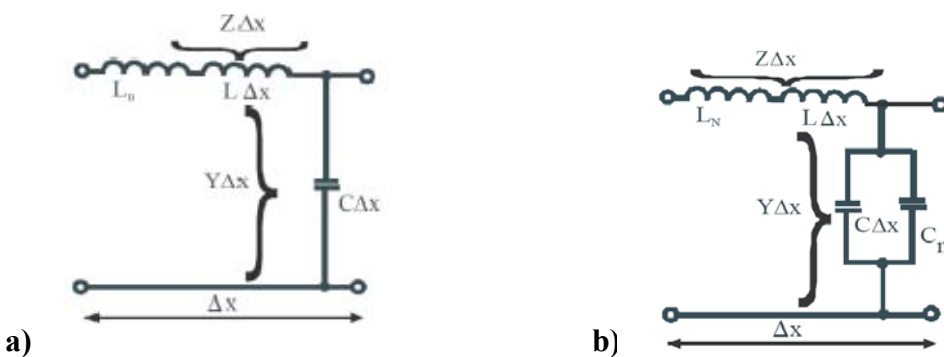


Figure 1-5 **a)** Transmission-line model of 1D active MNZ metamaterial, **(b)** Transmission-line model of 1D active MENZ metamaterial (C_n and L_n stand for the negative capacitor and the negative inductor, respectively).

The basic idea of a non-Foster MNZ metamaterial is very similar to the previously explained ENZ case. Instead of a shunt negative capacitor, one uses a series negative inductor that decreases the distributed inductance, and therefore, decreases the effective permeability below the free-space value:

$$\mu_{ref} = \frac{1}{\mu_0} (L_1 \Delta x - |L_n|) \quad (1.6)$$

In the previous report [73], we have also proposed a possible extension to, both the isotropic and the anisotropic, 2D non-Foster metamaterials (Figure 1-6). The unit cells of such metamaterials are based on two orthogonal branches with series inductances. By varying these inductances one can adjust needed values of the (positive) permeability in the x and y directions, respectively. Similarly, the shunt susceptance contains a negative capacitor (connected in parallel with a distributed capacitance of the transmission line assuring ENZ behavior).

The isotropic versions of the above mentioned active metamaterials are simply constructed by selecting identical values of the inductances in the x and y branches.

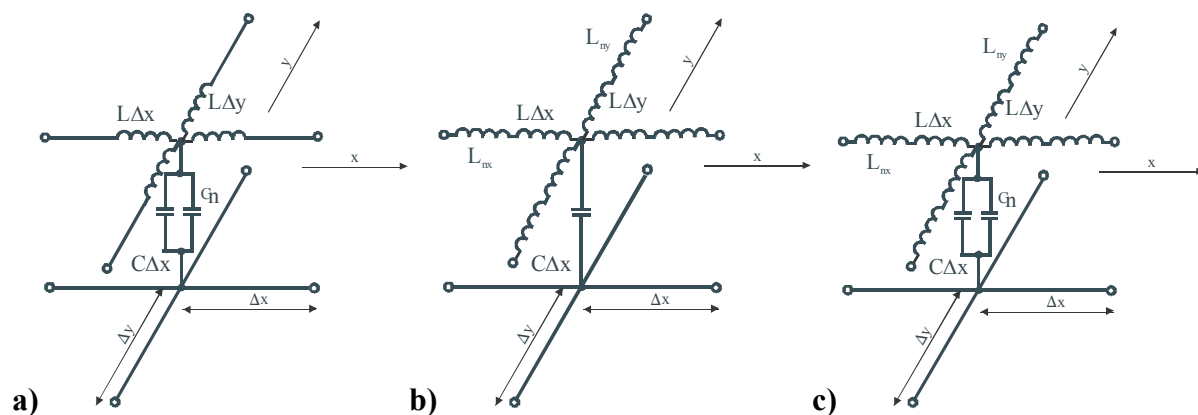


Figure 1-6 Examples 2D anisotropic active non-Foster metamaterials, a) ENZ, b) MNZ, c) MENZ

It is worth mentioning that the results published in our previous report [73], and subsequent publications [74-83], significantly enhanced the interest in this new field. Now, there are several research groups that actively work in the field of non-Foster metamaterials with proposals of novel applications such as squint-free leaky-wave antennas [100], broadband PMC surfaces [99] and many others.

Shortly, the study in [73] yielded novel and promising results but several important questions remain opened:

1. Is it possible to increase the operating frequency into microwave region by use of microelectronic technology?
2. Is it possible to develop a negative inductance needed for proposed anisotropic MNZ and MENZ metamaterials?
3. Is it possible to develop a non-Foster unit cell that is tunable (with possible adjustment of the generated negative capacitance/inductance i.e. the permittivity/permeability to a desired value by an external DC control signal)?

4. Is it possible to develop a ‘universal’ non-Foster unit cell that is in-situ reconfigurable (in order to obtain either DPS-ENZ or DPS-MNZ behavior by external DC control signal)?
5. Is it possible to interface these unit cells (and associated metamaterial structures) with free-space for possible scattering applications (e.g. cloaking)?

The purpose of the project is, therefore, to provide further insight into issues presented above by analytical, numerical and experimental investigation. The most important goal is the development of an experimental demonstrator of a tunable/reconfigurable DPS-ENZ and DPS-MNZ unit cell operating in the RF band. Finally, a route towards the microelectronic realization, that should extend the operating frequency into the microwave regime, is proposed.

Chapter 2 PROJECT OBJECTIVE AND REALIZED OUTCOMES

Project objective and realized outcomes

In our recent report (Broadband Epsilon-Near-Zero (ENZ) and Mu-Near-Zero (MNZ) Active Metamaterial, FA 8655-10-1-3030, EOARD and AFRL, August 2011 [73]) we showed that it is possible to overcome the basic dispersion-energy constraints (and, therefore, to overcome inherent narrowband operation) of passive metamaterials by incorporation of non-Foster elements into standard transmission-line-based structures. Indeed, the measurements of developed active metamaterials revealed almost dispersionless ultra-broad bandwidth of more than four octaves [73,74]. This bandwidth is considerably wider than the bandwidth of *all passive ENZ metamaterials* available at present and this clearly proves the correctness of the proposed novel concept. All experiments in [73] were limited to a maximal operating frequency that lied either in low RF range (up to 100 MHz) or in low microwave range (up to 2 GHz). Maximal frequency was limited by available fabrication facilities at University of Zagreb that include only discrete technology and not microelectronic processing. Therefore, investigation of possible extension of basic concepts of non-Foster metamaterials into UHF or even microwave region has not been attempted so far.

In this project, we have extended the frequency of operation into UHF region and, at the same time, increased the versatility of non-Foster-element-based metamaterials. It was done by the development of specially designed reconfigurable unit cell. This unit cell is *in-situ* reconfigurable (by external DC control signal) and able to achieve either DPS-ENZ or DPS-MNZ behavior. Using this novel approach, the same unit cell could be inserted into various transmission-line-based structures and (depending on its configuration) enable different applications such as: cloaking, leaky-wave antennas, artificial DB [94-96] or PMC surfaces [99], broadband phase shifters e.t.c.

The work in the project has been divided in the following tasks:

1. Development of a realistic model of negative non-Foster capacitor and associated active ENZ metamaterial. This model should be capable of both qualitative and quantitative prediction of capacitor behavior (an ideal, dispersionless loss-free model used in our previous study [73] was able to qualitatively predict only basic physical phenomena). The new model is verified by measurements on the low-frequency demonstrator (prototype), in both frequency and time domain.
2. Development of a negative capacitor with maximal operating frequency that lies in the UHF frequency band. Developed negative capacitor has been equipped with external

elements forming a unit cell of active non-Foster ENZ metamaterial. Since the microelectronic technology is not available at University of Zagreb, we opted for the realization based the best commercially available discrete off-the-shelf components (ultra-high-speed operational amplifiers).

3. Development of a non-Foster negative inductor. In our previous project [73], an RF negative capacitor (and associated ENZ metamaterial), operating in 2MHz-40MHz band, was successfully developed and tested. In [73], it was noted that the availability of a negative inductor would be needed for construction of practical active MNZ non-Foster metamaterial. Therefore, here we investigate the feasibility of construction of stable negative inductor by a two-stage process. In the first step, the selection of the most appropriate topology is done and the basic idea is proven by construction of a low-frequency RF demonstrator. In the second step, the fabrication and the measurement of the improved UHF version of the negative inductor, (based on the most advanced commercially available OPamp), is performed.
4. Adding tuneability/reconfigurability features to the developed negative capacitors/inductors and to the unit cells of associated metamaterials. It is done by the investigation of possible methods of tuning based on commercial varactors and PIN diodes. The associated prototypes of unit cells of ENZ/MNZ metamaterials are designed, manufactured and tested.

The main realized outcomes of the project are:

- We have improved understanding of the basic physics of a negative capacitance phenomenon by the analysis of a response of a negative capacitor to the pulse excitation. Towards this end, we have developed a low-frequency laboratory demonstrator based on a commercial integrated audio amplifier. Developed model generates large negative capacitance (-1.2 μ F to -0.6 μ F in the frequency range from 1 kHz-25 kHz). Such large values of negative capacitance bypasses the problem of oscilloscope input capacitance and enable direct measurements in the time domain. All the measurements show that a negative capacitor could be interpreted as a generator/sink. Generator/sink helps in charging/discharging of the external additional positive capacitor. This process alters the overall value of capacitance and leads to the ENZ behavior.
- We have improved the analysis of stability of negative-capacitor-based metamaterials. The previous approach developed in [73] used a very simple dispersionless model of a negative capacitor that is not causal. We have developed a more realistic one-pole, two-pole and three-pole models of a dispersive negative capacitor [97]. Developed model showed very good agreement with both SPICE-based simulations and the measurements on the manufactured prototypes across the whole operating bandwidth.
- We have performed a detailed experimental investigation of recently observed simultaneous superluminal phase and group velocities in non-Foster ENZ metamaterials [73,80] and found that, although being counter-intuitive, this behavior is in a perfect agreement with causality requirements. Simply, the group velocity is not equal to the energy velocity. The concept of group velocity covers the components of the input signal present only in the steady state condition. However, the spectrum will never be finite in the transient state (the switching-on phase of the generator). In the transient state, there is always a fraction of energy (however, small it is) that lies

outside the operating band and it travels with the speed of light, preserving the causality.

- We have investigated the basic physics of negative non-Foster RLC tank circuit. A simple analytical study revealed that this circuit is stable if it is driven by a generator, internal resistance of which is smaller than the absolute value of negative resistance in the non-Foster RLC tank circuit. We have manufactured the experimental prototype operating in the lower RF region (up to 70 MHz) and the measurements of input reflection coefficient indeed showed a stable behavior. To the best of our knowledge, this is the first experimental demonstration of stable negative RLC tank circuit.
- We have analyzed the feasibility of increase of the highest operating frequency of a non-Foster ENZ metamaterial towards UHF and microwave parts of the EM spectrum. We have designed, simulated and built the prototypes of the active ultra-broadband non-Foster ENZ unit cells that operate from 1 MHz to 700 MHz. This bandwidth (1:700 or more than 9 octaves) surpasses the bandwidth of all passive and active metamaterials available at the present state of the art. The main part of the developed unit cell is a negative capacitor based on a commercial ultra-fast OPamp or on an integrated gain-block with modified feedback. Developed negative capacitor generates a capacitance of -5 pF with negligible losses (the losses are an order of magnitude lower than those in [73]) across the whole bandwidth. We believe that the achieved bandwidth can be hardly improved further without switching to the microelectronic technology (specially designed MMICs).
- We have analyzed a feasibility of construction of a stable RF negative inductor that would enable development of non-Foster MNZ metamaterials [73]. Unexpectedly, we have found that it is a much more difficult task than a construction of a negative capacitor. Difficulties arise from the low-frequency instabilities caused by the inductor-based positive feedback. We have bypassed this problem by the introduction of a lower cut-off frequency of a negative inductor. In this way, a point of potentially unstable operation was moved below the operating frequency range. We have designed, simulated and measured two prototypes of negative inductors and associated MNZ unit cells. The first prototype uses a modified Kolev's circuit [59] and generates effective inductance of -60 nH within the bandwidth 1 MHz-50 MHz. The second prototype uses an OPamp and it generates effective inductance of -10 nH within the bandwidth 100 kHz-700 MHz. As far as our knowledge goes, these are the best results available at the present state of the art (using technology of discrete components). Further improvement could eventually be possible by the use of microelectronic technology. Our numerical study showed that it should be possible to increase the highest operating frequency above 10 GHz by the use of standard 63 nm CMOS technology.
- We have analyzed a feasibility of adding tuneability/reconfigurability features to the developed negative capacitors/inductors and the associated unit cells of ENZ/MNZ metamaterials. In order to achieve this goal, we have built two prototypes based on two different approaches: tuning based on a variable positive feedback loop and tuning based on a variable negative feedback loop. In the first approach (a case of the negative capacitor), the key element is a varactor diode that allows direct tuning of the effective capacitance (by applying an external DC voltage). Achieved capacitance was between -25 pF and -100 pF within the bandwidth 1 MHz-40 MHz (OPamp-based prototype). In addition, the range between -1 pF to -3 pF within the bandwidth 100 kHz-700 MHz (improved OPamp-based prototype) was designed. In the case of the negative inductor, we used a PIN diode configured as a variable resistor that controls

the gain and, therefore, the value of generated effective inductance. Achieved effective inductance was between -5 nH and -9 nH, within the bandwidth 100 kHz-700 MHz. Finally, we have built and tested associated reconfigurable DPS-ENZ and DPS-MNZ unit cells.

- We have analyzed a feasibility of extension of the developed planar ENZ/MNZ metamaterials toward volumetric applications. The approach was based on ‘interfacing’ the TL structure to free-space via an array of ‘antennas’. Full-wave simulations proved correctness of the basic idea.

Chapter 3 BACKGROUND PHYSICS OF PRACTICAL NON-FOSTER METAMATERIALS

Background physics of practical non-Foster metamaterials

3.1. Previous work: The unclear issues of physics of non-Foster elements

The basic element of any broadband non-Foster metamaterial is a non-Foster element itself (i.e., a negative capacitor or a negative inductor). Practical non-Foster metamaterials developed so far were predominantly based on negative capacitors [65-68, 73-83]. A negative capacitor C_n (Figure 3-1 (a)), briefly explained in Chapter 1, is a hypothetical network element, capacitance of which has the sign opposite to the sign of an ordinary (positive) capacitor C_p with equal capacitance:

$$C_n = -C_p, \quad C_n < 0, C_p > 0. \quad (3.1)$$

A negative capacitor may be thought as a positive capacitor with flipped sign of the current (while the sign of the voltage across the capacitor terminals remains unchanged):

$$v = \frac{1}{C_n} \int i(t) dt = -\frac{1}{C_p} \int i(t) dt = \frac{1}{C_p} \int [-i(t)] dt. \quad (3.2)$$

Here $v(t)$ and $i(t)$ stand for the voltage and current defined at the capacitor terminals (Figure 3-1 (a)). It is known that an ordinary capacitor is a passive element, usually defined (in the circuit theory) as a reactive load. Thus, the current $i(t)$ flows *into* the positive terminal of an ordinary (positive) capacitor. However, (3-2) shows that the current $i(t)$ flows *out of* the positive terminal of a negative capacitor. Due to this, the negative capacitor should be thought of as a (reactive) source. As it was shown in Figure 1-3 (and, for the sake of convenience, repeated here in Figure 3-1) the dispersion curve of the negative capacitor is the exact inverse of the dispersion curve of an ordinary capacitor. In other words, the negative capacitor obviously violates Foster's reactance theorem (1.2).

The violation of (1.2) is actually not surprising since the negative capacitor is a source (i.e. it is an active device). On the contrary, Foster's theorem is strictly valid *only* for *lossless passive* networks.

From a practical point of view, it is important to construct a circuit that can flip the sign of the current in (3.2) (i.e. to invert the direction of the current flow while the voltage remains unchanged). One possible way of achieving this 'inversion' is sketched in Figure 3-1 (b).

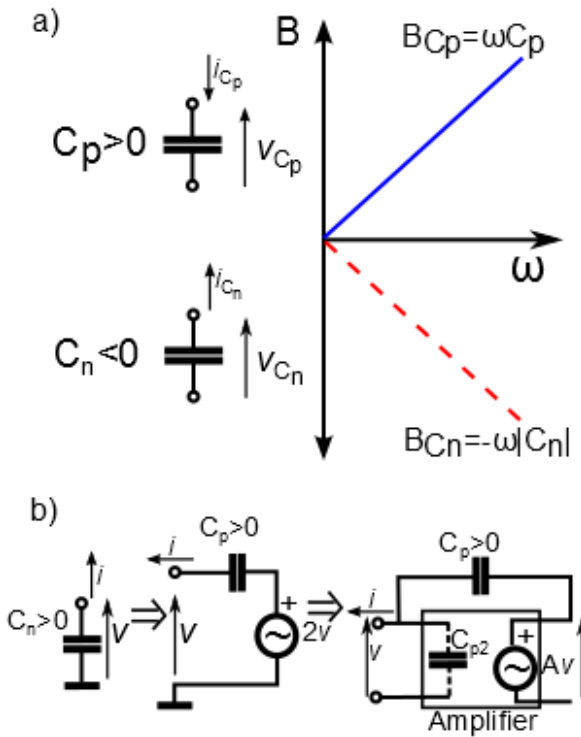


Figure 3-1 (a) Dispersion of a susceptance of various capacitor types. C_p (positive capacitor): solid blue curve, C_n (negative capacitor): dashed red curve. **(b)** Evolution of a model of negative capacitor. C_{p2} is an additional stabilizing ('swamping') capacitor used for ENZ effect

Here, a positive (grounded) capacitor C_p is connected in series with a voltage source $v_0(t)$ that is controlled by the input signal $v(t)$ (dependent source). The amplitude of $v_0(t)$ is chosen to be twice the amplitude of the input signal ($v_0(t)=2v(t)$). Since the voltage drop across the capacitor is now negative ($v(t)-2v(t)=-v(t)$), the net current $i(t)$ flows outward. Practically speaking, the dependent voltage source ($v_0(t)=2v(t)$) can be implemented by an (ideal) amplifier with (voltage) gain $A=+2$.

In principle, it is straightforward to generalize this simple principle to the circuit that does impedance inversion of any passive lumped element (Figure 3-2).

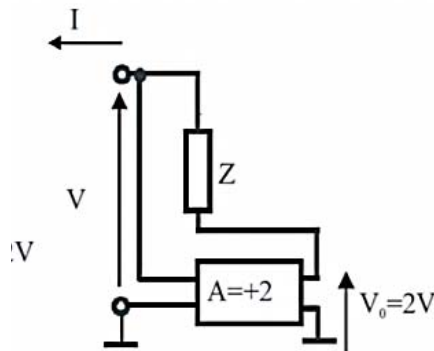


Figure 3-2 An example of the general operating principle of negative non-Foster impedance, based on a current negative impedance converter (INIC)

Repeating above analysis in phasor domain, one simply finds that the input impedance is given by:

$$Z_{in} = \frac{V}{I} = Z \cdot (1 - A) \quad (3.3)$$

In the case of an amplifier with fixed gain $A=+2$, (3.3) leads to a simple impedance inversion ($Z_{in}=-Z$). The circuit in Figure 3-2 is the so-called current negative impedance inverter (INIC) [30-36,73]. It is able to generate (depending on the character of impedance Z) negative resistance, negative capacitance, and negative inductance. Of course, it is possible to achieve the impedance inversion in other ways, as well. Looking back to (3.1) one could have flipped the sign of the voltage $v(t)$ or time t . These options would have led to the voltage negative impedance converter (VNIC) and a time-reversal circuit, respectively. The general theory can be explained equally well by any type of the NIC. However, the majority of practical devices developed in this project are of the INIC and, therefore it is used in all subsequent discussions.

It is important to notice that an idealized model in Figure 3-1 is dispersionless, i.e. a generated capacitance (or inductance) is not dependent on frequency, at all. It is interesting that many authors do not consider possible practical realization of it at all. Instead, they deal with a negative capacitor as an ordinary circuit element, defined in a *formal* mathematical way, $C_n < 0$. Sometimes, this simple approach is able of predicting (qualitative) behavior of the specific network.

For instance, this simple dispersionless model was used as a basic idea of capacitance decrease phenomenon (1.5) that led to the first practical non-Foster ENZ metamaterial [66]. Practical realization directly used the INIC approach from Figure 3-1. It was based on the AD8099, an ultra-fast voltage feedback operational amplifier (Figure 3-3 (a)) [73]. The circuit generates a negative capacitance, value of which can be adjusted (by varying a capacitance of C_1) to an arbitrary value in the range -20 pF to -100 pF, in the frequency band 2 MHz-40 MHz.

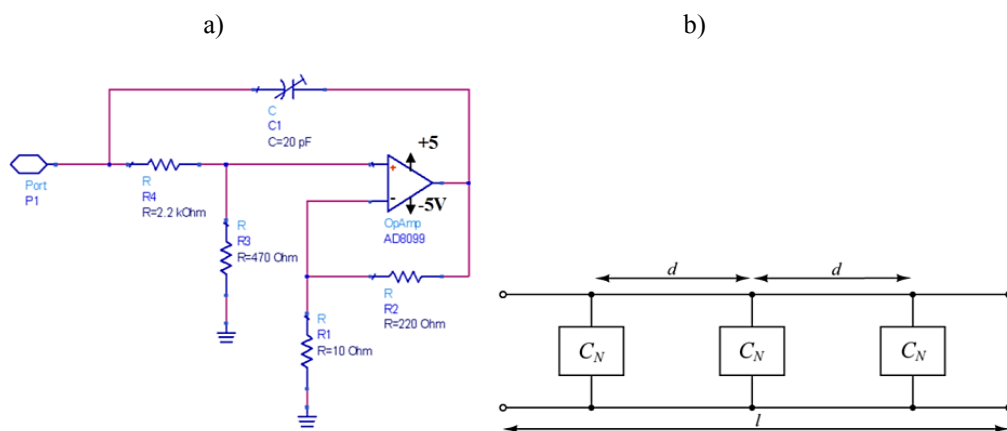


Figure 3-3 a) OpAmp-based RF negative capacitor, b) 1D ENZ metamaterial based on a transmission line loaded with three negative capacitors ([74])

Three negative capacitors were built and the measurement of input reflection coefficient revealed stable operation with an input capacitance of -60 pF in the frequency range 2 MHz-40 MHz. A simple, air transmission line was manufactured and periodically loaded with three negative capacitors [74] (Figure 3-3 (b)). The distance d between the elements was much smaller than the wavelength (approximately $\lambda/20$ at the highest frequency, λ being the free-space wavelength). According to the simplified explanation in (1.5) (the decrease of the

distributed shunt capacitance of the host transmission line by an ideal negative capacitor) one would (naively) expect the entirely dispersionless behavior of equivalent permittivity. However, complex permittivity extracted from the measurements of scattering parameters (Figure 3-4) shows only *approximately* dispersionless behavior.

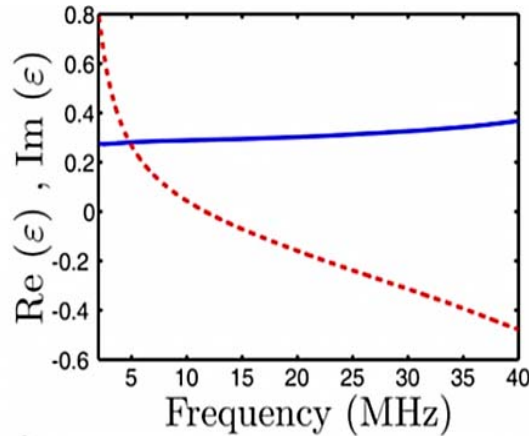


Figure 3-4 Measurement results of an active 1D non-Foster ENZ metamaterial [74], Solid – real part, Dashed – imaginary part

The real part of the effective permittivity is nearly dispersionless (it varies from 0.27 to 0.37 in the frequency range of more than four octaves (2 MHz to 40 MHz). At the same time the change of the imaginary part is more pronounced (it varies from +0.8 to -0.5). It can be guessed that the non-ideal, slightly dispersive behavior of a real part of the permittivity occurs due to a non-ideal amplifier in Figure 3-2 that obviously introduces some signal delay. However, it is not so straightforward to guess the origin of the pronounced dispersion of the imaginary part of equivalent permittivity that has both positive and *negative* signs. Although it is intuitively clear that every realistic negative capacitor (or more generally, every non-Foster element) *must* be frequency-limited, simple realistic models are not available. Thus, in this case, a simple model of a negative capacitor predicted correct quantitative behavior, but, it was not able to predict accurate dispersion characteristic.

Furthermore, the formal mathematical model of a negative capacitor ($C_n < 0$) says almost nothing about the background physics. What is the physical mechanism of the capacitance decrease in (1.3)? Does the negative capacitor somehow changes the net charge in the shunt branch of the unit cell in Figure 1-4 and, therefore, alters the equivalent capacitance? Does the energy flow into or out of the negative capacitor?

There are several other problems with the simple dispersionless model of a negative capacitor. The (entire) absence of the dispersion in ENZ metamaterial would mean the existence of superluminal group velocity *at every frequency* (i.e. the existence of superluminal energy propagation), which clearly violates causality. Again, it was noted that this paradox can be resolved by assumption that every realistic negative capacitor is always a frequency-limited device [74].

Even more striking example is the charging of the capacitor C by connecting it suddenly to a DC source via the resistor R [26]. From very basic physics, it is known that the voltage across the capacitor $v(t)$ has exponential form:

$$v(t) = V_B \cdot \left(1 - e^{-\frac{t}{\tau}} \right), \quad \tau = R \cdot C. \quad (3.4)$$

Here, V_B stands for the voltage of the DC source (a battery), t is the time and $\tau=RC$ is the time constant. In the case of an ordinary capacitor, both R and C are positive numbers. Therefore the time constant τ is a positive number, as well. This leads to a familiar exponential growth of the voltage until it reaches the voltage of the battery. However, in the case of a negative capacitor, the time constant τ is negative (due to $C<0$) causing an unbounded exponential decay. As time increases, the voltage decreases towards (negative) infinite value, causing infinite stored energy in the negative capacitor. At the same time, the power dissipated at resistor R increases towards infinite value. These effects do not seem to have a solid physical basis. This example shows that a negative capacitor is, under some circumstance, unstable (in practice, an onset of the oscillations will occur instead of the constant growth of the negative voltage). Actually, a negative capacitor cannot be used as a single isolated element because it is inherently unstable. Of course, one can work out the natural response of the circuit [73,46]. This analysis shows that there is a pole located in the right-hand-side of a complex plane. Formally, occurrence of instability occurs due to this pole. However, again it says nothing about the physical origin of the instability. Additionally, previous studies showed that a frequency-domain approach to stability issue completely fails here [73,46]. If one evaluates the absolute value of a reflection coefficient, he will get unit value, exactly as it would be in the case of an ordinary capacitor. So, one could (wrongly) conclude that the negative capacitor is a stable device.

For stable operation, a negative capacitor should always be connected to other (swamping) network elements. For instance, let us analyze a parallel combination of a positive capacitor C_p and a negative capacitor C_n . One easily deduces that the positive capacitor should have capacitance larger than the capacitance of the negative capacitor in order to assure stability. In other words, the overall capacitance C_0 should be positive:

$$C_0 = C_p + C_n = C_p - |C_n|, \quad C_p > |C_n|. \quad (3.5)$$

In attempt of generalization of (3.5) one may say that the positive overall capacitance along a closed loop is enough to assure stability. Although, this is usually believed so, the recent studies [73,46] showed that this is not true. The stability criterion is much more complicated and it depends on the network topology (therefore on the external passive elements connected to a negative capacitor).

There is also an unclear issue of ‘boosting’ of the negative capacitance. Let us assume that there is a negative capacitor C_n connected in a series with the positive capacitor C_p . In addition, let us assume that the capacitance of the positive capacitor is larger than the capacitance of the negative capacitor. A simple calculation shows that the overall capacitance should be negative and *larger than* a capacitance of the active negative capacitor:

$$C_0 = \frac{C_p \cdot C_n}{C_p + C_n}, \quad C_p > |C_n| \Rightarrow C_0 < 0 \vee |C_0| > |C_n|. \quad (3.6)$$

What is the physical background of this ‘boosting’ phenomenon?

Brief discussion above clearly shows that the basic physics of the negative capacitor is indeed counter-intuitive and that it should be investigated in time domain. There are three main problems with a simple, ideal, dispersionless model of a negative capacitor ($C_n < 0$):

- A dispersionless model can predict *qualitative* behavior but only within some finite bandwidth (the bandwidth, in which a practical negative capacitor

generates negative capacitance). Outside this band, the model should not be used at all (even for qualitative analysis) because it gives unphysical behavior (cases with pulse excitation, transient effects etc.). This is a direct consequence of the fact that the ideal model is not causal. Capacitance of every practical negative capacitor change with frequency. When frequency increases, the capacitance must become positive at some frequency.

- A dispersionless model is useful only in the case of low losses of a realistic negative capacitor. Inclusion of the shunt resistor in the model can (approximately) describe the losses. However, this approach cannot predict the negative input conductance that occurs quite often in the negative capacitors.
- A dispersionless model cannot predict any quantitative behavior. Therefore, it cannot be used for the design that should meet some prescribed specifications.

3.2. Investigation of basic physics of negative capacitor in time domain

(*The part of the results presented in the sections 3.2. were achieved with the help of Boris Okorn, who is a Ph.D student at University of Zagreb).

Recently, the negative capacitor was experimentally investigated in frequency domain, as a part of the metamaterial-based active transmission line [73,46,74]. In the same study, it was stressed that the analysis of basic physics in general, and of the stability, in particular, should be performed in time-domain. This is due to previously noted fact that ordinary frequency domain methods of assessing stability fail for the case of negative elements [73,46]. On the other hand, the time-domain measurements of the negative capacitors are difficult in the RF regime since associated values of capacitance are usually of the same order of magnitude as the capacitance of the oscilloscope probe (a few pF). Therefore, it was decided to relax this constrain by construction of a low-frequency laboratory model of a negative capacitor that can generate high values of the capacitance (in order of μF). This model should enable direct investigation of physics of the negative capacitor and, hopefully, help in understanding of some counter-intuitive basic issues.

3.2.1 Construction and initial testing of a low-frequency demonstrator

The experimental low-frequency prototype of a negative capacitor is shown in the lower part of Figure 3-5 (a). The design of the negative capacitor closely follows the basic idea from Figure 3-1 and it is actually a low-frequency version of our previous RF prototypes [73,74]. It is based on an integrated audio amplifier LM1875 and it was designed in a way that enables generation of a rather large negative capacitance ($-1.2 \mu\text{F}$). This large value is almost insensitive to the capacitance of the oscilloscope probes, assuring simple and reliable time-domain measurements. At first, the basic properties of negative capacitance circuit were investigated using a commercial circuit-theory simulator (ADSTM). A sample of predicted values of generated input negative capacitance and parallel conductance is shown in Figure 3-5 (b) and (c). It can be seen that the circuit generates almost constant capacitance of $-1.2 \mu\text{F}$ with negligible conductance ($<5\text{mS}$) in the frequency range 1 kHz-25 kHz.

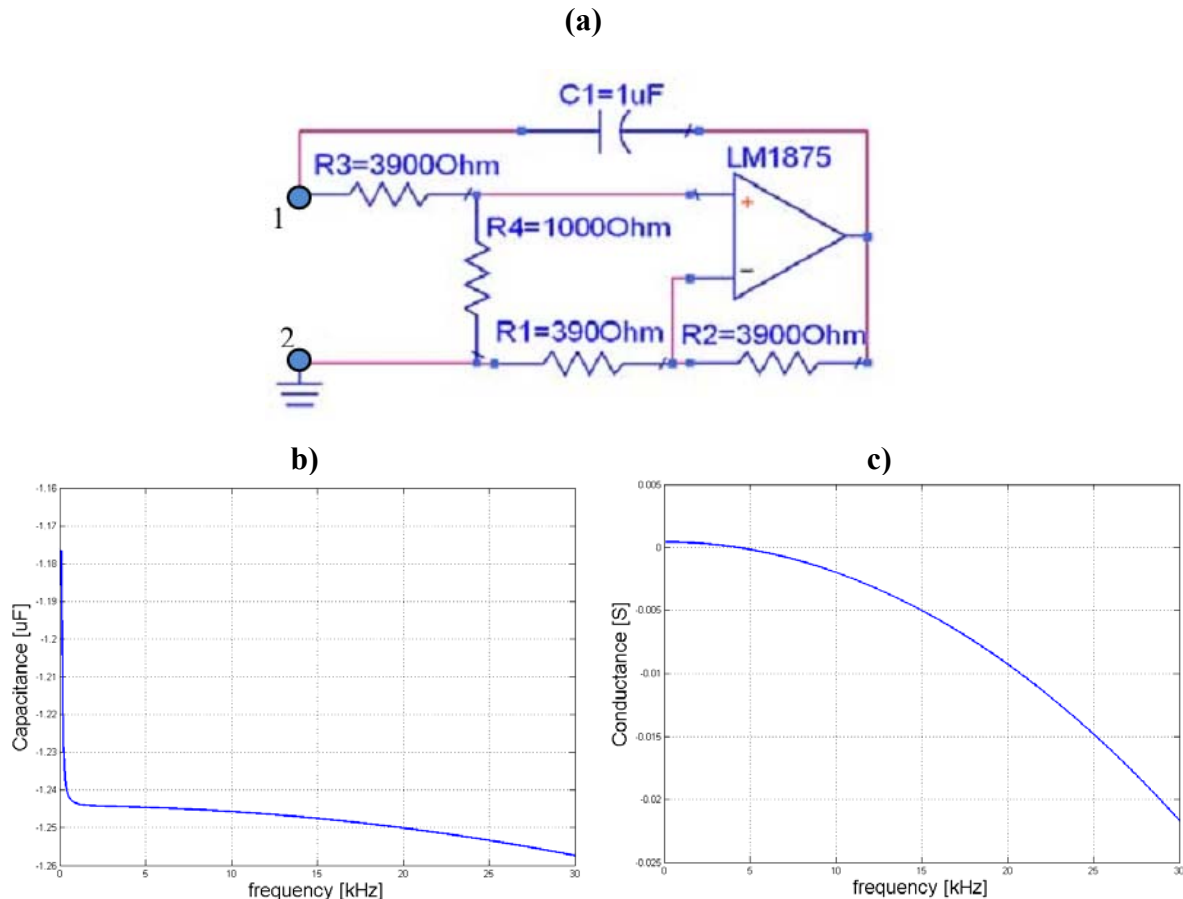


Figure 3-5 a)Experimental realization of a low-frequency negative capacitor demonstrator, b)Simulated input capacitance, c) Simulated input conductance

In the first experiment, the stability of the negative capacitor was checked. Several different parallel combinations of positive and negative capacitors were used for this purpose. The voltage across the negative capacitor and the current flowing through it were monitored by a digital oscilloscope (Tektronix TDS 2024B) and the current probe (Tektronix TM502A with AM503 amplifier). It was found that no voltages or currents existed in the loop if $|C_p| > |C_n|$. On the contrary, if $|C_p| < |C_n|$ the circuit was unstable (the negative capacitor circuit was oscillating and associated waveforms resembled those from ordinary relaxation oscillator). In addition, a trimmer resistor was connected in series with the negative and positive capacitors, forming a closed loop. It was found that this combination was stable for very small values of the resistance ($< 5\Omega$). If the resistance is increased above this value the circuit becomes unstable. It is in excellent agreement with the theoretical results from [73,46]. This clearly shows that the stability does not depend on the negative capacitor only, but rather it depends on the topology of the whole network including external elements.

3.2.2 Direct observation of negative capacitance

In the second experiment, a simple RC filter (an integrator) was constructed (Figure 3-6). It comprised a resistor ($R=3900 \Omega$) and a positive capacitor ($C_p=1.5 \mu F$). The function generator, adjusted to generate sinusoidal signal at the frequency of 2.4 kHz, was used as a source. The measured waveforms revealed familiar positive phase shift of $+90^\circ$ between the voltage and current at the positive capacitor. However, the phase shift between the voltage and current at the negative capacitor (Figure 3-6 (b)) was found to be negative (-90°), thus the voltage signal leads the current signal for all the frequencies within the range of 1 kHz-25 kHz. It resembles a property of an ordinary inductor. However, if one evaluates the reactance (V/I), he will reveal a decrease with the respect to the frequency. This is a direct proof of the negative capacitance. Due to small inherent losses the phase shift was not exactly equal to -90° for all the frequencies. However, the basic phenomenon was proven.

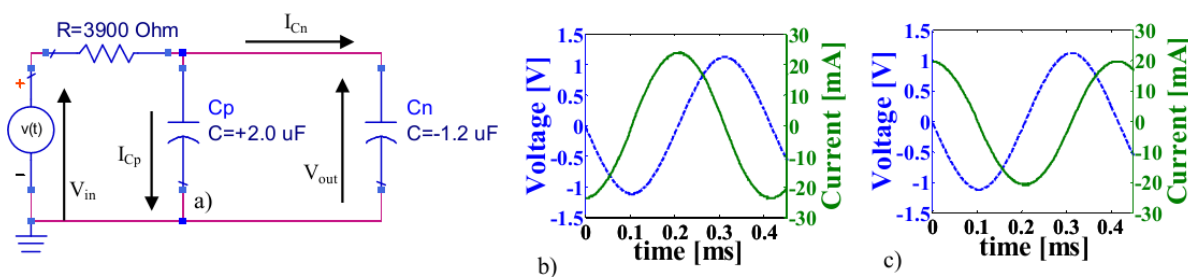


Figure 3-6: a) Experimental integrator circuit with positive capacitor C_p and negative capacitor C_n , excited by a sinusoidal signal. b) Measured waveforms at C_p : voltage (dashed blue) and current (solid green). c) Measured waveforms at C_n : voltage (dashed blue) and current (solid green).

3.2.3 Capacitance decrease phenomenon (ENZ phenomenon)

In this step, the capacitance decrease phenomenon was investigated. The waveform of the signal generated by the function generator was adjusted to a square wave. The rectangular signal is needed for the investigation of the energy exchange between the positive and negative capacitors (Figure 3-7). When the negative capacitor is disconnected from the network, one has an ordinary (passive) integrator circuit. It has familiar waveforms that show charging and discharging of the positive capacitor (the integration) (Figure 3-7 (a)). However if the negative capacitor is present, the situation is fundamentally different (Figure 3-7 (b)).

At first, one notices that the output voltage reaches its final value sooner than in a previous case (the curve has a steeper slope). In the same graph it can be seen that the one current flows *from* the negative capacitor while the second current flows *into* the positive capacitor. The current that flows into the positive capacitor is larger than the current which would flow into it if the negative capacitor were disconnected. Therefore, it can be concluded that the negative capacitor is indeed a source that helps in charging the positive capacitor when the square wave at the input of the network has positive amplitude. However, it is also a sink (in other words, a source with reversed polarity) that helps in discharging the positive capacitor when the input square wave has negative amplitude. Very similar behavior was observed for the other frequencies in the whole frequency bandwidth of the experimental model (1 kHz - 25 kHz).

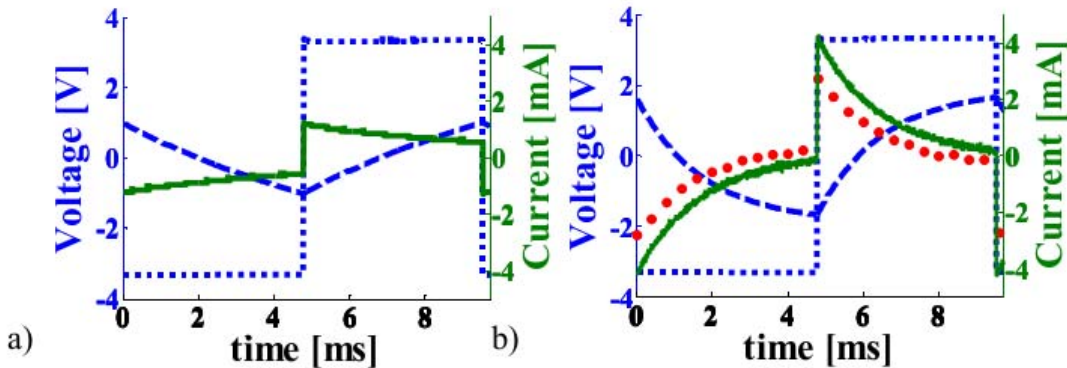


Figure 3-7: Measured waveforms on experimental integrator circuit with positive capacitor (C_p) and negative capacitor (C_n), excited by a signal with rectangular waveform

a) Input voltage (dotted blue), output voltage (dashed blue) for the integrator with a positive capacitor, current (solid green) that flows into the positive capacitor (C_p)

b) Input voltage (dotted blue), output voltage (dashed blue), the current that flows into positive capacitor C_p (solid green) and current that flows out from the negative capacitance C_n (dotted red)

3.2.4 Negative capacitance boosting phenomenon

In this step, the ‘boosting’ of the negative capacitance was investigated (Figure 3-8). The circuit comprise a series combination of a positive capacitor ($+3 \mu\text{F}$) and a negative capacitor (generated by low-frequency demonstrator) ($-1.2 \mu\text{F}$). Analysis of the charging curve revealed generation of the negative capacitance that is 70% larger than the capacitance generated by the active circuit itself. The physical explanation is similar to that from the previous experiment. The negative capacitor now helps in charging/discharging of both positive capacitors. This allows the series combination of the positive and negative capacitor to be interpreted as the new equivalent negative capacitor. Achieved overall negative capacitance is larger than the negative capacitance obtained by the active circuit in the case with no additional positive capacitor.

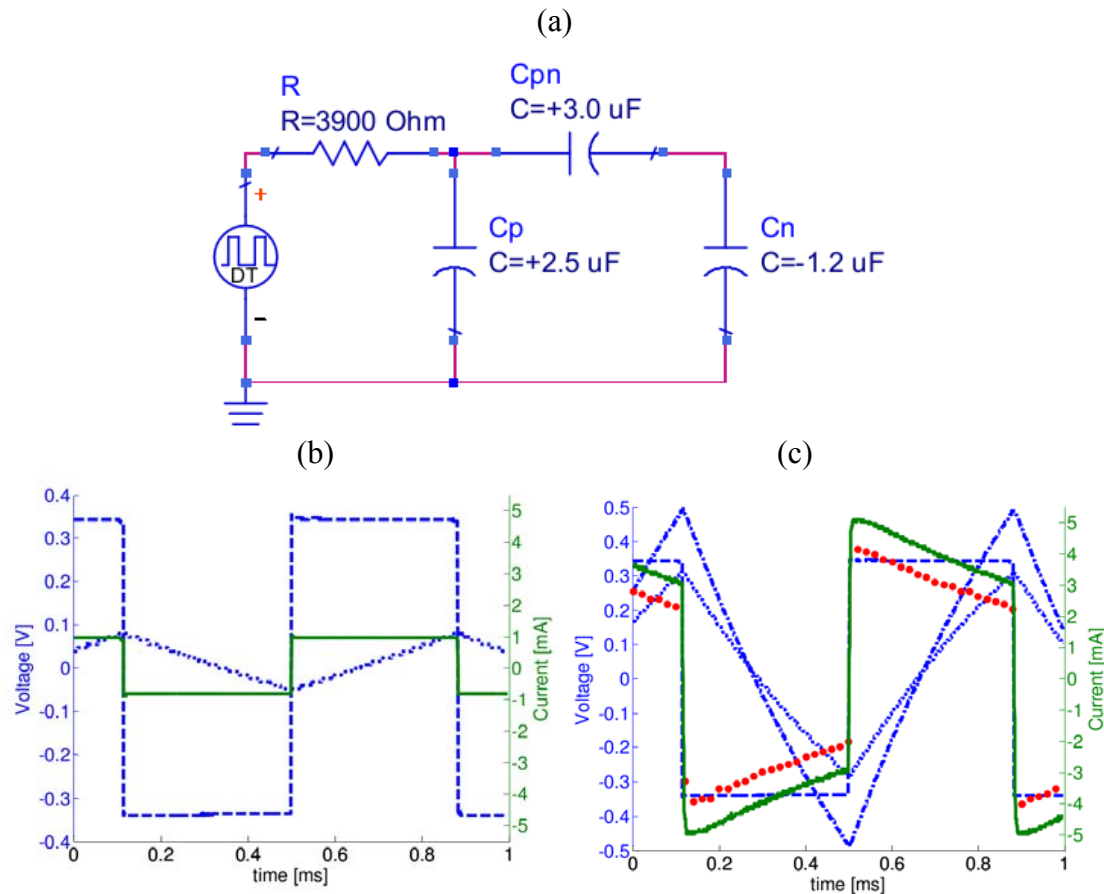


Figure 3-8 a) Experimental circuit for investigation of negative capacitance boosting phenomenon
 b) Measured input voltage (dotted blue), output voltage (dashed blue) for integrator with a positive capacitor, current (solid green) that flows into the positive capacitor (C_p)
 c) Measured input voltage (dotted blue), output voltage (dashed blue,), the voltage on negative capacitor C_n (dot-dashed), the current through the positive capacitor C_p (solid green) and the current that flows out from the negative capacitance C_n (dotted red)

As a simple cross-check of the operation of low-frequency negative capacitance demonstrator, the values of generated negative capacitance were extracted from the time-domain measurements, (using a circuit from Figure 3-6 (a)). Obtained results (Figure 3-9) showed that the developed circuit generated the negative capacitance from $-1.2 \mu\text{F}$ to $-0.6 \mu\text{F}$ within the frequency range of 1 kHz - 25 kHz . It can be observed that the circuit indeed generates almost constant, large negative capacitance ($-1.1 \mu\text{F}$) in a wide frequency range (5 kHz - 15 kHz).

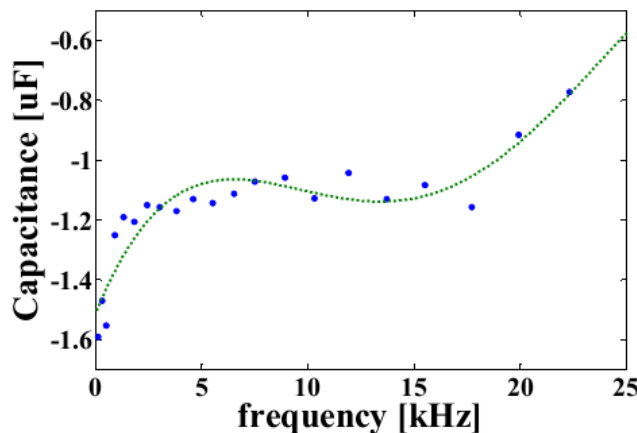


Figure 3-9 Values of negative capacitance extracted from the time-domain measurements. Dots (blue): raw data, Dotted green curve: 4th order polynomial fit

All the results presented in this section show that time-domain analysis gives a deep insight into the physics of non-Foster capacitor. In addition, it is clear that the dispersion of realistic negative capacitor is a key issue that somehow should be incorporated into the basic model from Figure 3-1. This is attempted in the next section.

3.3. Improvement of model of negative capacitor

In the first step, one may try to model a realistic negative capacitor as a parallel combination of the conductance G and an ideal non-Foster negative capacitance C_n (Figure 3-10). (Of course, the model based on a series combination of a resistor and a negative capacitor is mathematically correct, as well. However, this model is inconvenient since the negative capacitors are usually used in a shunt branch of the host transmission line.)

In the case of an ideal amplifier (in Figure 3-1), the voltage gain A is a real number and there is no signal delay across the amplifier. In the frequency domain (phasor domain), it means that there is no phase shift between the input and output signals. If one draws the phasor diagram (Figure 3-10 (a)), he will find that the input current lags the input voltage, thus the input impedance is a pure negative capacitance. However, every realistic amplifier always introduces some delay or (in the frequency domain) some phase shift Φ (in other words, the gain A is a complex number). The phasor diagram for this case is sketched in Figure 3-10 (b). A simple analysis shows that in this case there is a component of the input current that is 180 degrees out of phase in respect to input voltages. Thus, the origin of negative input conductance (that often occurs in realistic negative capacitors) lies in the inevitable phase shift of the used active element.

This brief analysis shows importance of the phase shift (or, more generally, complex gain) of the active element used in negative capacitor. In the following sections, this issue is investigated in more details. Obtained analytical results are cross-checked by SPICE simulation of a low-frequency demonstrator based on the LM1875 OPamp (section 3.2).

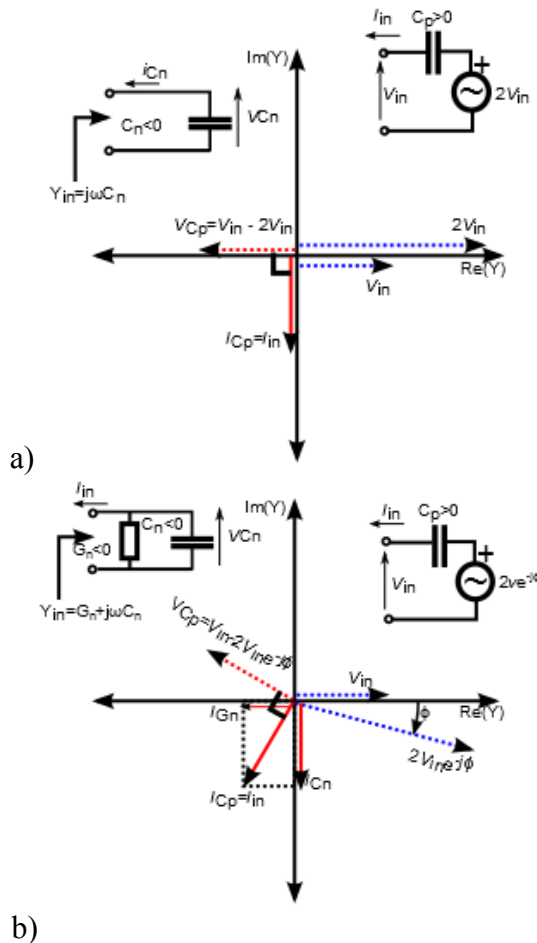


Figure 3-10 Phasor diagram for a negative capacitor. **a)** ideal case with zero-valued time delay (there is no phase shift in dependent voltage source) **b)** realistic case with finite time delay (there is a phase shift in dependent voltage source)

3.3.1 One-pole model of the negative capacitor

As mentioned before, every realistic amplifier introduces some signal delay (dependent on the used elements and internal construction of the amplifier). In the frequency domain, it means that the gain (both the magnitude and phase) is a function of frequency. In circuit theory, the transfer function of an amplifier is often described by the n-pole model:

$$A(\omega) = \frac{A_0}{\prod_{i=1}^{i=n} \left(1 - j \frac{\omega}{\omega_i} \right)}. \quad (3.7)$$

Here, A_0 stands for the zero-frequency gain and ω_i is the angular frequency of i -th pole. The number of poles that is needed for description of some device depends on the required accuracy and device's internal construction.

Let us start with a very simple one-pole model. It is a simple exercise to derive the input admittance of the realistic negative capacitor:

$$V_{source} = \frac{2V_{in}}{1 - j \frac{\omega}{\omega_1}}, \quad Y_{in} = -Y \frac{1 - j \frac{\omega}{\omega_1}}{1 + j \frac{\omega}{\omega_1}}, \quad Y_{in} = j\omega C_n + G_n \quad (3.8)$$

Equivalent input capacitance and inductance (C_n , G_n) of the LM1875 OPamp-based negative capacitor were calculated using (3.8). The element values from Figure 3-5, together with the frequency of the first pole (found in the manufacturer's data sheet) were used in calculation. The results are shown in Figure 3-11. It can be seen that the input capacitance becomes positive above the frequency of the first pole, which is physically sound. However, the input conductance remains negative for all of the frequencies up to infinity. This is clearly a non-physical result that shows that the one-pole model is not a good description of a realistic non-Foster negative capacitor.

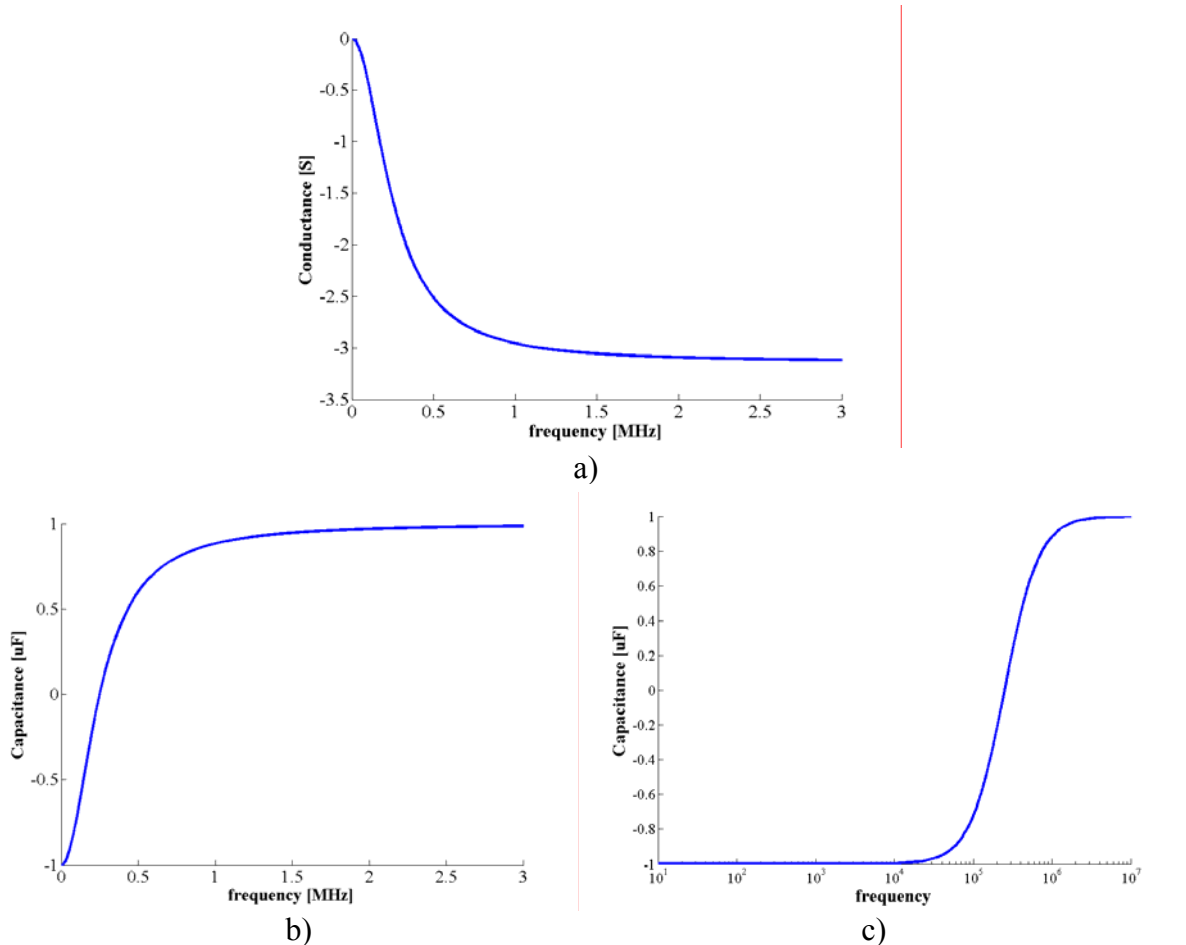


Figure 3-11 One-pole analysis **a)** Equivalent input conductance G , **b)** Equivalent input capacitance C_n , **c)** Equivalent input capacitance C_n plotted in logarithmic scale that prompts a flat frequency response across wide bandwidth. ($f_{p1} = 250$ kHz)

3.3.2 Two-pole model of the negative capacitor

One may say that the unrealistic results obtained by the one-pole model are not surprising since the phase shift of the amplifier has a maximal value of 90 degrees. Adding the second pole to the transfer function leads to the maximal phase shift of 180 degrees, which is more realistic. Again, the input admittance is calculated using the basic circuit equations:

$$V_{source} = \frac{2V_{in}}{\left(1 - j\frac{\omega}{\omega_1}\right)\left(1 - j\frac{\omega}{\omega_2}\right)}, \quad Y_{in} = Y \left(1 - \frac{2}{\left(1 - j\frac{\omega}{\omega_1}\right)\left(1 - j\frac{\omega}{\omega_2}\right)}\right), \quad Y_{in} = j\omega C_n + G_n. \quad (3.9)$$

Similarly to the previous case, equivalent input admittance was calculated using the manufacturer's data for the frequencies of the first and second pole. Obtained results are shown in Figure 3-12. It can be seen that the behavior of the input capacitance C_n remained similar to the previous one-pole case. The difference is in the occurrence of a slight overshoot. The curve of the equivalent conductance G_n is still negative within the large part of the frequency spectrum and it asymptotically approaches zero for the frequencies above 10 MHz. This behavior does not seem to be physical. In addition, an unexpected, pronounced 'dip' at the frequency of 800 kHz is noted.

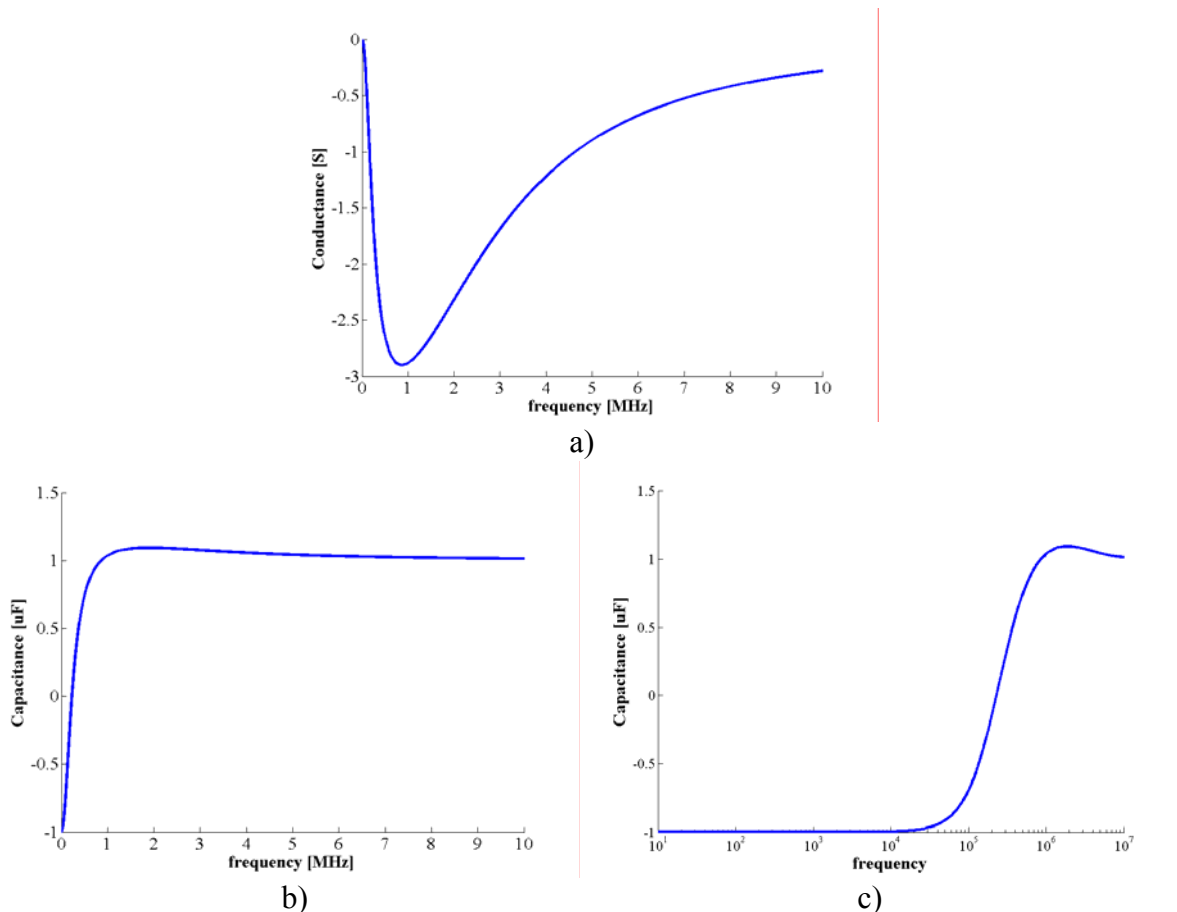


Figure 3-12 Two-pole analysis **a)** Equivalent input conductance G_n , **b)** Equivalent input capacitance C_n , **c)** Equivalent input capacitance C_n plotted in logarithmic scale that prompts a flat frequency response across wide bandwidth. ($f_{p1} = 250$ kHz, $f_{p2} = 1$ MHz)

3.3.3 Three-pole model of the negative capacitor

The next step is a three-pole analysis. The source voltage and input admittance are given by:

$$V_{source} = \frac{2V_{in}}{\left(1 - j\frac{\omega}{\omega_1}\right)\left(1 - j\frac{\omega}{\omega_2}\right)\left(1 - j\frac{\omega}{\omega_3}\right)}, \quad Y_{in} = Y \left(1 - \frac{2}{\left(1 - j\frac{\omega}{\omega_1}\right)\left(1 - j\frac{\omega}{\omega_2}\right)\left(1 - j\frac{\omega}{\omega_3}\right)}\right), \quad Y_{in} = j\omega C_n + G_n. \quad (3.10)$$

The results of calculation of a three-pole model are given in Figure 3-13. It can be seen that both the conductance and capacitance become positive numbers at high frequencies. This is causal behavior, therefore, the three-pole model appears to be physically correct.

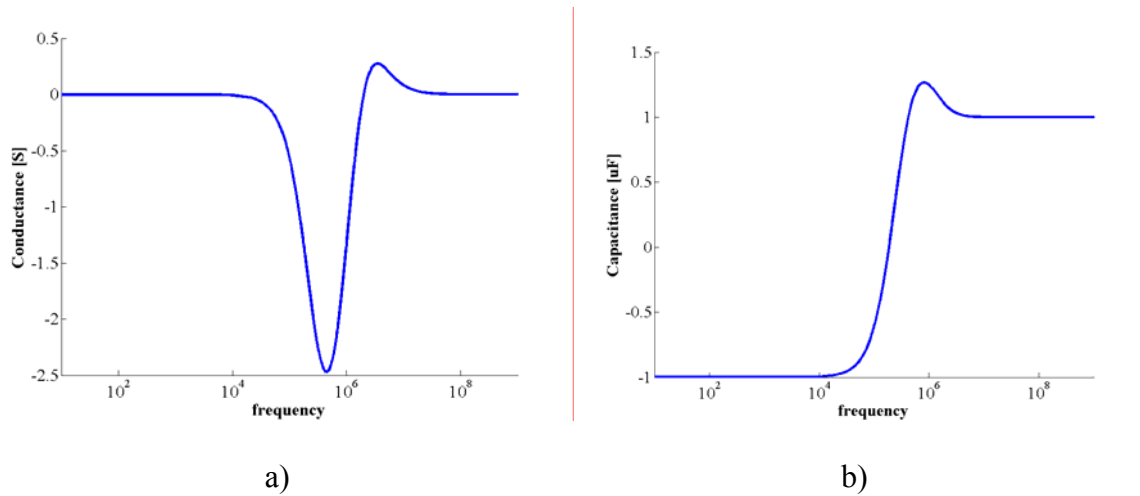


Figure 3-13 Three -pole analysis **a)** Equivalent input conductance G_n , **b)** Equivalent input capacitance C_n
($f_{p1} = 250$ kHz, $f_{p2} = 1$ MHz, $f_{p3} = 3$ MHz)

In order to validate the three-pole model we performed circuit-theory simulation of the negative capacitor using manufacturer's SPICE model of the LM1875 amplifier. It should be noted that all other passive components are assumed to be ideal. It can be seen (Figure 3-14) that obtained results are in a good agreement with three-pole analysis.

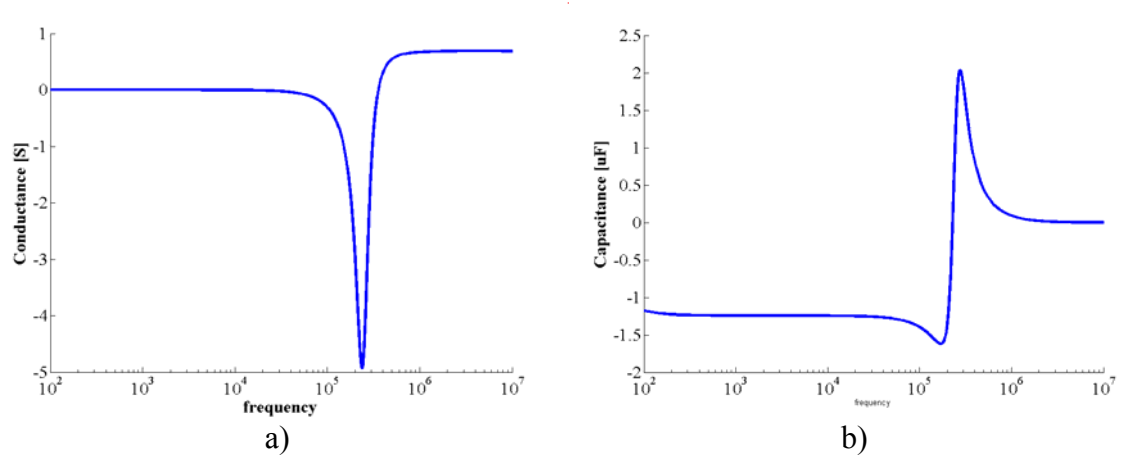


Figure 3-14 Results of SPICE simulation of input impedance of LM1875-based negative capacitor **a)** equivalent input conductance G_n , **b)** equivalent input capacitance C_n

The three-pole mode can be used for the theoretical investigation of the 'boosting' phenomenon that was studied experimentally in the section 3.2.4. We compared two different cases. The first case (Figure 3-15 (a)) deals with 'boosted' negative capacitor of capacitance $-2 \mu\text{F}$ (a series combination of a positive capacitor ($+3 \mu\text{F}$) and a negative capacitor ($-1.2 \mu\text{F}$)). The second case (Figure 3-15 (b)) deals with a negative capacitor of $-2 \mu\text{F}$. It can be seen that the bandwidth of the 'boosted' negative capacitor is narrower than the bandwidth of a 'regular' negative capacitor. Additional interesting observation is that the generated conductance is lower in the case of 'boosted' capacitor. Thus, the boosting might be useful for lowering loss/gain of the negative capacitor (but, at the cost of bandwidth).

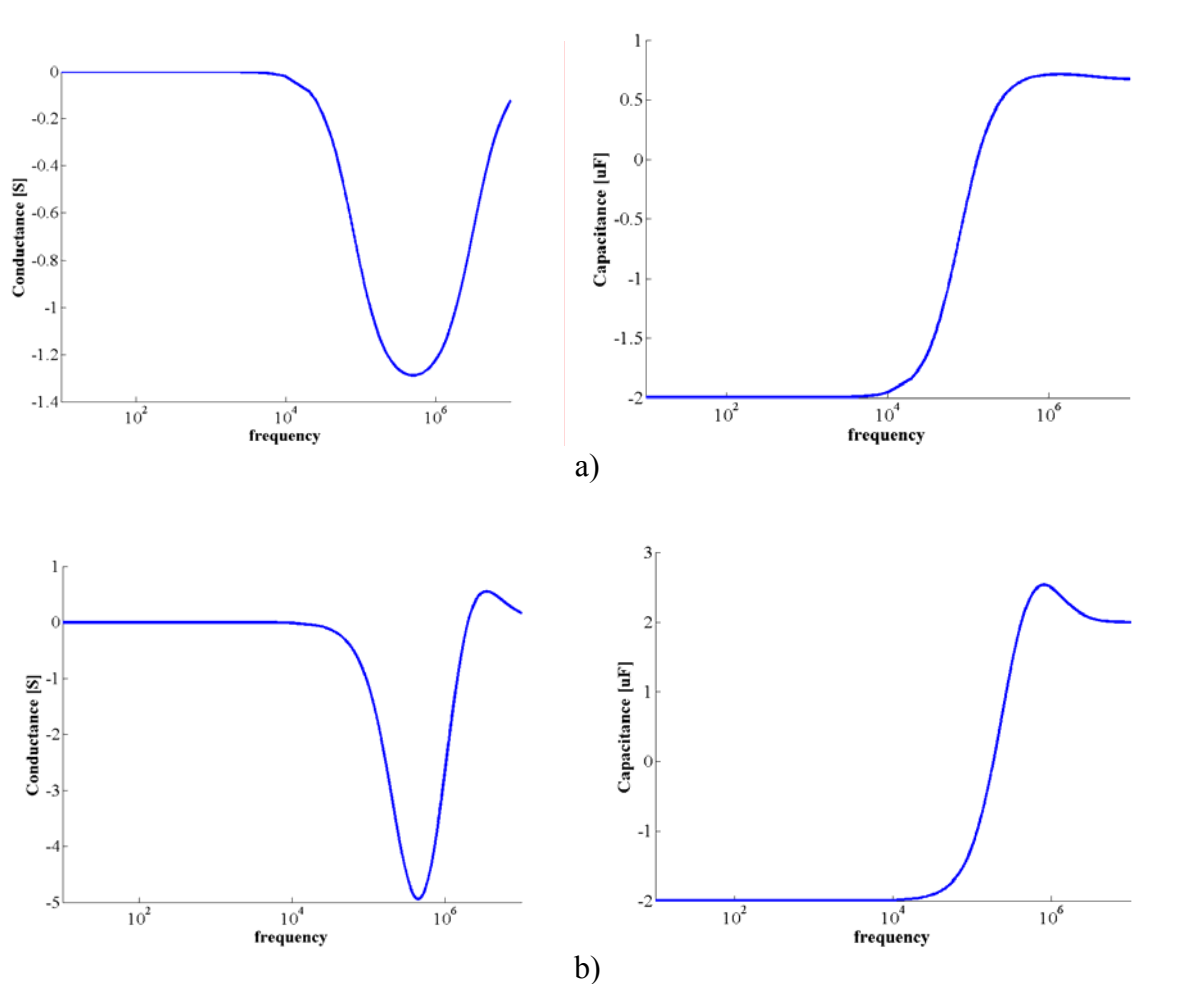


Figure 3-15 The 'boosting' of the negative capacitance. **a)** G_n and C_n of a 'boosted' negative capacitor , **b)** G_n and C_n of a 'regular' negative capacitor

Finally, we measured the input admittance of the low-frequency demonstrator with the help of an Agilent 4294A impedance analyzer. The standard method with additional stabilizing ('swamping') positive capacitor was used in extraction. The results are shown in Figure 3-16 and Figure 3-17. At first, the isolated stabilizing capacitor was measured (Figure 3-16). After that, the stabilizing capacitor was connected to the negative capacitor and input admittance is measured (Figure 3-17 (a)). Using obtained data, the equivalent capacitance and conductance of the negative capacitor are extracted (Figure 3-17 (b)). At first, it can be seen that the used stabilizing capacitor was of rather poor quality (there is a resonance at 450 kHz). The similar

resonance can be spotted in the curve of extracted negative capacitance (located at the slightly different frequency of 350 kHz). This happened because the same type of the (low quality) capacitor was used in the feedback loop. These irregularities should disappear with the use of the capacitors with higher quality. Apart from these unwanted resonances associated with technological problems, the general behavior of both the input capacitance and input conductance (Figure 3-17 (b)) was found consistent with the prediction from the three-pole model. It can be seen that around the frequency of 250 kHz (the frequency of the first pole), the capacitance becomes a positive number. This is in a very good agreement with the prediction from the three-pole theory.

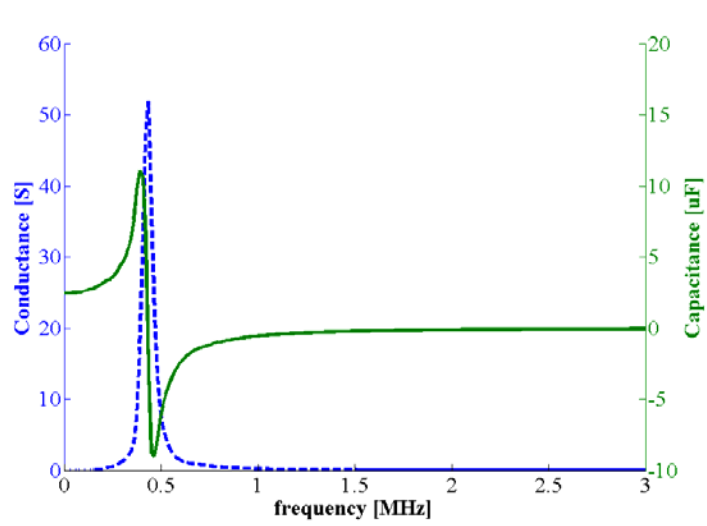


Figure 3-16 Measured capacitance and conductance of the ‘swamping’ positive capacitor C_p

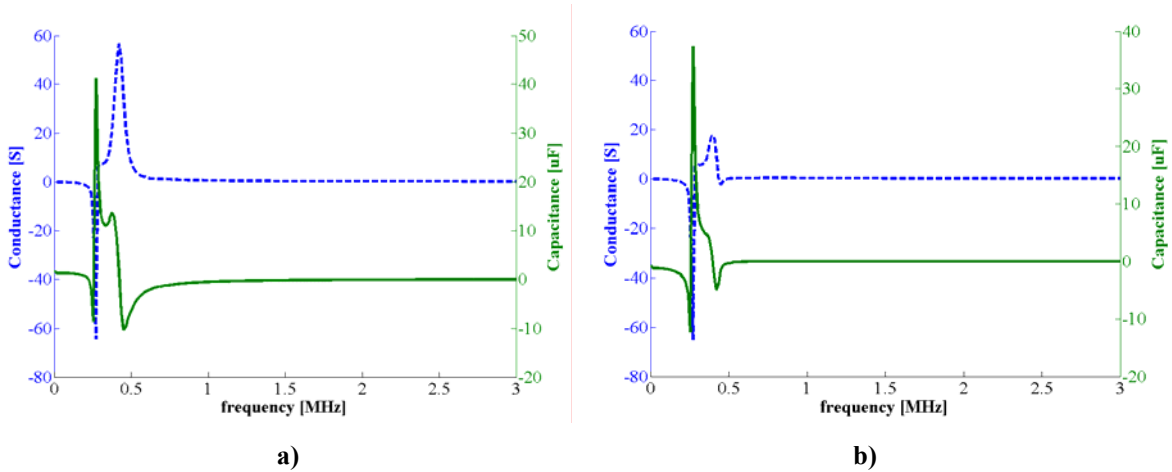


Figure 3-17 (a) Measured capacitance and conductance of the negative capacitor (low frequency demonstrator) with connected ‘swamping’ positive capacitor C_p **(b)** Extracted values of the input capacitance and input conductance for low-frequency demonstrator.

It can be concluded that three-pole model of negative capacitor is physically sound and accurate. It can predict both qualitative and quantitative behavior of a realistic negative capacitor.

3.4. Phenomenon of simultaneous superluminal phase and group velocities

The phase velocity (v_p) is one among the fundamental quantities in the electromagnetic theory, defined by [16]:

$$v_p = \frac{\omega}{k} = \frac{c}{\text{Re}(n)}, \quad n = \sqrt{\mu_r \epsilon_r}. \quad (3.11)$$

Here, ω stands for the angular frequency, c is the speed of light, k is a real-valued wave vector and $n=n'-jn''$ is the complex index of refraction. If ϵ_r (or μ_r) has a real part that is smaller than one (a case of ENZ or MNZ metamaterials) the phase velocity becomes ‘superluminal’ ($v_p > c$). It is well known that the superluminal phase velocity does not violate causality. The phase velocity is just a velocity of the point of a constant phase of a monochromatic signal, so it is not a ‘physical’ velocity [16]. In spite of this, the effect of superluminal phase velocity is essential for many potential engineering applications based on transformation electromagnetics. These include the invisibility cloaks [5,6], the field concentrators and wavefront converters [12,13,]. Unfortunately, the operating bandwidth of all these devices is inherently narrow (a typical relative bandwidth is smaller than 1% (1:1.01) [14]. This happens because a band with either ENZ ($0 < \epsilon_r < 1$) or MNZ ($0 < \mu_r < 1$) behavior (i.e. the ‘superluminal band’) is always finite and dispersive. Of course, this is the consequence of the energy-dispersion constraints (1.1) or, in other words of the Foster theorem, (1.2). Essentially, the superluminal phase velocity is a resonant narrowband phenomenon.

The second fundamental velocity is the group velocity (v_g), defined as the velocity of an envelope of a narrowband multi-frequency signal [16,17] :

$$v_g = \frac{\partial \omega}{\partial k} = \frac{c}{\text{Re}(n) + \omega \frac{\partial \text{Re}(n)}{\partial \omega}}. \quad (3.12)$$

Strictly speaking, the superluminal group velocity violates dispersion constraints. Therefore it occurs only in the vicinity of either an absorption line or a gain line (this is a well-known case of the anomalous dispersion [16], which is again *a resonant narrowband phenomenon*). However, the preliminary results recently shown in [73,74] demonstrated that non-Foster ENZ metamaterial supports *simultaneous* (and nearly *dispersionless*) superluminal phase and group velocities. Here, we report the detailed experimental investigation of these counter-intuitive effects and correlate them to the model of the negative capacitor. This investigation is done both in the frequency and time domain. The used non-Foster ENZ metamaterial was a transmission line loaded with three negative capacitors, previously developed in our group and used in several experiments [73] (and briefly reviewed in section 3.1). The relative permittivity varied from 0.27 to 0.37 within the frequency range of 2 MHz-40 MHz, spanning a bandwidth of 1:20 (180%)).

3.4.1 Investigation in frequency domain

The investigation in the frequency domain was based on the measurements of the scattering parameters (network analysis) with the help of an ZVA8 Rohde Schwarz vector network analyzer (test port impedance of 50Ω). Active transmission line (1D active non-Foster ENZ metamaterial from [74]) was sequentially excited at both of its ends (Figure 3-18

(a)). The corresponding 2x2 scattering matrix was measured and the phase and group velocities were extracted using a standard approach [17, 74]. Obtained results are shown in Figure 3-18. As expected, it was found that the real part of the complex index of refraction is smaller than one and nearly dispersionless (it varies from 0.5 to 0.65) within a very broad frequency range (2 MHz - 40 MHz). The change of the imaginary part is more pronounced (it varies from -0.4 to +0.3).

The extraction of the group velocity involves a numerical derivative of the real part of index of refraction in (3.12). However, due to inevitable influence of noise on the measurement, a direct calculation of derivative using raw data leads to significant numerical errors.

Thus, the measurement data were first fitted using the fifth order polynomial. The analysis of the fitting residuals revealed that the accuracy of this procedure was better than 1%.

The extracted phase and group velocities (Figure 3-18 (d)) show that active non-Foster ENZ metamaterial indeed supports ultra-broadband simultaneous superluminal phase and group velocity (v_p varies from $1.6c$ to $1.9c$ and v_g varies from $1.5c$ to $1.8c$ within 1:20 bandwidth (180%)). Of course, these results are the direct consequence of the ultra-broadband behavior of extracted complex effective permittivity shown in Figure 3-4 and repeated here for the sake of the convenience (Figure 3-18 (b)). The real part of the extracted permittivity is almost dispersionless, while the imaginary part shows both inherent loss and gain. It is interesting that the non-ideal behavior of the imaginary part does not have a significant impact on the broadband superluminal behavior. This can be seen from comparison of the real part of the exact index of refraction ($n' = \omega \text{Re}(\sqrt{\epsilon_{ef}})$) and the approximation that neglects loss/gain ($n' \approx \omega \sqrt{\text{Re}(\epsilon_{ef})}$) (Figure 3-18 (c)). The maximal difference between the exact value and loss-free approximation is 15%, which gives the maximal difference of 13% in the phase and group velocity.

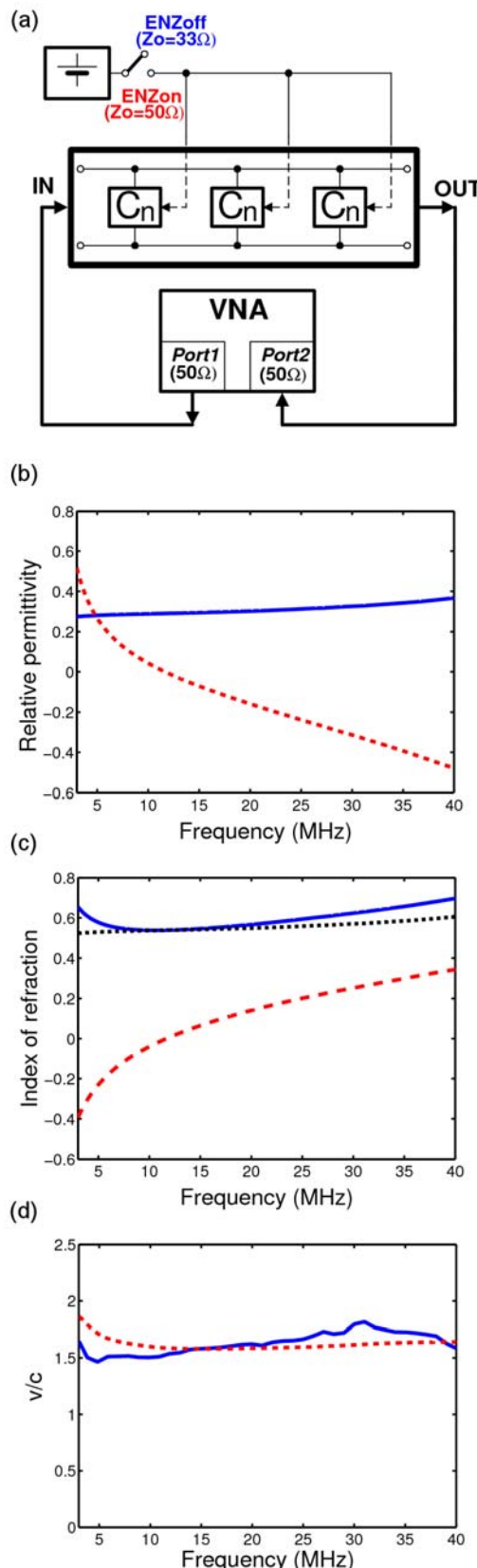


Figure 3-18 Measurements in the frequency-domain, (a) Experimental set-up (b) Extracted effective permittivity (real part: solid-blue, imaginary part: dashed-red) , (c) Extracted index of refraction (real part-solid-blue, imaginary part: dashed-red, the lossless approximation: dotted-black), (d) Extracted phase velocity (dashed-red) and the group velocity (solid-blue) [80].

3.4.2 Investigation in time domain

In order to understand the counter-intuitive underlying physics of a simultaneous superluminal broadband phase and group velocities and its connection with causality, we have performed the measurements in time-domain, as well (Figure 3-19). Active non-Foster ENZ metamaterial was excited by Agilent arbitrary waveform generator 81160A (with output impedance of $50\ \Omega$). Furthermore, the input and output waveforms were acquired by a high-speed Agilent digital oscilloscope MSO7034B (with input impedance of $2.2\ M\Omega \parallel 12\text{pF}$). Similarly to the measurements in the frequency domain, some additional components were used in order to overcome the problems with unwanted reflection in the ‘off’ state. The termination of the system (a loading resistor) was switched between 50Ω (the ‘on’ state) to 33Ω (the ‘off’ state). Furthermore, in the ‘off’ state there was an additional resistor (75Ω) connected between the output of the arbitrary waveform generator and the ground. The parallel combination of the generator output impedance and the external resistor ($50\Omega \parallel 75\Omega$) changes the effective output impedance to 33Ω . In this way, the line is matched to the generator and unwanted reflections are avoided. Moreover, two connecting coaxial cables (IN to CH1, OUT to CH2) were prepared very carefully in order to assure identical electrical lengths. The repetitive Gaussian pulse (period of 100 ns, -40 dB spectral width of 50 MHz) was used for the excitation. The measured propagation time of the active line in the ‘off’ and the ‘on’ states (thus, the propagation time in air and the propagation time in the non-Foster ENZ metamaterial) is shown in Figure 3-19 (b)). It can be noted that the output pulse in the ‘on’ state indeed comes sooner than the output pulse in the ‘off’ state, despite of its extremely broad spectrum (3 MHz-60 MHz). This is a clear evidence of the broadband superluminal propagation. The measured time advance of 1.25 ns gives the group velocity of $1.61c$, which corresponds well with the frequency-domain results in Figure 3-18 (d). The analysis of the graph in Figure 3-19 (b) also revealed that the -3dB spectral width of the output pulse was increased by 13% in ‘on’ state due to small (but inevitable) dispersion. The amplitude FFT spectra of the input and output waveforms are shown in Figure 3-19 (c). It is clear that the dispersion occurs because there are some spectral components of the input signal that lie above the operating band of the active non-Foster ENZ metamaterial. Due to these ‘missing’ components (and therefore the ‘missing’ fraction of the energy of the input signal), the group velocity is *not equal* to the energy velocity and it does obey causality. Clearly, only the frequency components of the signal that lie within the operating band of the non-Foster negative capacitor travel with the superluminal velocity. This shows that one *should not* analyze these superluminal effects using a simple, dispersionless model of a negative capacitor.

One may immediately ask what would have happened if one had used even broader active ENZ metamaterial, the spectral width of which would have spanned over all the frequency components of the input signal. It is important to understand that the spectrum that covers all the components of the input signal describes *only* the steady state condition. The spectrum will never be finite in the transient state (the switching-on phase of the generator). In the transient state, there is always a fraction of energy (however small it is) that lies outside the operating band and it travels with the speed of light, preserving the causality. Thus, the signal front always travels with the speed of light.

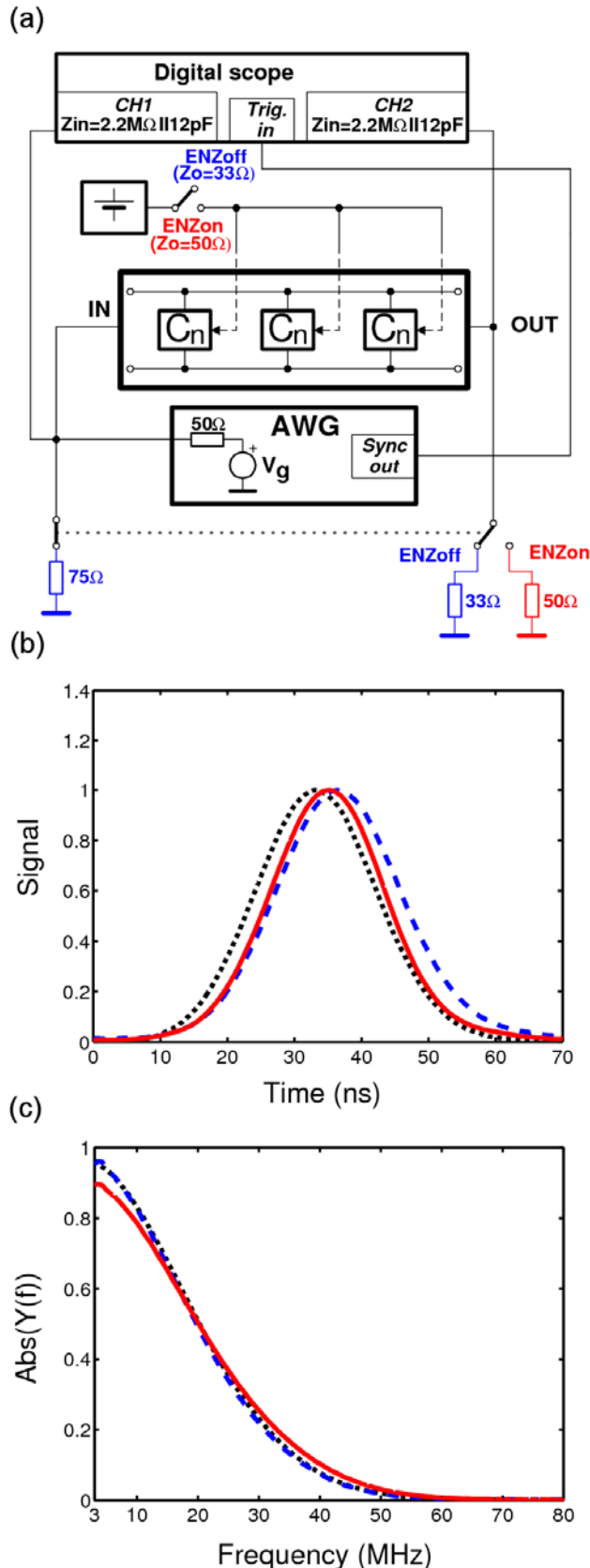


Figure 3-19 Measurements in time-domain, (a) Experimental set-up (b) Time-domain waveforms, (input signal: dashed-black, output signal with ENZ off: dashed-blue, output signal with ENZ on: solid-red), (c) FFT spectra (input signal: dashed-black, output signal with ENZ off: dotted -blue, output signal with ENZ on: solid-red).[80]

3.5 Feasibility of non-Foster ENG/MNG metamaterial

It is well known that an isolated negative capacitor is unstable. In a very thorough analysis in [79] it was shown that the stability does not depend only on the active negative element and its parasitic effect, as it is usually believed. Furthermore, the stability of a non-Foster element also depends on the elements of the external passive network. For instance, let us briefly analyze a case of the isolated negative capacitor. One should not forget that the negative capacitor is actually an amplifier with a capacitor in positive feedback. Theoretically, if the input of the amplifier is left open, both the input and output voltages will be zero and the circuit will be stable. Of course, in reality, there is always some noise present at the input of the amplifier. This noise will appear at the output, as well (however, its level will be increased due to the gain of the amplifier, and it will be ‘modulated’ by the frequency characteristic of the amplifier). Output (amplified) noise will be fed back again to the input, then again amplified e.t.c. Obviously, this process resembles the behavior of an ordinary oscillator and leads to self-oscillations (every signal waveform is allowed in idealized case with an amplifier with infinite bandwidth, while the three-pole models can predict the waveform). In order to stabilize the circuit one should decrease the signal fed back to the input below the level that supports an onset of oscillation. For instance, this can be achieved by an additional ordinary (positive) capacitor C_p connected in parallel to the input (in parallel to the ‘negative’ capacitor). These two capacitors (C and C_p , here C stands for the ‘inverting’ capacitor in the feedback loop) form a voltage divider (please look at Figure 3-1 (b)) described by a simple equation:

$$\frac{v_0(t)}{v(t)} = \frac{C}{C_p + C}. \quad (3.13)$$

From (3.13), it can be concluded that the self-oscillation will occur if $C_p < C$. On the other hand, the circuit will be stable if $C_p > C$. This is actually a well-known analysis of a feedback factor in microwave electronics [17].

The analysis in [46] shows that parallel and series networks that contain non-Foster elements have different stability criteria. Particularly, a 1D transmission line periodically loaded with shunt CC_n circuits (providing that $C > |C_n|$, C being the positive capacitor and C_n being the negative capacitor) shows *stable* ENZ dispersionless behavior. A dual circuit (a transmission line periodically loaded with series LL_n circuits (providing that $L > |L_n|$)) shows *stable* MNZ dispersionless behavior. On the other hand, active ENG and MNG metamaterials should include isolated negative capacitors (inductors) that are unstable. Therefore, in [73] it was mentioned that the ENG and MNG metamaterials do not seem to be feasible in practice.

sign of R	sign of C	sign of L	Stability
+	+	+	Stable
+	-	+	Unstable
+	+	-	Unstable
+	-	-	Unstable
-	+	+	Unstable
-	-	-	Stable
-	+	-	Unstable
-	-	+	Unstable

Table 3-1 Stability criteria for driven positive/negative LC tank circuit [73]

However, one should be very careful in the analysis of this issue. If one looks at Table 3-1, he will find that a series RLC circuit (driven by a generator) is stable in two fundamentally different cases: the case in which all the elements are positive and the case in which all the elements are *negative*. Let us analyze these two cases in more details.

In the case of a familiar passive (positive) RLC tank circuit driven by a sinusoidal signal, a part of the energy is exchanged between the elements and a generator while a part is dissipated. It is clear that below the resonant frequency, majority of the energy is stored in the capacitor C . On the contrary, above the resonant frequency, majority of the energy is stored in the inductor L . That is the reason why the input impedance ‘seen’ from the generator port (Figure 3-20) has a familiar behavior. Now, imagine that one of the elements of the tank circuit has a negative sign. That element (a negative capacitor, for instance), must be of an active type. Therefore, it would act as a new source of energy that would break the balance causing instability.

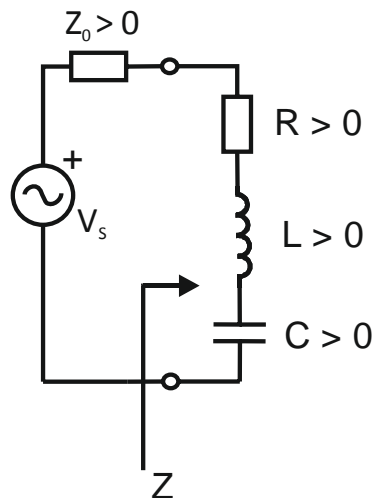


Figure 3-20 Ordinary (positive) series RLC circuit driven by a generator with positive internal resistance

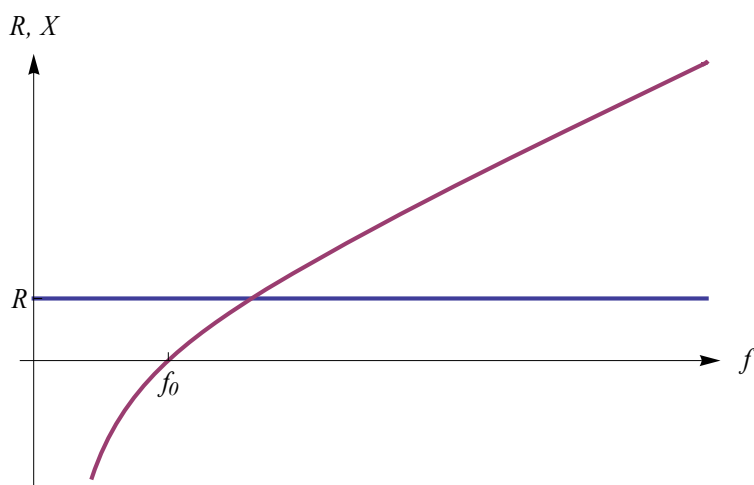


Figure 3-21 Input impedance of an ordinary (positive) series RLC circuit, (blue: R, magenta: X)

Now, let us see what would happen if all three elements of the tank circuit (R, L, C) were negative. According to Table 3-1 such an *isolated* system would be stable (formally, there is a balance of ‘negative’ energy). However, an RLC circuit is in practice always driven

by some generator that, of course, has a positive real part of the impedance. Thus, one would have a combination of positive and negative elements that leads to instability (Table 3-1).

3.5.1 An idea of stable negative RLC tank circuit

Let us now imagine that a generator has a real internal impedance Z_0 that is *lower* than the absolute value of the negative resistance R in the ‘negative’ RLC circuit ($Z_0 < |R|$) (Figure 3-22). The overall resistance would be $Z_0 + R = Z_0 - |R|$ and this is a negative number ($Z_0 - |R| < 0$). Since all other elements are also negative ($L < 0$, $C < 0$), this system should be stable (Table 3-1). The impedance curve of such a negative RLC circuit should be an exact inverse of the impedance curve of an ordinary (positive) RLC circuit (Figure 3-23).

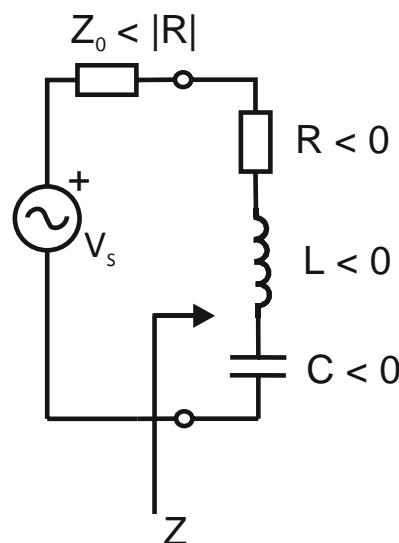


Figure 3-22 An idea of a stable negative non-Foster RLC circuit driven by a generator.

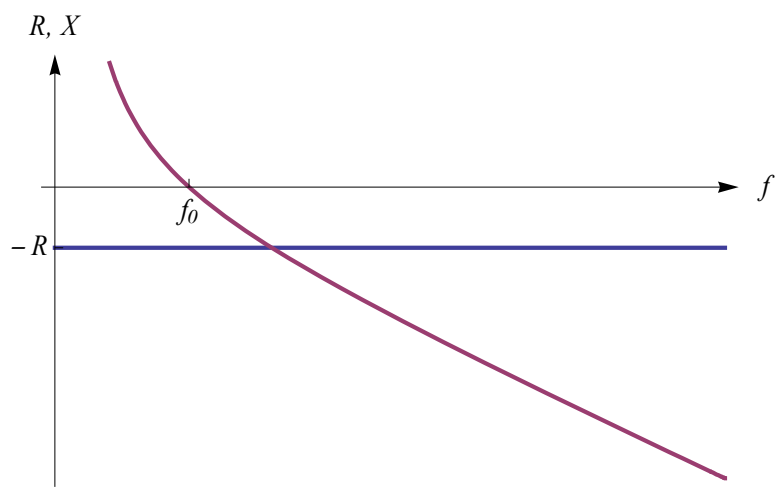


Figure 3-23 Input impedance of a stable negative non-Foster RLC circuit, (blue: R, magenta: X)

Is it possible to test this counter-intuitive idea in practice? At first, one should manage to somehow construct a negative RLC circuit. The first idea is to use a series combination of three NICs terminated with appropriate loads (thus, a series combination of a negative capacitor, a negative inductor, and a negative resistor). Of course, all three negative elements

will always be dispersive i.e. they will become positive at some frequency. This ‘crossing’ frequency must be exactly equal for all three elements (in order to assure stability). This appears to be very challenging. A better way is to use ordinary positive RLC circuit in the feedback loop of INIC (Figure 3-1). This circuit can be connected to the vector network analyzer and (providing that $Z_0 < |R|$) and it should be stable. Thus, it would be possible to measure the input impedance of a negative RLC circuit.

3.5.2 Negative RLC tank circuit RF demonstrator

We attempted this novel idea in practice. At first, we used the AD8099 INIC developed in [73] (Figure 3-3 (a)) and substituted the capacitor in the feedback loop with an RLC circuit. Unfortunately, this system was found to be always unstable. A thorough analysis revealed that the problem occurred due to non-negligible positive/negative conductance generated by the circuit itself (please look at the discussion in section 3.3). It means that one needs a better active element, with broader bandwidth and negligible phase shift. We performed a very detailed survey of all high-speed OPamps available in the market (as mentioned before, the microelectronic technology is not available at the University of Zagreb and, therefore we used of-the-shelf components). After a long survey, and a lot of testing of the purchased samples, it appeared that the THS 4043 amplifier was the best choice for the RF demonstrators of non-Foster elements and associated metamaterials. The THS4303 device is a wideband, fixed-gain amplifier that offers high bandwidth of 1.8 GHz at a nominal gain of 10, high slew rate (5500 V/μs), low noise, and low distortion. This combination of specifications enabled us to overcome the performance limitations experienced with the previously used AD8099 amplifier. The main improvement over the AD8099 comes from the internal negative feedback which lowers the parasitic capacitance from inverting the input of the operational amplifier to the ground. Therefore, higher rollover frequency and a wider frequency span of the negative capacitance are possible. Also, the gain of the amplifier is not fixed since one terminal of the gain setting resistor is left open. This allowed us to trim the overall gain easily by connecting an additional resistor in series between this terminal and ground. Additional improvements come from the package, that is significantly smaller than the packages of previously used amplifiers, minimizing serial parasitic inductance and capacitance.

The negative RLC circuit was designed as an INIC using the approach detailed in [73] and the final circuit diagram is sketched in Figure 3-24 (a). Briefly, the gain of the amplifier itself ($A=10$) was lowered to $A=3$ with an additional resistor (220Ω). The resonance of the RLC circuit in the positive feedback loop ($R=470 \Omega$, $L=100 \text{ nH}$, $C=100 \text{ pF}$) was chosen to be approximately 55 MHz, which is well below the maximal frequency of the NIC inversion (700 MHz) that should assure stable operation. A photograph of the assembled prototype is depicted in Figure 3-24 (b). The input reflection coefficient was measured with the help of an ZVL Rohde Schwartz network analyzer and the extracted reactance and resistance values are shown in Figure 3-25. It can be seen that the slope of the reactance curve is indeed opposite to the slope of the associated curve of a classical positive RLC circuit. The curve crosses zero at the frequency of 60 MHz indicating the resonance. In addition, the resistance is negative and its curve approximately flat within the analyzed frequency band. The most important and counterintuitive fact is that this circuit is stable. To the best of our knowledge, this is the first demonstration of a negative non-Foster RLC circuit. We believe that this finding may pave a way towards non-Foster ENG and MNG metamaterials that have appeared not to be feasible so far.

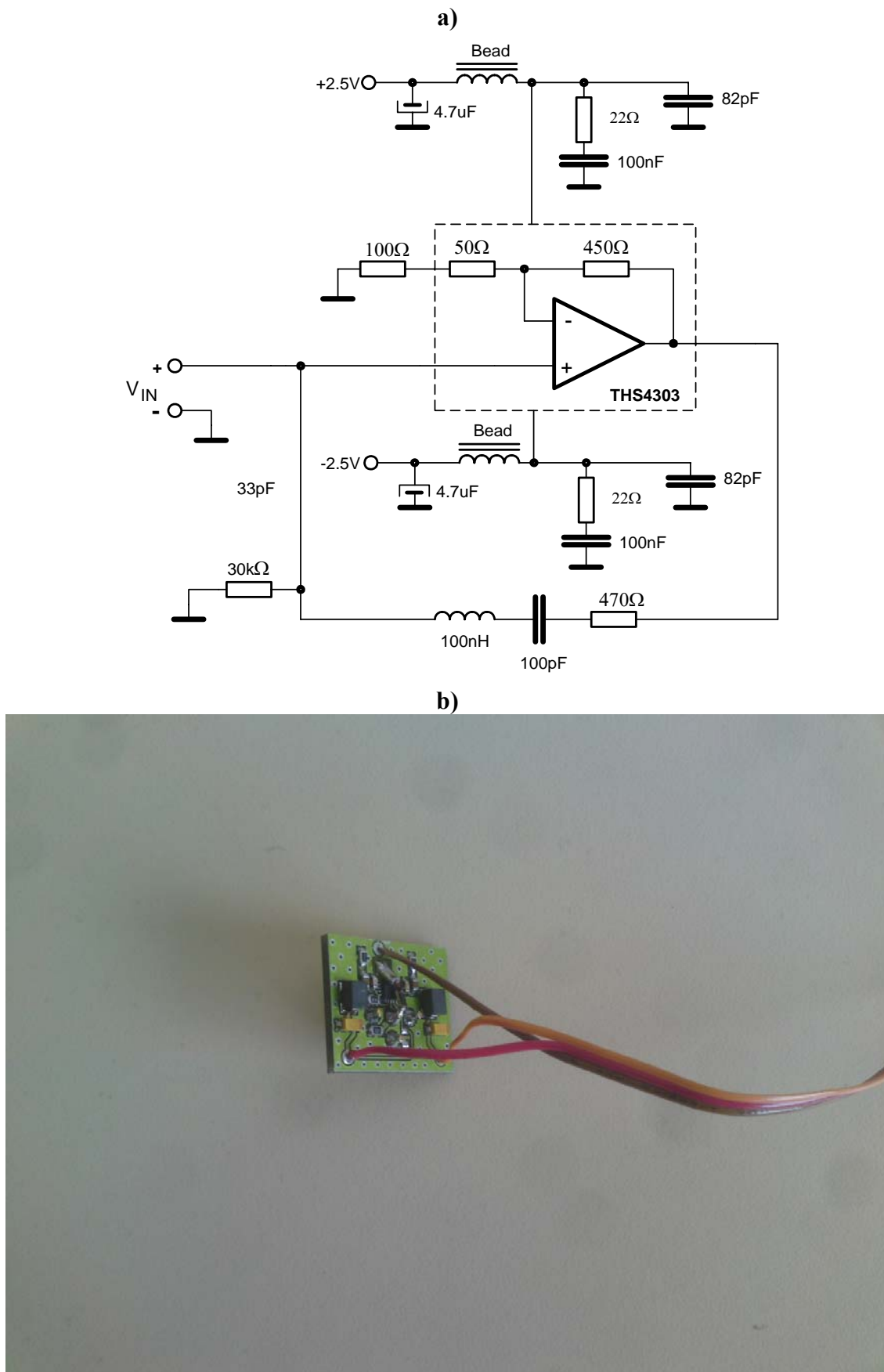


Figure 3-24 a) Circuit diagram of the negative non-Foster RLC circuit **b)** - Photograph of the manufactured negative non-Foster RLC circuit

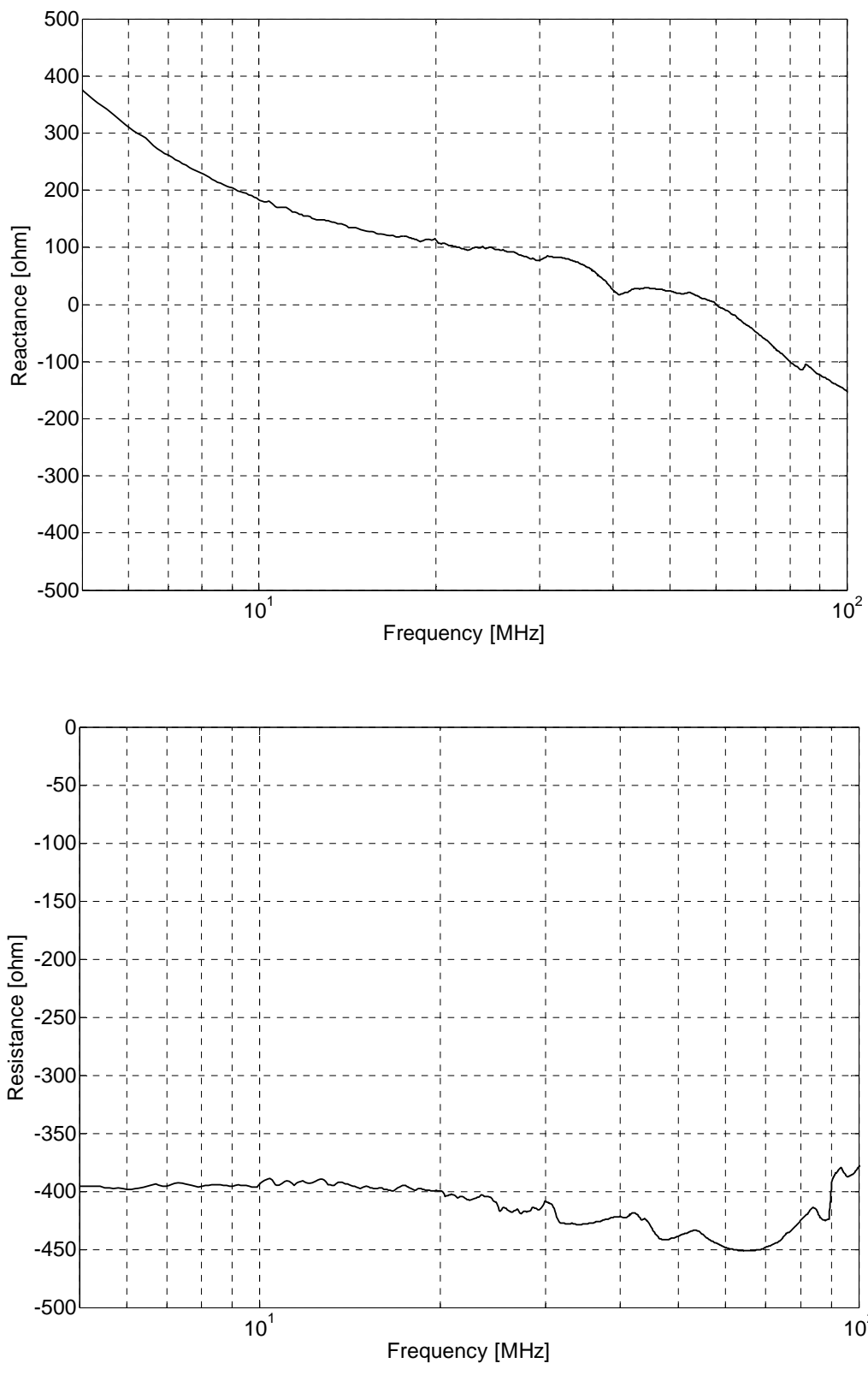


Figure 3-25 , (a) – Measured imaginary part of the impedance of the negative RLC circuit **(b)** - Measured real part of the impedance of negative RLC circuit

3.5. Summary

Some unclear issues of the basic physics of practical non-Foster metamaterials have been analyzed in this chapter. The most important findings are summarized below:

- Commonly used ‘mathematical’ dispersionless model of an ideal non-Foster negative capacitor is non-causal and it might be used only for the crude prediction of the qualitative behavior within a finite bandwidth. Outside this band, the model should not be used at all (even for qualitative analysis) because it gives unphysical behavior.
- A simple, more realistic three-pole model of a dispersive negative capacitor is proposed. This model showed very good agreement with both the SPICE-based simulations and the measurements on the manufactured prototypes across the whole operating bandwidth. The model is capable of prediction of both basic physical phenomena and accurate dispersion characteristic.
- The understanding of the basic physics of a negative capacitance phenomenon was improved by the analysis of a response of the negative capacitor to a pulse excitation using a developed low-frequency demonstrator based on a commercial integrated audio amplifier. All the measurements show that a negative capacitor could be interpreted as a generator/sink. In addition, performed experiments explained clearly the physics of the ENZ behavior and negative capacitance ‘boosting’ phenomenon.
- A detailed experimental investigation of the recently observed simultaneous superluminal phase and group velocities in non-Foster ENZ metamaterials has been performed both in the frequency and time domain. It was found that, although being counter-intuitive, this behavior is in a perfect agreement with the causality requirements. However, for the correct interpretation of the results one must use a dispersive model of a realistic negative capacitor.
- The basic physics of a negative non-Foster RLC tank circuit is investigated. A simple analytical study revealed that this circuit is stable if it is driven by a generator, internal resistance of which is smaller than the absolute value of the negative resistance. The prototype operating in the lower RF region (up to 70 MHz) has been designed and manufactured, and the measurements of the input reflection coefficient indeed showed a stable behavior. To the best of our knowledge, this is the first experimental demonstration of a stable negative RLC tank circuit. This approach might pave a way towards non-Foster ENG and MNG metamaterials that have appeared not feasible so far.

Chapter 4 Towards more versatile non-Foster metamaterials

4.1 Previous work: Technological constraints of state-of-the art non-Foster metamaterials

The first paper that theoretically discussed a possible use of active non-Foster elements in metamaterials was published in 2001 [25]. This paper analyzed the equations for the polarizability of metamaterials based on short loaded dipoles and small loaded loops. It was shown analytically that a loading of a short dipole with a *negative capacitance* (instead of an ordinary, positive inductance) should lead to a wideband dispersionless ENG behavior. Similarly, the loading of a small loop with a *negative inductance* (instead of an ordinary, positive capacitance) should lead to a wideband dispersionless MNG behavior. It is important to stress that, in this case, the bandwidth would be limited only by the bandwidth of the realized non-Foster element. Thus, one might expect multi-octave bandwidth, which would be a significant progress in the metamaterial field. The authors in [25] also proposed active ‘impedance sheets’ (i.e. very thin metamaterials) with ENG or MNG properties. In conclusion, it was noted that the required negative non-Foster elements appear to be feasible at the lower end of RF range using available technology (OPamps). However, the subsequent theoretical study [26] revealed that the ‘isolated’ dispersionless ENG and MNG metamaterials based on negative non-Foster elements are inherently unstable (usually, it is an accepted rule that a sum of the capacitances (or inductances) along a closed mesh is a positive number). Due to stability problems, the ENG and MNG metamaterials have appeared not to be feasible in practice, at least so far (please look at the discussion in the section 3.5). Following the original idea from [25] the authors in [27] theoretically investigated the stability of an array of small loops loaded with non-Foster reactive elements. Surprisingly, it was found that such a metamaterial can be stable, but only if the array is infinitely large. In this case (that is probably non-practical), the predicted MNG behavior was not entirely dispersionless, but the estimated bandwidth was significantly larger than a bandwidth of passive metamaterials.

The first practical realization of a non-Foster-based active dispersionless ENZ metamaterial was developed in our group, presented in [65] and further improved in [66]. The negative capacitors were constructed using discrete FET-based circuits incorporated into a 2D microstrip unit cells. Measurement of the equivalent effective permittivity showed fairly constant ENZ behaviour ($0.25 < \epsilon_r < 0.35$) within one octave (1 GHz-2 GHz) [66]. In the subsequent study [74] a complete 1D active RF ENZ metamaterial (based on an air transmission line loaded with three op-amp-based negative capacitors) was analysed, built and tested. The measured real part of the effective permittivity was rather constant (it varied from 0.27 to 0.37) in the frequency range 2 MHz-40 MHz (the bandwidth of more than four

octaves). This bandwidth is significantly wider than the bandwidth of any passive ENZ metamaterial. In addition, it was found that this type of line supports counter-intuitive (but causal) superluminal phase and group velocities [80].

It is important to understand the technological problems of non-Foster elements. The first limitation is the transit frequency (f_t) of the active element itself. In [73] it was pointed out that this frequency should be at least ten times higher than the maximal operating frequency of the non-Foster element. This comes from a very simple fact that the operation of all NIC circuits is based on either voltage or current inversion. The inversion requires no phase shift between the input and the output of the active device (zero-degree phase shift). This can be achieved only at very low frequencies, for which the transit time across the active device can be neglected. As ‘a rule of thumb’ one can say that the f_t should be ten times higher than the maximal operating frequency of a non-Foster element. The drawback of the high transit frequency is that it makes the circuit more prone to unwanted oscillations due to unavoidable parasitic capacitances and parasitic inductances within the circuit. Of course, this problem is further pronounced due to inherent instability of the non-Foster elements caused by the existence of the positive feedback.

All non-Foster metamaterials developed in our group (to the best of our knowledge there are no other successful practical realizations published so far) were ‘hand-crafted’, using either discrete BJTs, FETs or OPamps. Achieved maximal frequency of operation was below 100 MHz (except examples in [66] that operated in the 2 GHz band, but with the problem of repeatability of ‘hand-crafted’ prototypes). Most of the devices constructed in our group used high-speed OPamps [65-68,73-78]. They are cheap and the associated NIC designs are very simple, without complicated DC bias networks. In addition, the repeatability of the manufactured circuits (even in the case of simple ‘hand-crafting’) is excellent. The only drawback is the worse noise performances comparing to BJT and FET technology. Therefore, the OPamp technology is very convenient for the construction of proof-of-concept demonstrators of active non-Foster metamaterials. So far, the ENZ metamaterial that used OPamp technology operated up to the frequency of 40 MHz, thus in the lower RF band.

Much better results could be expected if one used microelectronic technology. The reason for this is very simple: parasitic capacitances and inductances may significantly influence the operation of practical non-Foster elements (due to the inherent positive feedback, which is very sensitive to an additional phase shift). To the best of our knowledge there is only one successful realization of an integrated microelectronic non-Foster element (negative inductance) [98]. At the same time, this is the only realization of a negative inductance operating in the UHF band. In [98] authors developed stable variable negative inductance that can be adjusted from -60 nH to -20 nH up to the frequency of approximately 600 MHz. This paper probably presents the state-of-the art in non-Foster elements from a technological point of view. Unfortunately, the used technology (IBM 8 HP BiCMOS process) is very expensive and not available for many research groups. In addition, no attempts to use this microelectronic version of the negative inductance in the broadband metamaterial have been published so far. In the subsequent paper, the same group used the developed negative inductance for the realization of a broadband PMC surface in antenna technology [99]. These are certainly important contributions, but they use very expensive technology.

Therefore there are (at least in our opinion) two important issues that are not clear at the moment:

- Is it possible to extend the operating frequency of negative capacitors based on discrete elements (and associated metamaterials) into the UHF band?

- Is it possible to add the reconfigureability/tuneability feature to these metamaterials?

4.2 Increase of the maximal operating frequency: Negative capacitor demonstrator

In this section we report our efforts toward the increase of the maximal operating frequency of a negative capacitor into the UHF band.

4.2.1. Initial design based on OpAmp(100 kHz - 450 MHZ)

For the construction of a negative capacitor we used an OPamp INIC approach detailed in [73] and briefly reviewed here in Figure 3-3. The selected OPamp was a THS 4304 and the initial circuit is depicted in Figure 4-1. As in the case of a negative RLC circuit, (3.5.2), the gain of the amplifier itself ($A=10$) was lowered to $A=3$ with the additional resistor (220Ω). The value of the inverting feedback capacitor was quite low (1.7 pF) and it was chosen as a compromise between a wideband operation and an acceptable dispersion. With this capacitance value, SPICE-based circuit simulation predicted generated negative capacitance of -5 pF with the maximal operating frequency of approximately 700 MHz. In addition, the ‘swamping’ stabilizing capacitor of 33 pF was added to the circuit. Designed negative capacitor was prototyped at 0.6 mm thick FR4 substrate and it used high quality 0805 SMD components. The PCB layout of the prototyped device is shown in Figure 4-2 and its photograph in Figure 4-3. Please note that, for the sake of initial testing, the PCB was equipped with an SMA connector.

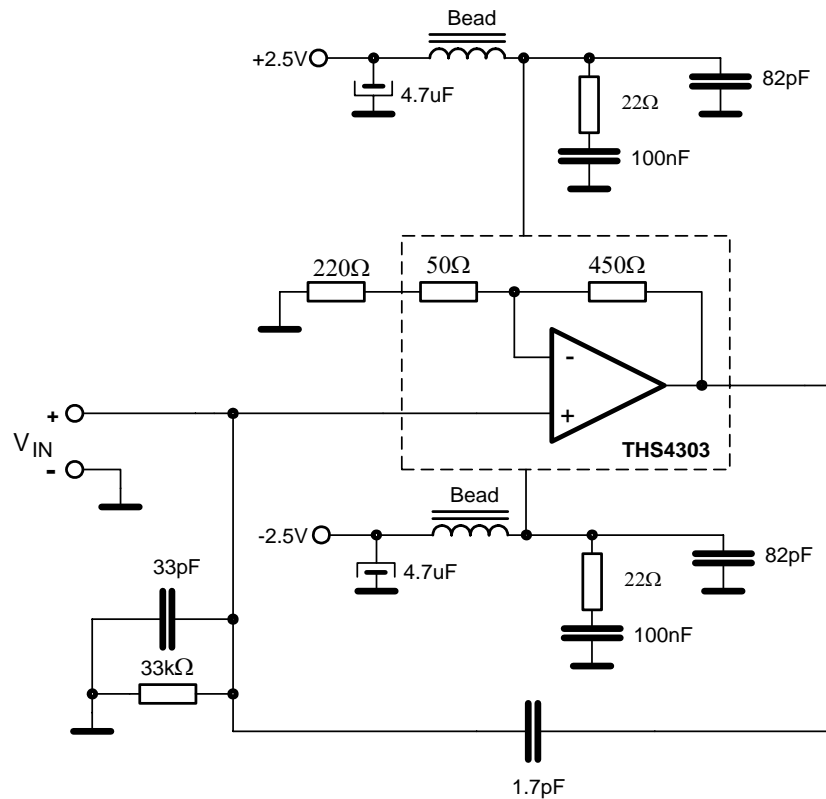


Figure 4-1 Circuit diagram of the initially designed negative capacitor demonstrator (100 kHz – 450 MHz)

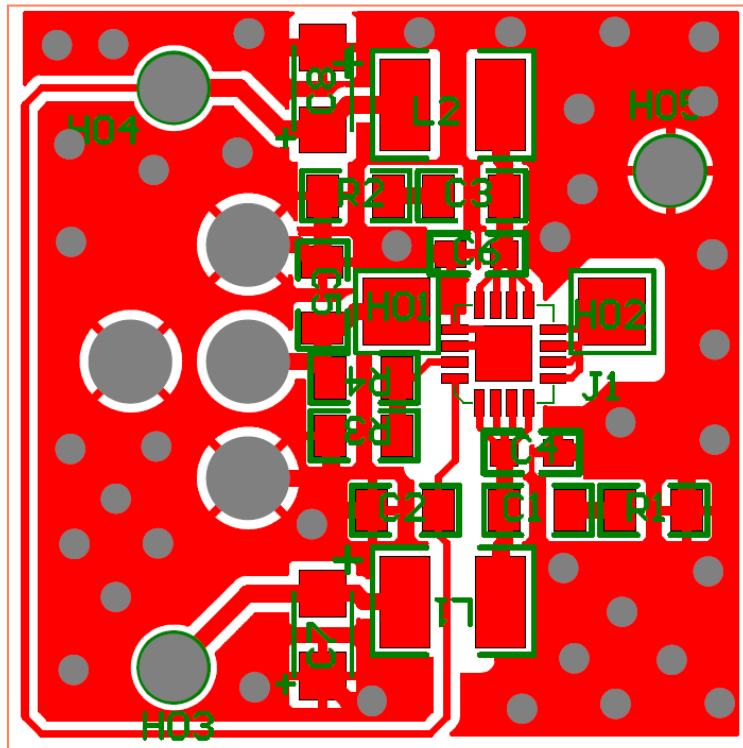


Figure 4-2 PCB layout of the initially designed negative capacitor demonstrator (100 kHz – 450 MHz)

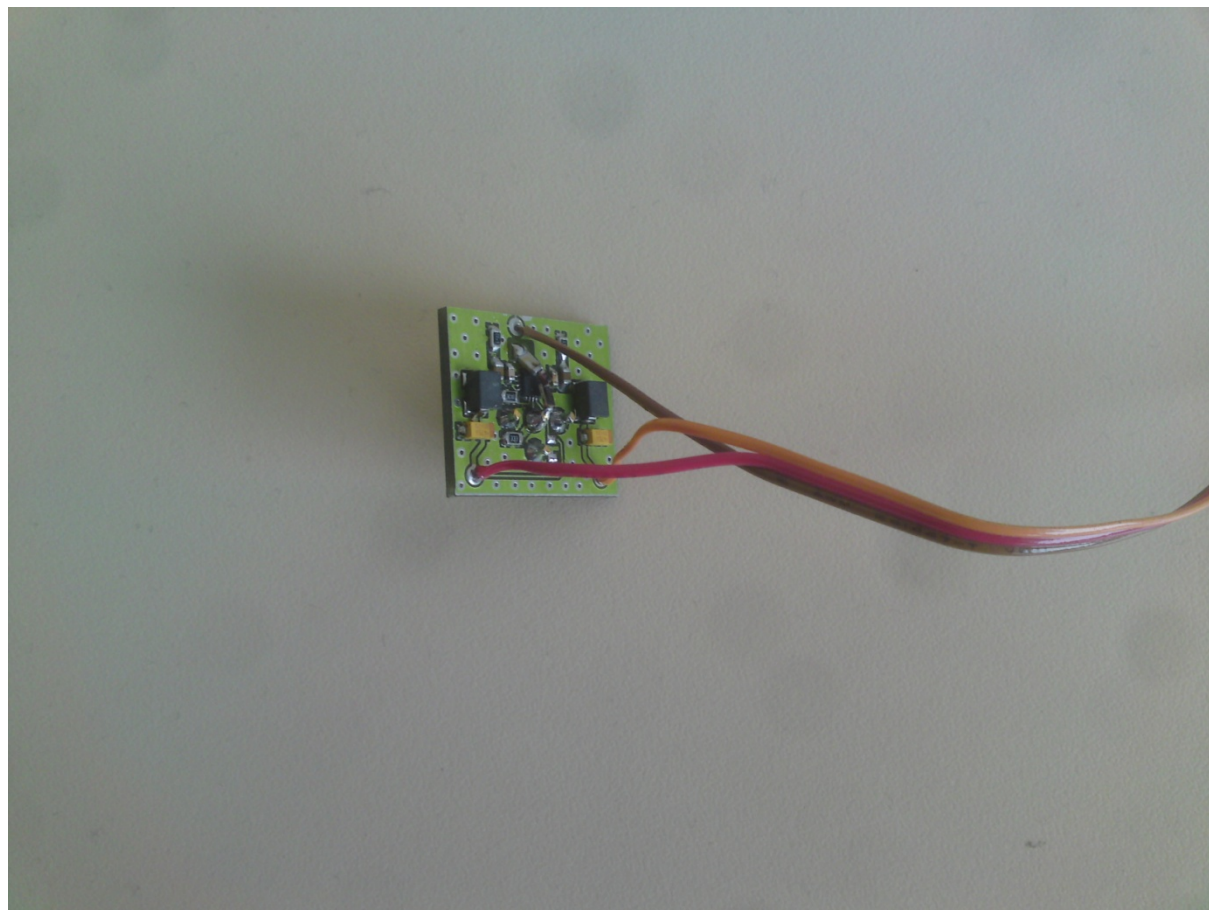


Figure 4-3 Photograph of the initially designed negative capacitor demonstrator (100 kHz – 450 MHz)

The first measurements (using an ZVA 40 VNA), after the de-embedding of a ‘swamping’ 33 pF capacitor, showed unexpectedly dispersive negative capacitance, with the maximal operating frequency of approximately 450 MHz (not shown in the figures). After thorough investigation it was found that this behavior was caused by an unwanted parasitic tracks inductance and pad capacitance. So, we estimated the values of these parasitics using a simple quasi-static approach. Then, the appropriate lumped elements were incorporated into the circuit diagram and the SPICE-based simulation was repeated. Obtained results (compared with the measurements) are shown in Figure 4-5. It can be seen that now the simulated values match the measurements quite well, highlighting the importance of proper handling of the parasitic effects. Furthermore, it was found that the use of an microwave VNA (such as Rohde Schwartz ZVL 40 that operates from 10MHz to 40 GHz) is problematic for the measurements of these non-Foster circuits. The problem appears due to pronounced noise in the lower part of the measurement range that significantly decreases the measurement accuracy. This noise is a consequence of a complicated harmonic and sub-harmonic mixing that is usually used in the VNAs that cover RF and microwave bands. It was found that it is better to use a RF VNA that has a better noise figure at low frequency (please compare the differences among the results in Figure 4-5 a), b) and c)).

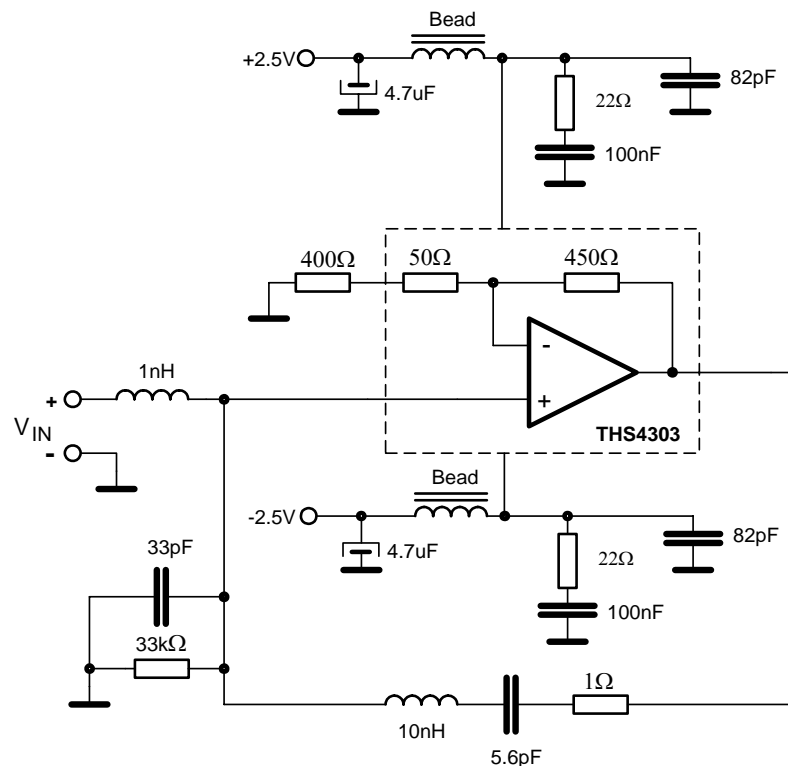


Figure 4-4 Circuit diagram of the initially designed negative capacitor demonstrator (100 kHz – 450 MHz) with parasitic effects included

Furthermore, it was attempted to investigate the sensitivity of the PCB layout on the properties of the manufactured negative capacitor. It was done by tuning the values of the parasitic track inductances and pads capacitances. It was found that the two most sensitive parameters were the length of the track in the feedback loop and the length of the input track that connects the negative capacitor to an SMA connector (i.e. the track parasitic inductances). Just a slight change of the track length (in order of 1 mm) significantly alters the performances of the circuit. Therefore, it was decided to perform a new design cycle, in which the lengths of all the connecting tracks were minimized.

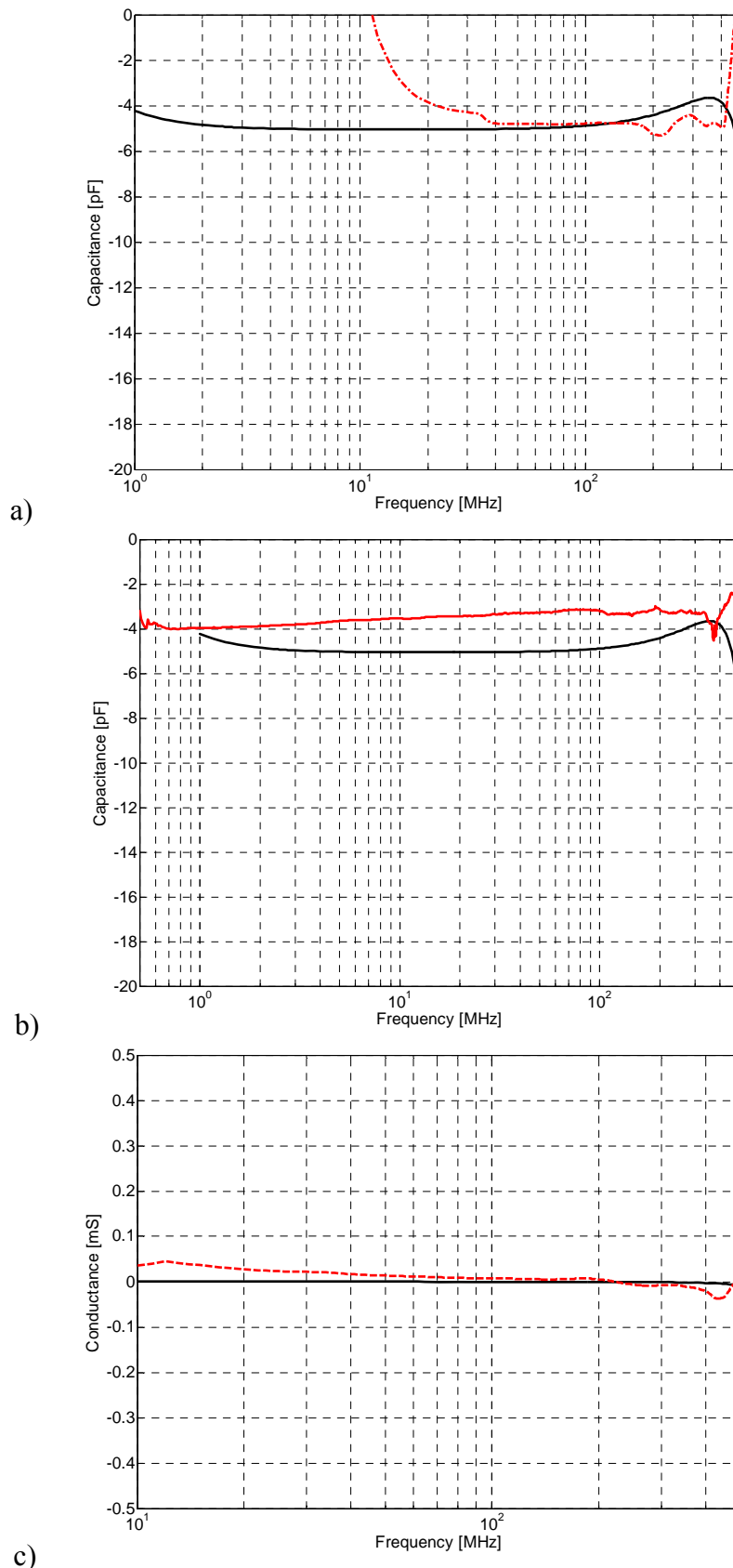


Figure 4-5 Measurements of the initially designed negative capacitor demonstrator a) generated capacitance (solid black – simulations, dashed red - measurements) (measured with an ZVA 40VNA) b) generated capacitance (solid black – simulations, dashed red - measurements) (measured with the help of an ZVL 8 VNA) c) generated conductance (solid black – simulations, dashed red - measurements) (measured with an ZVL 8 VNA)

4.2.2. Improved design based on OpAmp (100 kHz - 700 MHz)

The circuit diagram (with included parasitic effects) of a new prototype and the associated optimized PCB layout are shown in Figure 4-6 and Figure 4-7, respectively. Measured values of the extracted effective parameters are given in Figure 4-8.

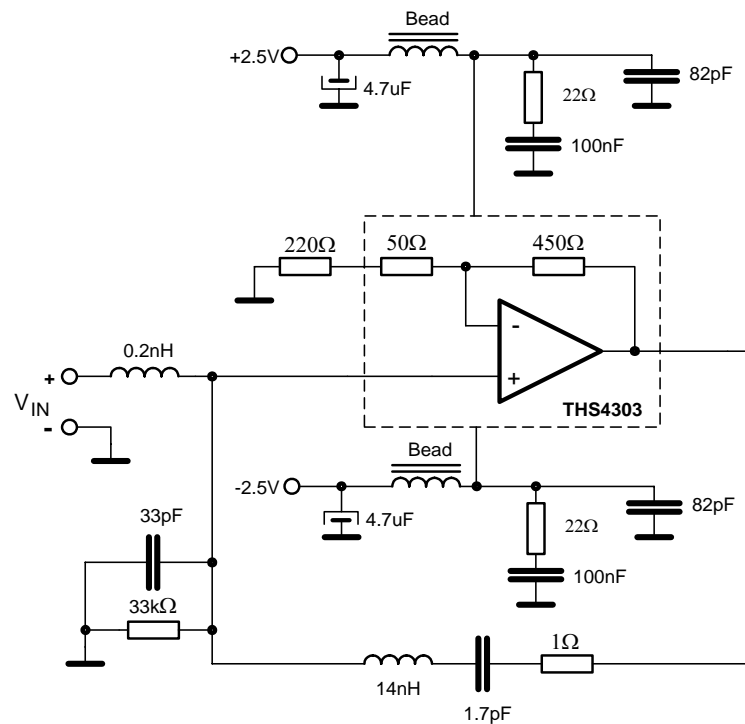


Figure 4-6 Circuit diagram of the improved design of the negative capacitor demonstrator (100 kHz – 700 MHz) with included parasitic effects

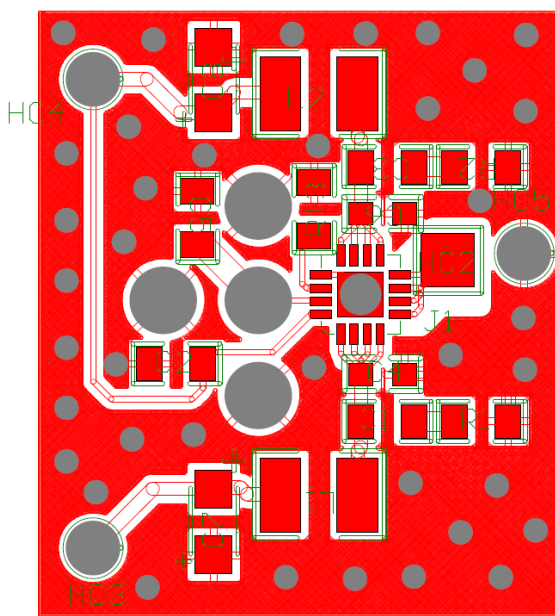


Figure 4-7 PCB layout of the improved design of the negative capacitor demonstrator (100 kHz – 700 MHz)

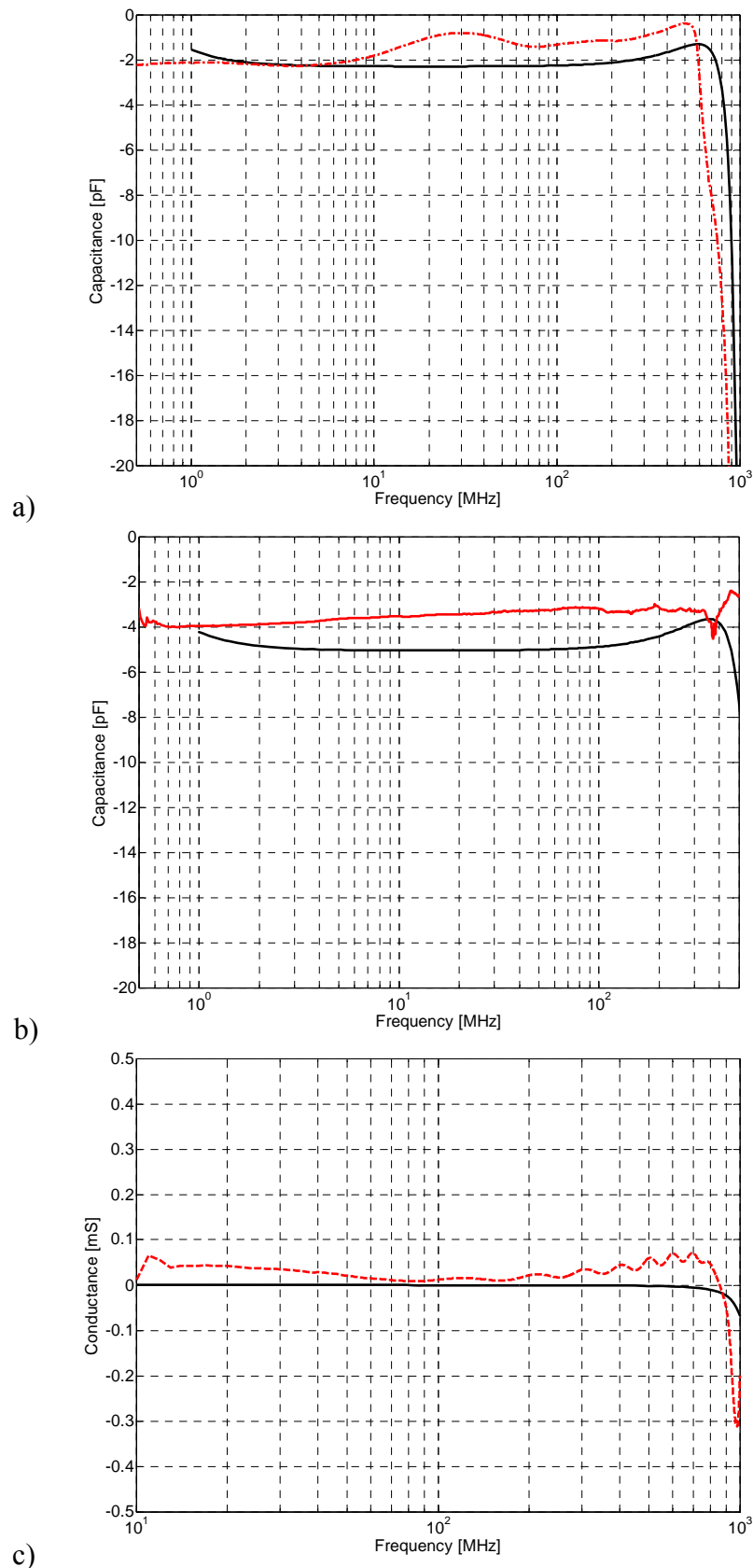


Figure 4-8 Measurements of the improved design of the negative capacitor demonstrator a) generated capacitance (solid black – simulations, dashed red - measurements) (measured by an ZVA 40 VNA) b) generated capacitance (solid black – simulations, dashed red - measurements) (measured with the help of an ZVL 8 VNA) c) generated conductance (solid black – simulations, dashed red - measurements) (measured with an ZVL 8 VNA)

At first, it can be seen (Figure 4-6) that the parasitic inductance at the input is greatly reduced (from 1 nH to 0.2 nH) by shortening the input track (Figure 4-7). Secondly, the resonance between the inverting capacitor and the parasitic inductance (14 nH and 1.7 pF) was moved further away from the operating region. These changes improved the operating bandwidth that now spans from 100 kHz up to almost 700 MHz (it was difficult to determine the accurate maximal frequency due to a problem with calibration of the reference plane). Actually, it was found that the inductance of an SMA inner pin also affects the results. Additional simulations showed that a structure that would use a negative capacitor without the connector should have maximal operating frequency above 700 MHz. In spite of the experienced difficulties, it was proven possible to push the operation frequency of a negative capacitor into the UHF range using cheap, commercially available OPamps. We believe that these results can hardly be improved without the use of the microelectronic technology.

4.2.3. The ENZ unit cell

Finally, the developed negative capacitor was used as a part of a simple 1D ENZ unit cell (similar to that used in [73]) in which a (positive) capacitance of the host line had a value of 5 pF/cell. Extraction of the measured parameters showed that it was possible to obtain an equivalent relative permittivity of $0.7 \pm 15\%$ in the frequency band 100 kHz-700 MHz. By lowering distributed capacitance of a host line (or by adding additional positive capacitor) it is possible to lower relative permittivity down to the value of 0.2.

4.3 Increase of the maximal operating frequency: Negative inductor demonstrator

(*The part of the results presented in the sections 4.3.1. and 4.3.2 were achieved with the help of Eduardo Ugarte Muñoz, who is a Ph.D student at Universidad Carlos III de Madrid).

In order to build an MNZ unit cell, one would need a negative inductor. Unfortunately, the literature available in public is sparse of studies that report successful realization of a stable non-Foster negative inductor in the RF range. We are aware of only two papers and they use expensive microelectronic technology [98,99]. Since microelectronic technology is not available at the University of Zagreb, it was attempted to prove the basic ideas using two cheap approaches: discrete FET transistors and commercially available high-speed OPamps. The final goal is to build a negative inductor that operates in the range 100 kHz-700 MHz (similarly to the negative capacitor developed in the previous section). In this way, it would be possible to combine negative capacitors and negative inductors in various types of ENZ/MNZ unit cells and associated metamaterials.

4.3.1 Design based on Kolev's circuit with FETs (1 MHz – 50 MHz)

Kolev's circuit (also known as Meunier-Kolev circuit) is an active network that does inversion of the load impedance [59]:

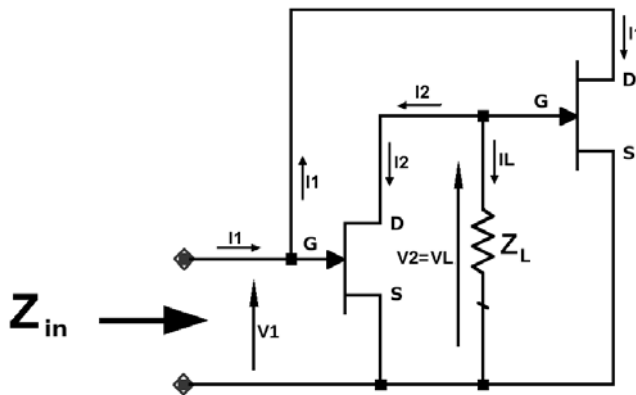


Figure 4-9 Kolev-Meunier's circuit

A simple and a straightforward analysis [73] showed that the input impedance is proportional to a negative inverse of the load impedance:

$$Z_{\text{in}} = -\frac{1}{g_{m1}g_{m2}Z_L} \quad . \quad (3.14)$$

Here, g_{m1} and g_{m2} stand for the transconductances of the FETs, while Z_L is the load impedance. So, if Z_L is an inductor, the input impedance will behave like a negative capacitance and this property was used in [59,73]. Here, we propose to use this circuit for the generation of a negative inductance by a simple use of a capacitor as the load Z_L . At first, the circuit simulation of the Kolev's circuit that contains both ideal FETs and realistic SPICE models of BF999 Si MOS FETs was performed. A sample of the obtained results is shown in Figure 4-10 and Figure 4-11. The analysis of these figures shows that the circuit based on ideal FETs generates almost ideal negative inductance up to a frequency of approximately 500 MHz. On the other hand, a realistic case with BF999 FETs shows good behavior up to a frequency of 200 MHz (the reactance curve closely follows the curve of an ideal negative conductor). However, the existence of non-negligible real part of the input impedance limits the maximal operation frequency to approximately 50 MHz.

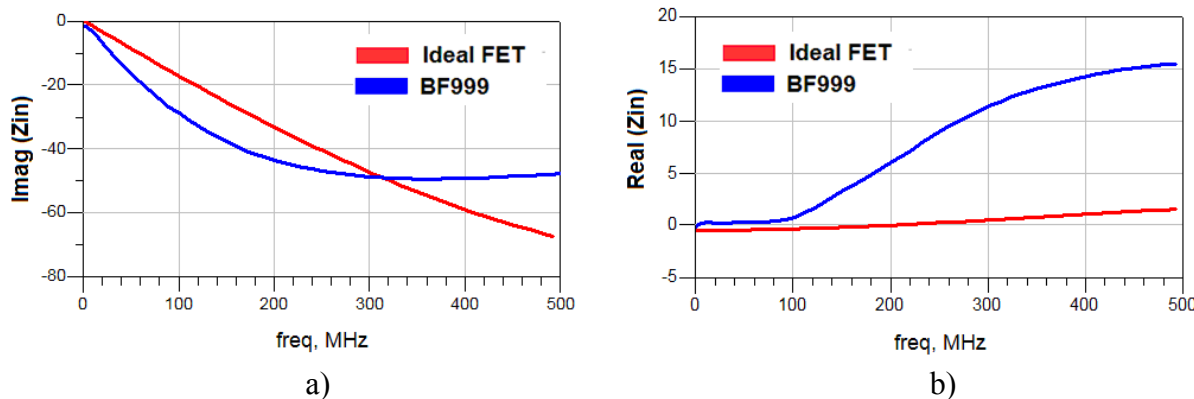


Figure 4-10 Simulated input impedance of the Kolev's circuit, a): imaginary part , b) real part

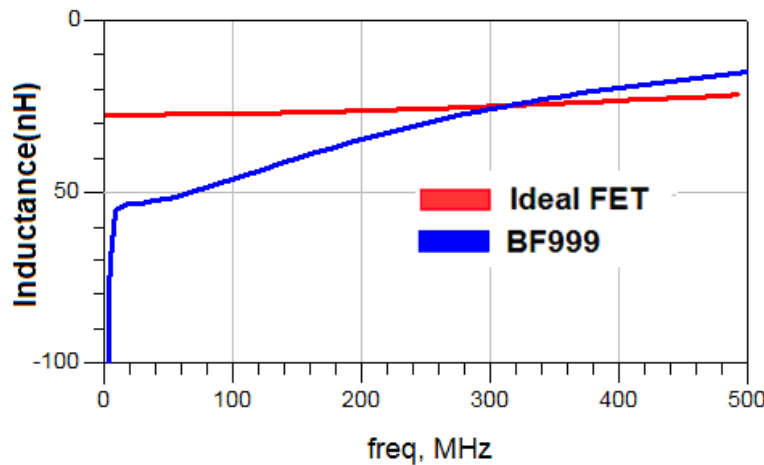


Figure 4-11 Simulated negative inductance of the Kolev's circuit

We manufactured and tested a variant of the Kolev's circuit that operates as a negative inductor. Complete circuit diagram (including the biasing networks) and the photograph of the prototype are shown in Figure 4-12 and Figure 4-13, respectively.

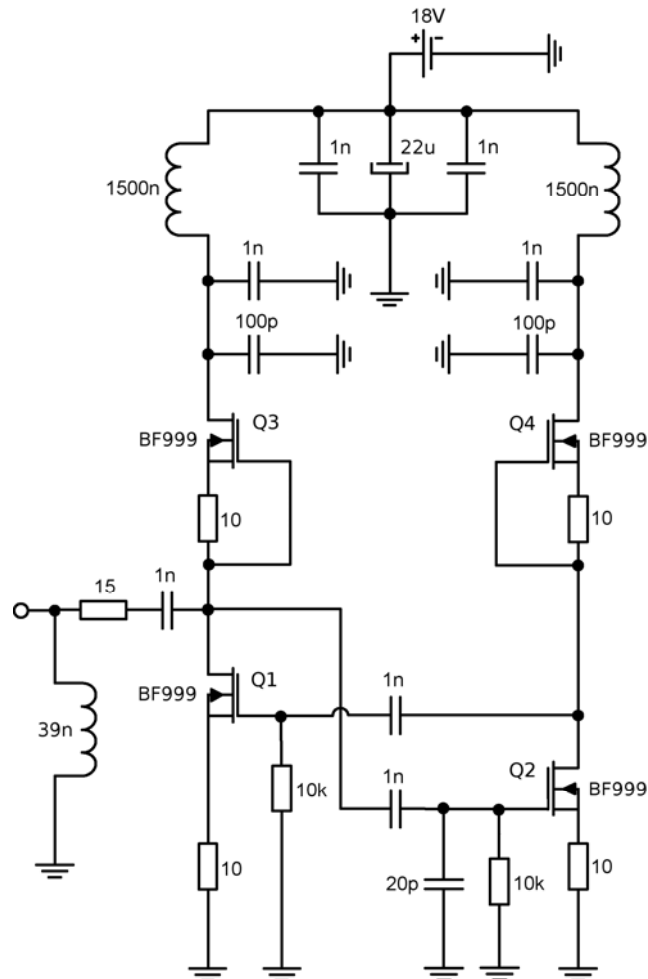


Figure 4-12 Schematic diagram of the manufactured prototype of a negative inductor circuit based on Kolev's topology

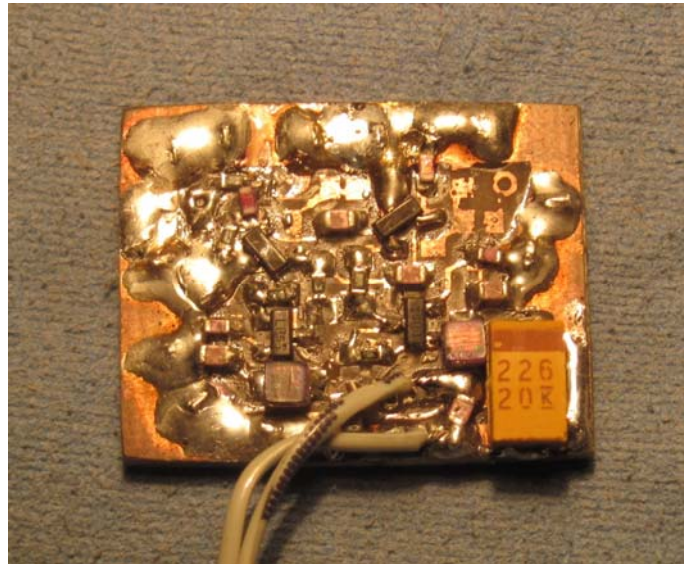


Figure 4-13 Photograph of the manufactured prototype

There are some practical aspects of the basic circuit:

- UHF silicone depleted-type MOSFETs $Q1$ and $Q2$ are the main active devices
- $Q3$ and $Q4$ are the current sources that provide the drain currents for $Q1$ and $Q2$, respectively.
- $C = 20 \text{ pF}$ is the load capacitor
- DC decoupling capacitors of 1 nF are used in the feedback paths as well as for the input decoupling
- The filters consisting of a parallel combination of 100 pF and 1 nF capacitors and a 1500 nH choke are used to block the RF signal from the power supply paths
- $10 \text{ k}\Omega$ resistors are used for setting the $Q1$ and $Q2$ gate bias voltage at $V_g \approx 0 \text{ V}$. Those behave as high impedance for the RF signals.
- The purpose of the 10Ω resistors connected in series with the MOSFETs is to balance the V_{DS} of $Q1-Q4$, keeping it close to 9 V , thus assuring a decent voltage swing on each transistor.
- A 15Ω resistor, connected in series with the input, partially compensates the negative resistance, occurrence of which is inevitable in this type of an impedance inverter.

As mentioned before, a negative inductor by itself is unstable (therefore, it will not be possible to measure it by a network analyzer) if it is not compensated at the input to obtain an overall positive inductance. It seems logical to conclude that the correct way to compensate a negative inductor would be by placing a series positive inductor (inductance of which is larger than the modulus of the generated negative inductance), so that $L_{total} = L_{positive} - |L_{negative}|$ is a positive number. However, the first measurements of the Kolev's circuit from Figure 4-12 showed instability. On the other hand, it was found that the circuit was stable when a positive shunting inductor (39 nH) was connected at the input. Thus, we used an additional shunt positive inductor in the extraction procedure (the stability analysis that explains why this is necessary, is presented later in this chapter).

Measured reflection coefficient of the prototype (obtained with the help of an ZVL 8 Rohde Schwartz VNA) and the extracted equivalent input impedance are shown in Figure 4-14 and Figure 4-15, respectively.

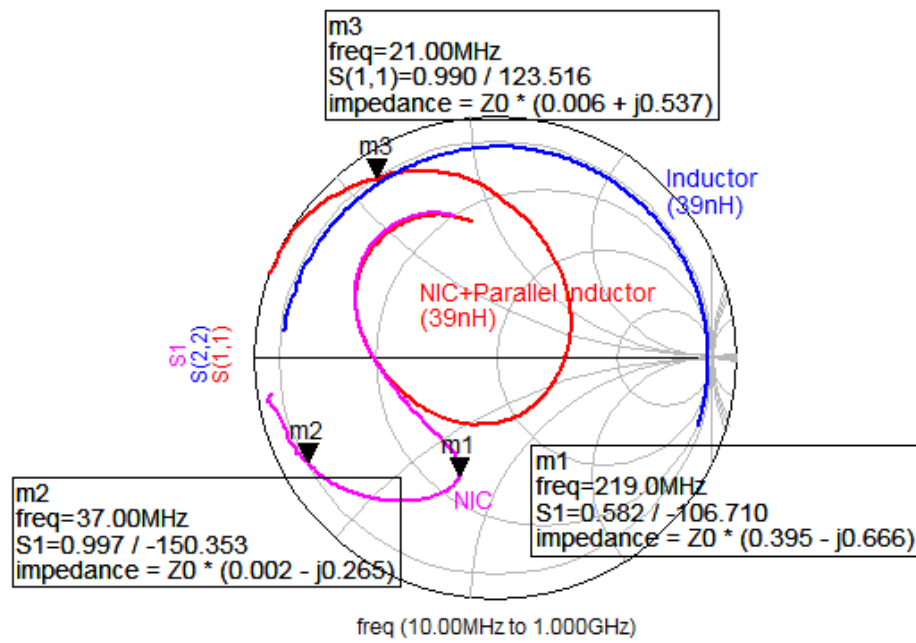


Figure 4-14 Measurements of the reflection coefficient of the Kolev's circuit. Blue: the stabilizing inductor 39 nH, red: the circuit shunted with the stabilizing inductor, magenta: de-embedded reflection coefficient)

From the measurement results presented in Figure 4-14, one could conclude following:

- The input impedance has a negative real part up to 37 MHz.
- For the frequencies from 10 MHz to 200 MHz the input impedance behaves as a negative inductance.
- For the frequencies above 200 MHz, the input impedance does not behave as a negative inductance (The magenta locus in Figure 4-14 shows clockwise rotation with the respect to the frequency)

The real and imaginary parts of the input impedance are presented in Figure 4-15. It can be seen that these results agree well with the results from the simulation (Figure 4-10). Thus, the circuit behaves as a negative inductance for the frequencies up to 200 MHz. However, the real part of the input impedance can be neglected for the frequencies up to 50 MHz. This issue is explained in details in

Figure 4-16.

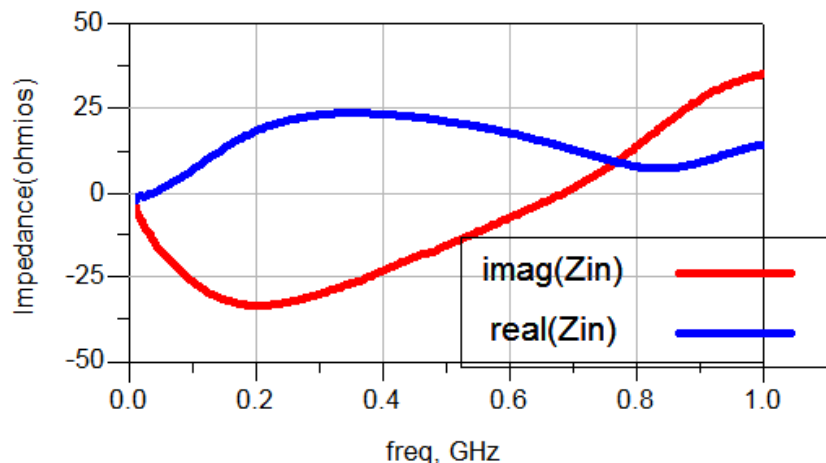


Figure 4-15 Input impedance of the measured negative inductance circuit

It presents the comparison of the simulated and the measured impedance in the frequency range 10 MHz-200 MHz. It can be seen that the behavior of the input impedance can be approximated with the behavior of an ideal -60 nH inductor. The real part of the input impedance is quite small (it is lower than 10 Ω for $f=100$ MHz, but it becomes slightly negative at the frequencies below 37 MHz). This negative resistance (that can lead to instabilities) can be compensated by increasing the value of a series 15 Ω resistor at the input, but at the cost of more pronounced losses at higher frequencies. Thus, the realized circuit behaves closely to the ideal negative inductor of -60 nH, within the frequency range 1-50 MHz.

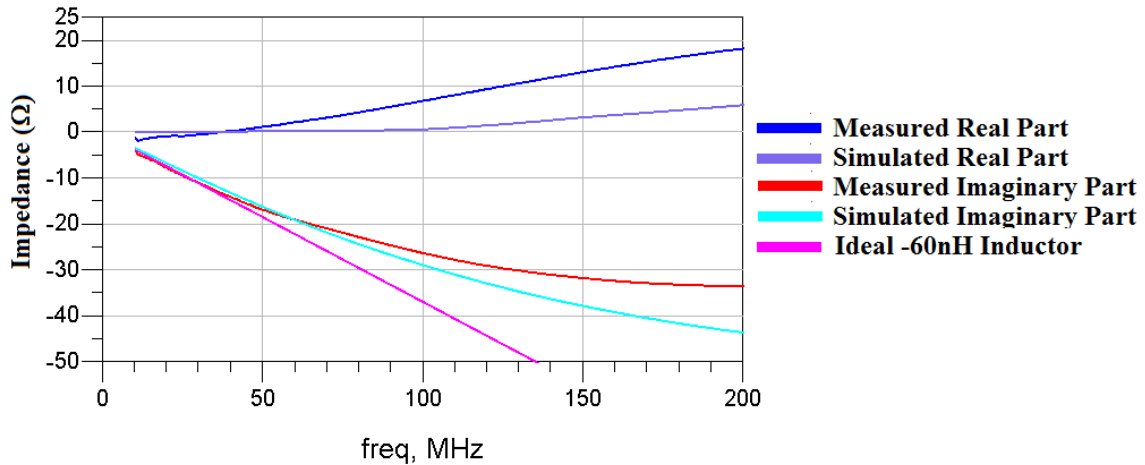


Figure 4-16 Real and imaginary part of the input impedance of the Kolev's circuit

Finally, a comparison between the simulated inductance and the inductance extracted from the measurements is shown in Figure 4-17.

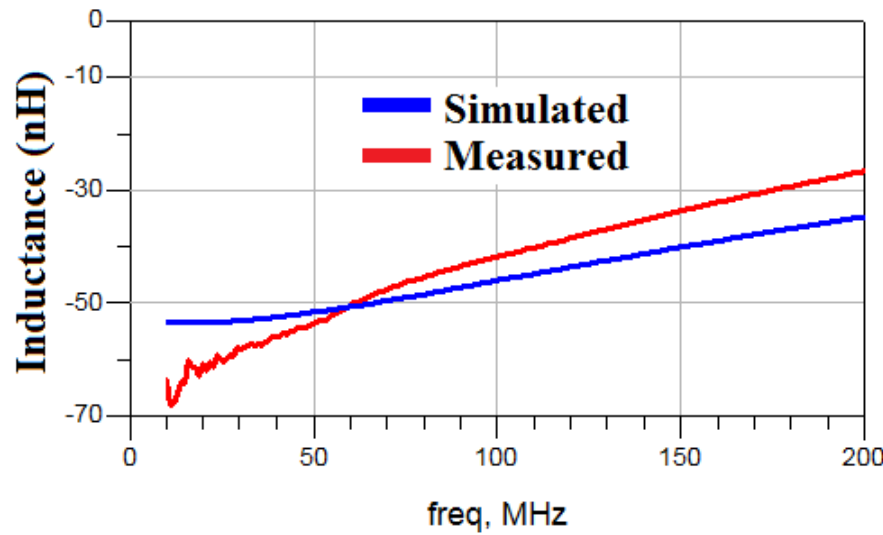


Figure 4-17 Simulated and measured equivalent inductance

As it was mentioned in the previous discussion, the circuit was not stable with a positive inductor (with inductance larger than a modulus of generated negative inductance),

connected in the series with the input. Counter-intuitively, it was only stable when a positive inductor (39nH) was placed in parallel with the circuit. In order to understand this issue, we developed the equivalent circuit of a realistic negative inductor (Figure 4-18). It was found that this circuit fits the measurement results quite well (Figure 4-19). The equivalent circuit comprises the ideal negative inductor $L_n = -50$ nH, connected in parallel with a series combination of a positive inductor $L = 7$ nH and a positive capacitor of $C = 8.5$ pF. For very low frequencies, the capacitor in Figure 4-18 presents a very high reactance, so the circuit behaves almost as an ideal negative inductor. On the other hand, for the high frequencies the capacitor behaves nearly as a short circuit. Due to this, the circuit behaves as a simple parallel combination of L_n and L . Thus, the overall inductance (at high frequencies) is positive due to the fact that $|L_n| > L$

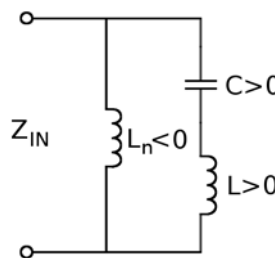


Figure 4-18 Realistic equivalent circuit of the manufactured negative inductor

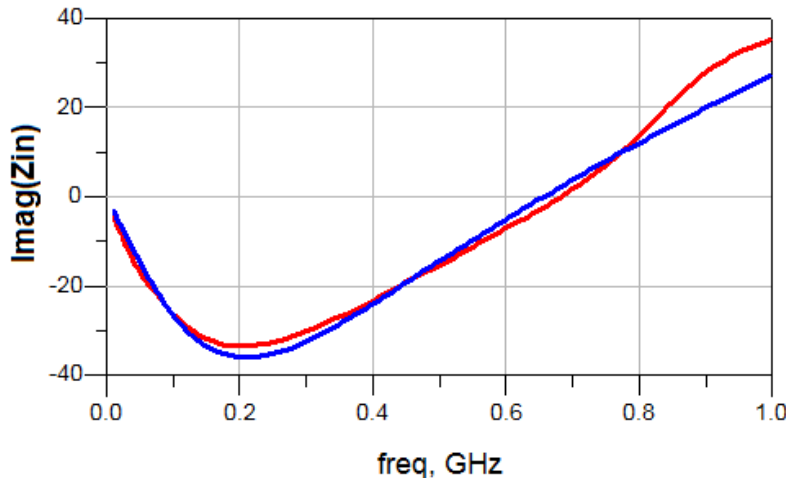


Figure 4-19 Imaginary part of the input impedance. Blue: calculation from the equivalent circuit , red: measurements

It can be seen that the agreement between the measured reactance and the reactance obtained by the equivalent circuit is rather good (Figure 4-19). Thus, it is possible to use this equivalent circuit for studying the stability of the manufactured negative inductor.

Let us first analyze the case of a realistic negative inductor connected in series with the positive inductor driven by a Norton current source (I , R) (Figure 4-20).

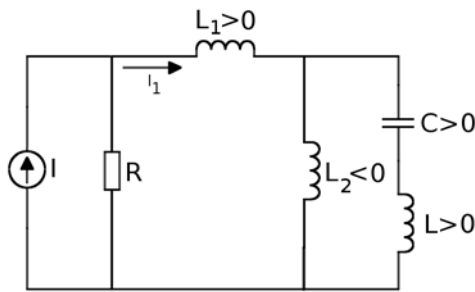


Figure 4-20 Realistic negative inductor L with a series positive inductor L_1

The unknown current I_1 can be obtained from the analysis in the Laplace domain:

$$\begin{aligned}
 I_1 &= \left(\frac{I}{s} \right) \cdot \frac{R}{R + s \cdot L_1 + \left(s \cdot L_2 // \left(\frac{1}{s \cdot C} + s \cdot L_3 \right) \right)} = \\
 &= \frac{I \cdot R + I \cdot R \cdot C \cdot (L_2 + L_3) \cdot s^2}{s^4 \cdot C \cdot (L_3 \cdot L_2 + L_1 \cdot L_2 + L_1 \cdot L_3) + s^3 \cdot R \cdot C \cdot (L_3 + L_2) + (L_3 + L_2) \cdot s^2 + R \cdot s} \quad (3.15)
 \end{aligned}$$

The circuit will be stable if $I_1(s)$ has no poles in the right-hand part of the s-plane. Figure 4-21 shows the loci of the poles of $I_1(s)$. It can be observed that there are two poles in the right-hand part of the s-plane. When the value of the positive series inductor L_1 is changed, the locations of the poles change but they are always in the right-hand part of the s-plane. Thus, this circuit is unstable, exactly as it was observed during the first measurements on the experimental prototype.

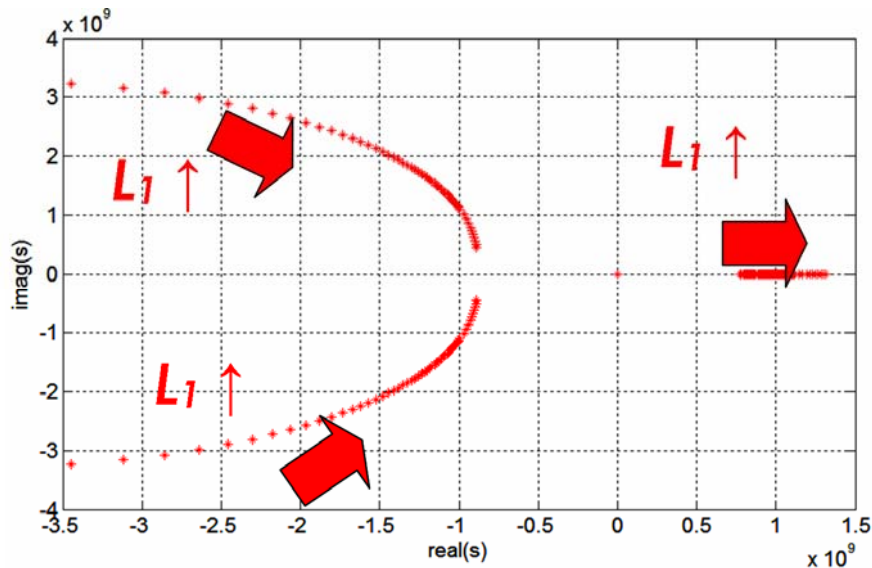


Figure 4-21 Poles of the manufactured negative inductor L_2 with a series positive inductor L_1

Now, let us analyze the case of a realistic negative inductor shunted with the positive inductor L_1 (Figure 4-22):

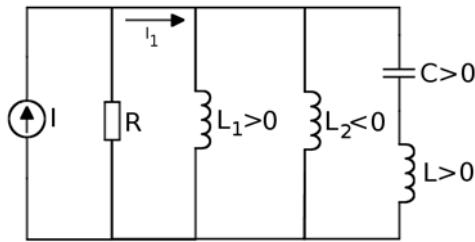


Figure 4-22 A realistic negative inductor L_2 with a parallel positive inductor L_1

The Laplace transform of the current I_1 is given by:

$$\begin{aligned}
 I_1 &= \left(\frac{I}{s}\right) \cdot \frac{R}{R + \left(s \cdot L_1 // s \cdot L_2 // \left(\frac{1}{s \cdot C} + s \cdot L_3\right)\right)} = \\
 &= \frac{I \cdot R + I \cdot R \cdot C \cdot (L_{eq} + L_3) \cdot s^2}{s^4 \cdot C \cdot (L_3 \cdot L_{eq}) + s^3 \cdot R \cdot C \cdot (L_3 + L_{eq}) + (L_{eq}) \cdot s^2 + R \cdot s} \quad (3.16)
 \end{aligned}$$

The location of the poles loci is shown in Figure 4-23. It can be seen that the poles are in the left-hand part of the s-plane if the inductance of the positive inductor L_1 is smaller than the modulus of the negative inductance L_2 (blue). However, they are located in the right-hand part of the s-plane (red), if the inductance of the positive inductor L_1 is larger than the modulus of the negative inductance L_2 . So, the circuit is stable if a positive inductor (inductance of which is smaller than a modulus of negative inductance) is connected in parallel with a realistic negative inductor. Exactly this behavior was observed during the experiments on the prototype.

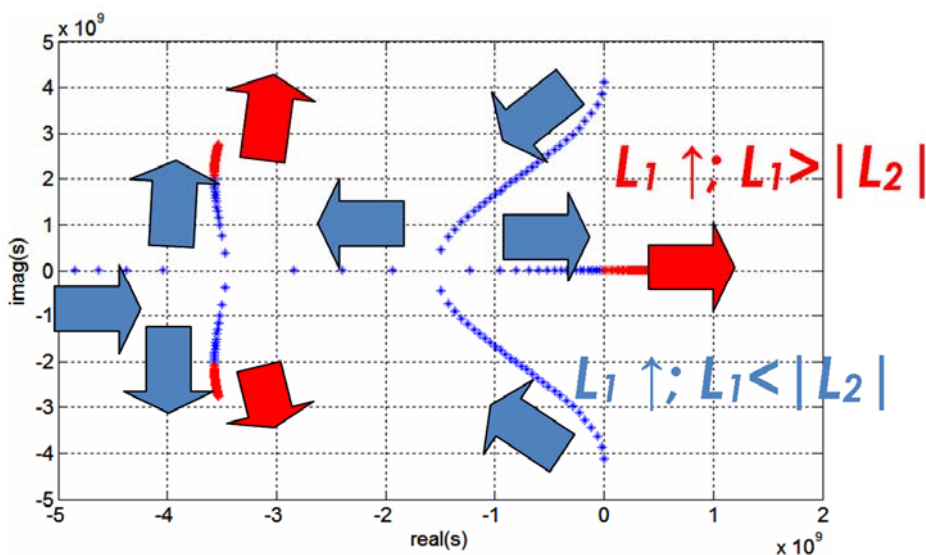


Figure 4-23 Loci of poles of a manufactured negative inductor L_2 shunted with a positive inductor L_1

As a conclusion of this stability investigation, one can state that the stability calculation of a realistic non-Foster element should take into account the dispersion behavior. This is consistent with the general discussion in Chapter 3.

4.3.2. Design based on Kolev's circuit with OPamps (1 MHz – 10 MHz)

The negative inductor developed in the previous section showed nearly ideal behavior in the lower RF range (up to 50 MHz). It is very difficult to increase this frequency using discrete FETs and ‘hand-crafting’, primarily due to the problems of construction of a stable active bias network. As mentioned several times, previously, we used high-speed OPamps for the construction of stable RF negative capacitors, operating in 2-40 MHz range ([73], Figure 3-3). It would be interesting to see if it is possible to use OPamps arranged in a way that somehow ‘imitates’ the Kolev’s circuit (Figure 4-9). This would enable building a negative inductor based on cheap OPamps.

The basic idea of a ‘replacement’ of a discrete MOSFET with a block comprising two operational amplifiers is sketched in Figure 4-24.

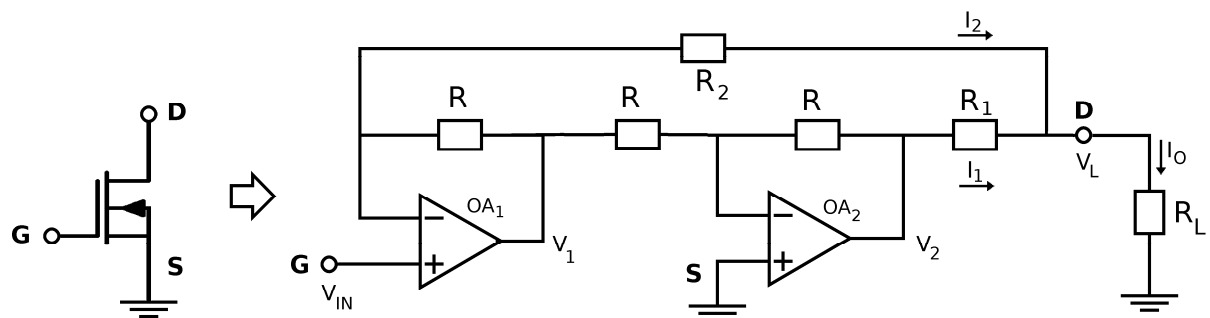


Figure 4-24 OPAMP transconductance amplifier circuit as a replacement for a MOSFET device

The current through the load I_L can be expressed by:

$$I_L = \frac{V_2 - V_L}{R_1} + \frac{V_{IN} - V_L}{R_2} I_L = \frac{V_2 - V_L}{R_1} + \frac{V_{IN} - V_L}{R_2} \quad (3.17)$$

$$\begin{aligned} V_{IN} &= -I_2 \cdot R + V_1 \longrightarrow V_{IN} = -I_2 \cdot R - V_2 \\ V_{IN} &= \frac{V_L - V_{IN}}{R_2} \cdot R - V_2 \longrightarrow V_2 = V_L \cdot \frac{R}{R_2} - V_{IN} \cdot \left(1 + \frac{R}{R_2}\right) \end{aligned} \quad (3.18)$$

Using (3.17) and (3.18), one gets:

$$I_L = V_L \cdot \left(\frac{R - R_2 - R_1}{R_2 \cdot R_1} \right) + V_{IN} \cdot \left(\frac{R_1 - R_2 - R}{R_2 \cdot R_1} \right) \quad (3.19)$$

If the condition $R=R_1+R_2$ is satisfied, the output current does not depend on the load resistance, but only on the input voltage V_{in} and R_1 and R_2 . From the relationship between the input voltage and the output current one can calculate the equivalent transconductance of an OPamp-based ‘FET replica’:

$$I_L = -\frac{2}{R_1} \cdot V_{in} \longrightarrow \frac{I_L}{V_{IN}} = g_m = -\frac{2}{R_1} \quad . \quad (3.20)$$

Figure 4-25 shows the frequency response of a transconductance amplifier with $R_2=600 \Omega$, $R_1=100 \Omega$, $R=500 \Omega \rightarrow g_m=-2/100=-20 \text{ mS}$. The red curve shows the ideal behavior (using an ideal OPamp), while the magenta and blue curves show the behavior using the AD8099 OPamp with, and without compensation, respectively. The OPamp without compensation has current peaks at high frequencies which could lead to instabilities. On the contrary, the compensated circuit presents an almost constant transconductance up to 500 MHz.

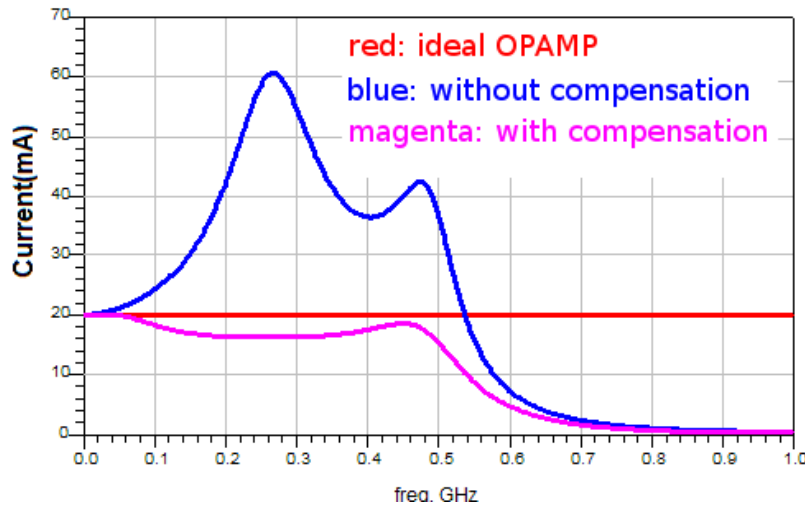


Figure 4-25 The response of the transconductance amplifier

Once the transconductance block is designed, it is possible to connect two of them together in order to obtain Kolev's topology of a negative inductor circuit.

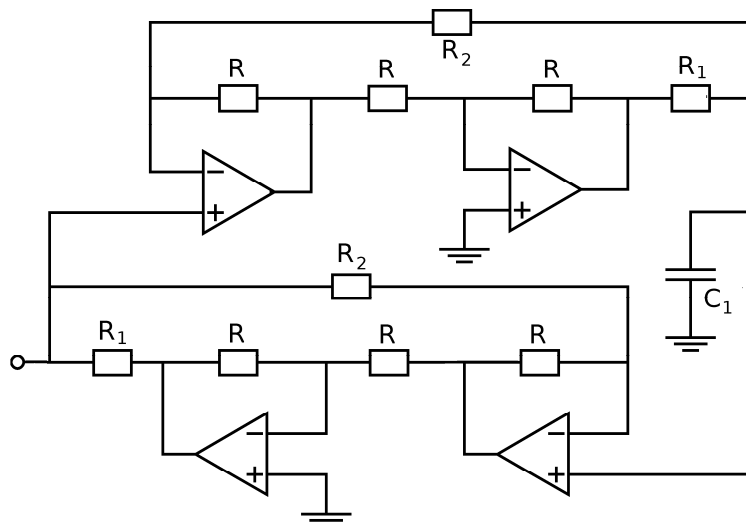


Figure 4-26 AC equivalent circuit of the designed negative inductance

In the next step, the complete design of a negative inductance circuit was performed (Figure 4-27).

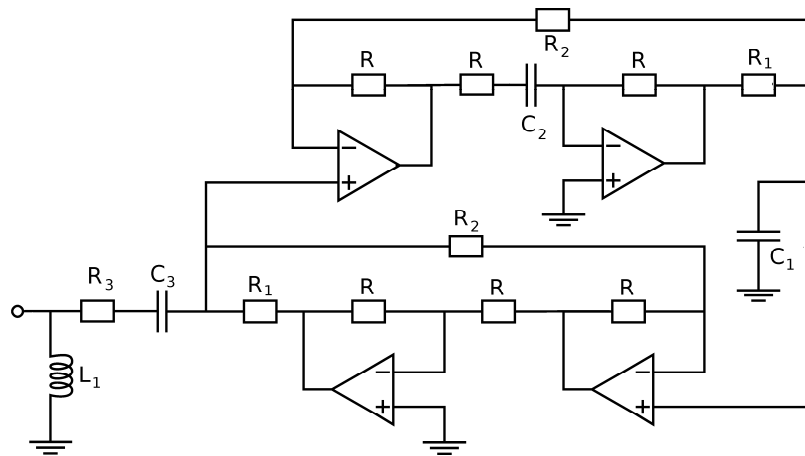


Figure 4-27 Designed negative inductance circuit based on four OPamps

The chosen resistor values were $R_2=200 \Omega$, $R_1=100 \Omega$, $R=300 \Omega$. Therefore, the transconductance of the amplifiers is set to $g_m = -20 \text{ mS}$. The input impedance and inductance are given by:

$$Z_{in} \approx \frac{-1}{g_m^2} \cdot \frac{1}{Z_L} = \frac{-1}{g_m^2} \cdot j \cdot \omega \cdot C \longrightarrow L_n = \frac{-C}{g_m^2} \quad (3.21),$$

Taking into account that $C_1=20 \text{ pF}$, the expected negative inductance is -50 nH . Capacitors C_2 and C_3 were added for DC decoupling. The purpose of the resistor R_3 (5Ω) is the (partial) compensation of the negative resistance. The inductor L_1 assures the circuit stability when connected to a 50Ω measurement system (stabilizing inductor, influence of which is removed during de-embedding procedure).

Figure 4-28, Figure 4-29, and Figure 4-30 show simulated input impedance of the negative inductance circuit (Figure 4-27), based on ideal OPAMPS and the AD8099. Using the ideal OPAMP we obtain the expected -50 nH value, while using the real AD8099 SPICE model we obtained a negative impedance about -65 nH up to 60 MHz (the imaginary part of the input impedance is linear up to 60 MHz). The losses are quite low (equivalent series resistance is lower than 10Ω within the whole operating frequency band).

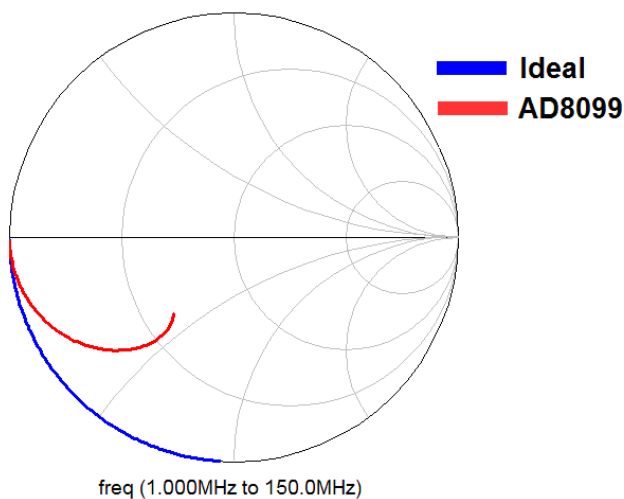


Figure 4-28 Simulated S_{11} of the negative inductance circuit based on four OPamps

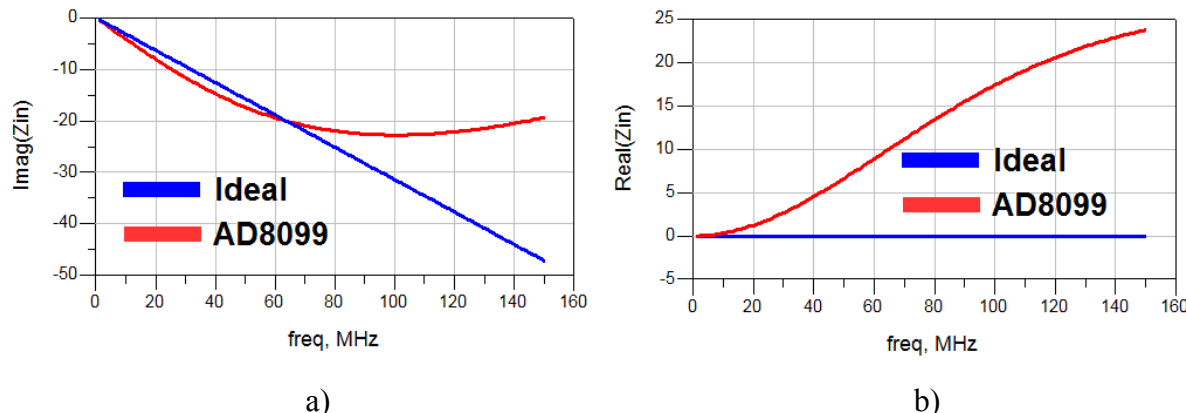


Figure 4-29 Simulated input impedance of the negative inductance circuit based on four OPamps.
a) imaginary part, b) real part

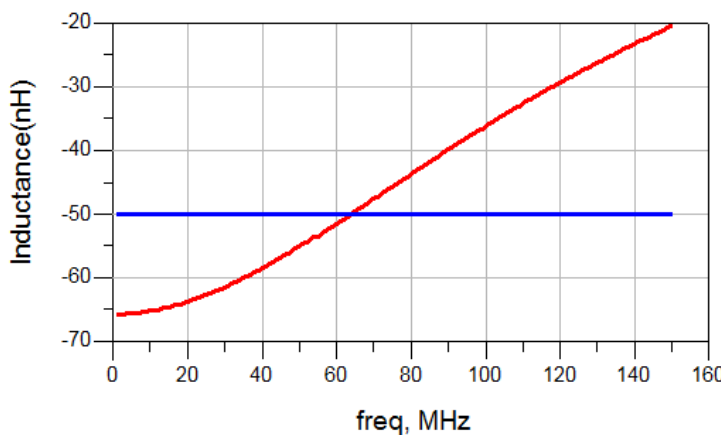


Figure 4-30 Simulated equivalent negative inductance

After the simulation, the circuit was prototyped on a low-cost FR4 substrate (Figure 4-31). Each of the operational amplifiers was placed on a small piece of the FR4 substrate with local feedback resistors connected directly to the pins of the integrated circuit. Four of such blocks were placed on a larger piece of FR4, and the interconnections were made by simple air bridges. After assembling, the input impedance was measured by an ZVL8 VNA and the obtained results are presented in Figure 4-32 and Figure 4-33. It can be seen that the obtained maximal operating frequency is only 10 MHz. It is worse than the bandwidth of the original FET-based Kolev's circuit from the previous section. Furthermore, this result is not close to the maximal frequency of 60MHz, predicted in simulation. The cause of these bad results is primarily in the parasitic inductance of the connecting air bridges. These parasitic inductances introduce significant phase shifts on the signal and feedback paths. The circuit could be improved by the placement of all elements on a single, miniaturized PCB, and even further by using multiple amplifiers on one chip/package and to use passive SMT elements. Very probably, by minimization of the lengths of the connecting tracks, it would be possible to achieve maximal operating frequency that is close to 60 MHz, predicted by the simulations. However, this was not attempted due to the inherent complexity of the circuit, which could have been a serious problem in adding tuneability/reconfigurability feature. Instead, it was decided to modify the design of an INIC OPamp based negative capacitor from section 4.2.2 into a negative inductor.

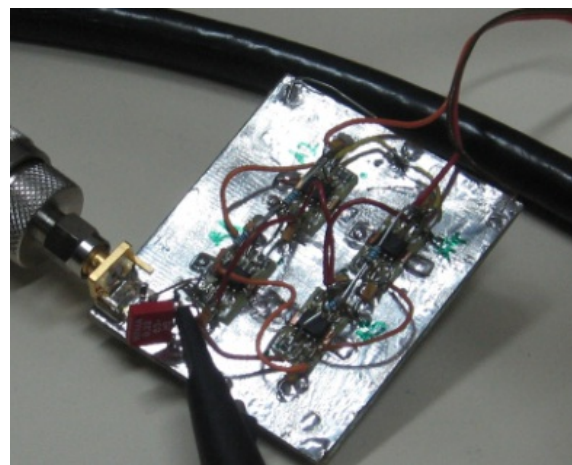


Figure 4-31 The prototype of the negative inductance circuit based on four OPamps

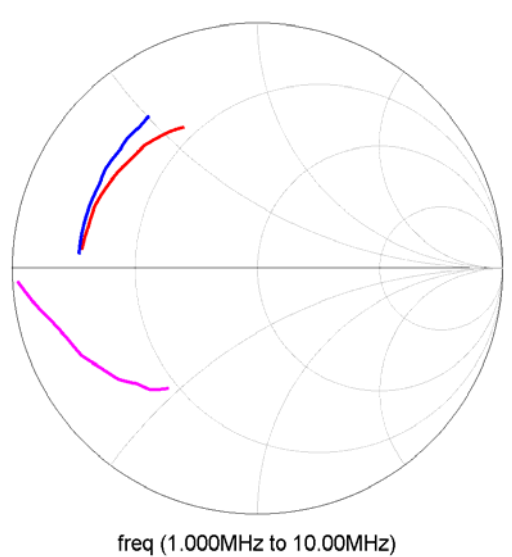


Figure 4-32 Measured S11 of the negative inductance circuit based on four OPamps. Blue: circuit power off, red: circuit power on, magenta: de-embedded S11, circuit power on)

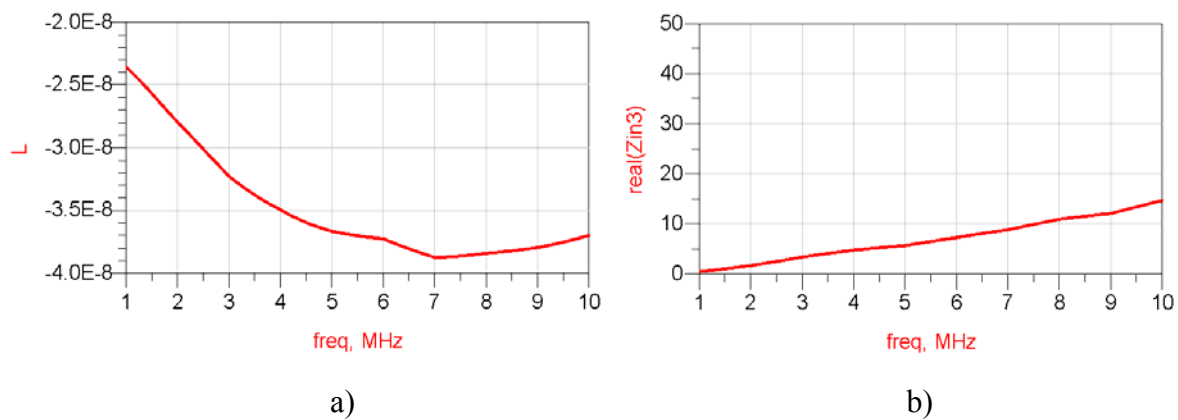


Figure 4-33 De-embedded inductance and resistance of the negative inductance circuit based on four OPamps. a) inductance, b) resistance

4.3.3. Design based on an Opamp (100 kHz - 700 MHz)

At first sight, turning the THS4303-based negative capacitor from section 4.2.2. into a negative inductor looks rather straightforward. The only modification needed is the replacement of a capacitor in the feedback loop with an inductor. However, it is clear that an inductor in the feedback loop must be DC decoupled (otherwise, the circuit will be unstable at low frequencies for which the inductor reactance approaches zero). It is also clear that the capacitance of the decoupling capacitor directly influences the lowest operating frequency. Therefore, one should select a high quality DC decoupling capacitor. The second problem comes from the ‘swamping’ stabilizing inductor that should shunt the input of the circuit. It might happen that the resonance of this inductor with the OPamp input capacitance falls into the operating frequency range. Finally, there is a previously explained problem of the parasitic inductances of the tracks. Of course, these are pure technological problems but they can decrease the operating bandwidth. We used the approach similar to that from the section 4.2.2. All the parasitic effects were approximated using quasi-static equations from the literature and predicted values are used in the SPICE-based simulations. After that, several optimization cycles of the PCB layout were performed. The final circuit diagram (with parasitic effects included) and a photograph of the fabricated prototype are shown in Figure 4-34 and Figure 4-35, respectively.

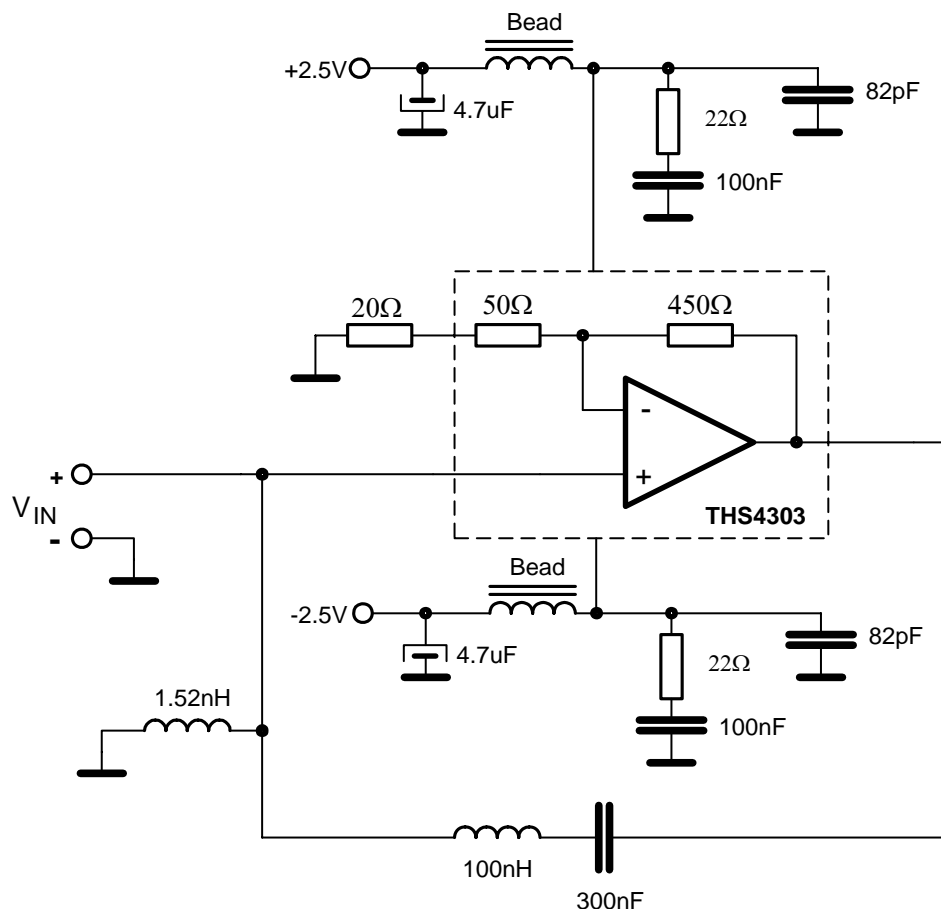


Figure 4-34 Circuit diagram of the design of the negative inductance demonstrator (100 kHz – 700 MHz)

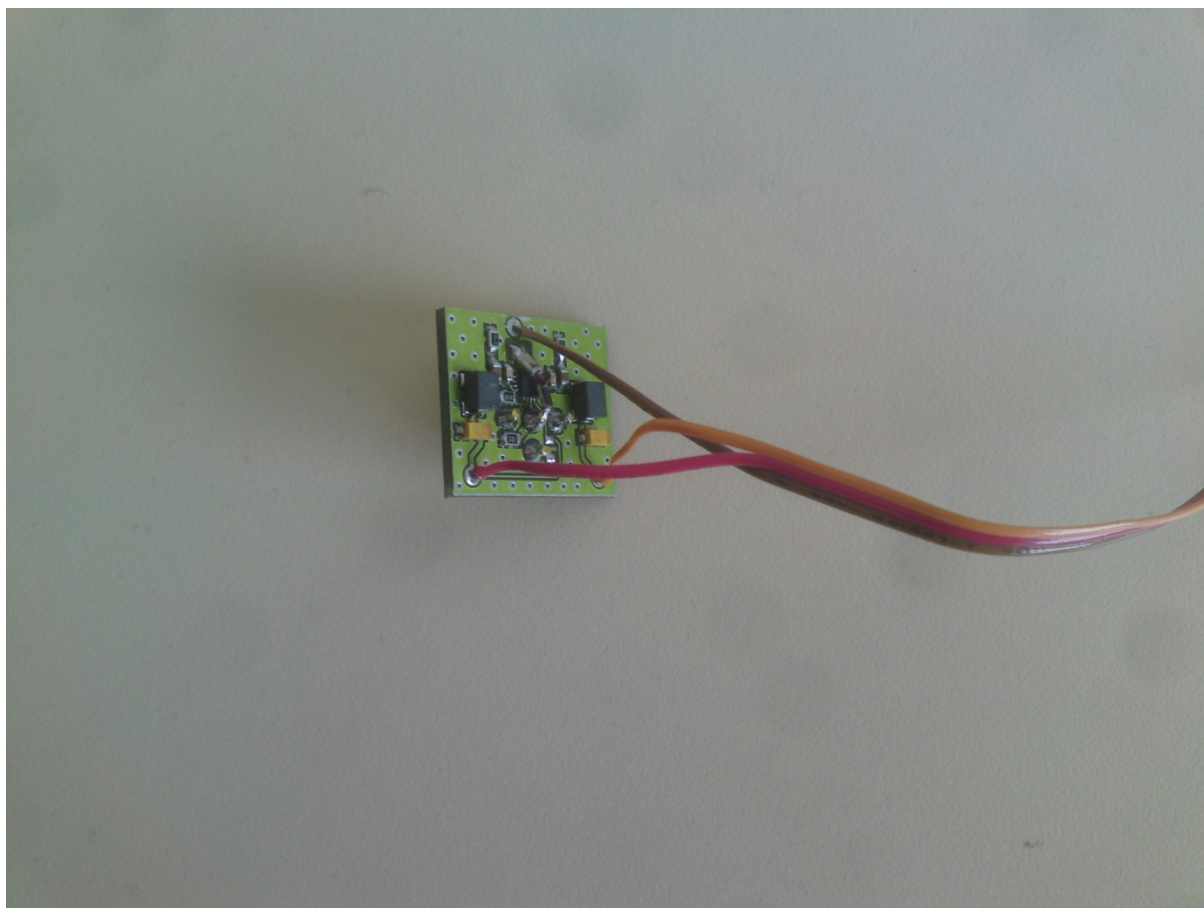


Figure 4-35 Photograph of the design of the negative inductance demonstrator (100 kHz – 700 MHz)

After the assembling, the input reflection coefficient was measured using an ZVL8 VNA. Input inductance and shunt conductance, de-embedded form the results of the measurements are shown in Figure 4-36 . It can be seen that the measured value follows the prediction form the simulations rather well, up to the frequency of 600 MHz. Above that frequency, the negative inductance becomes dispersive, but this dispersion is still acceptable up to the frequency of 700 MHz. Similarly to the case of a negative capacitor, it was found that the inductance of an SMA inner pin seriously affects the results. Again, additional simulations showed that a structure that would use a negative inductor without the connector should have a maximal operating frequency above 700 MHz with almost dispersionless behavior ($\pm 15\%$). As it was mentioned in the case of a negative capacitor, we believe that it is very difficult to achieve better results without the use of microelectronic technology.

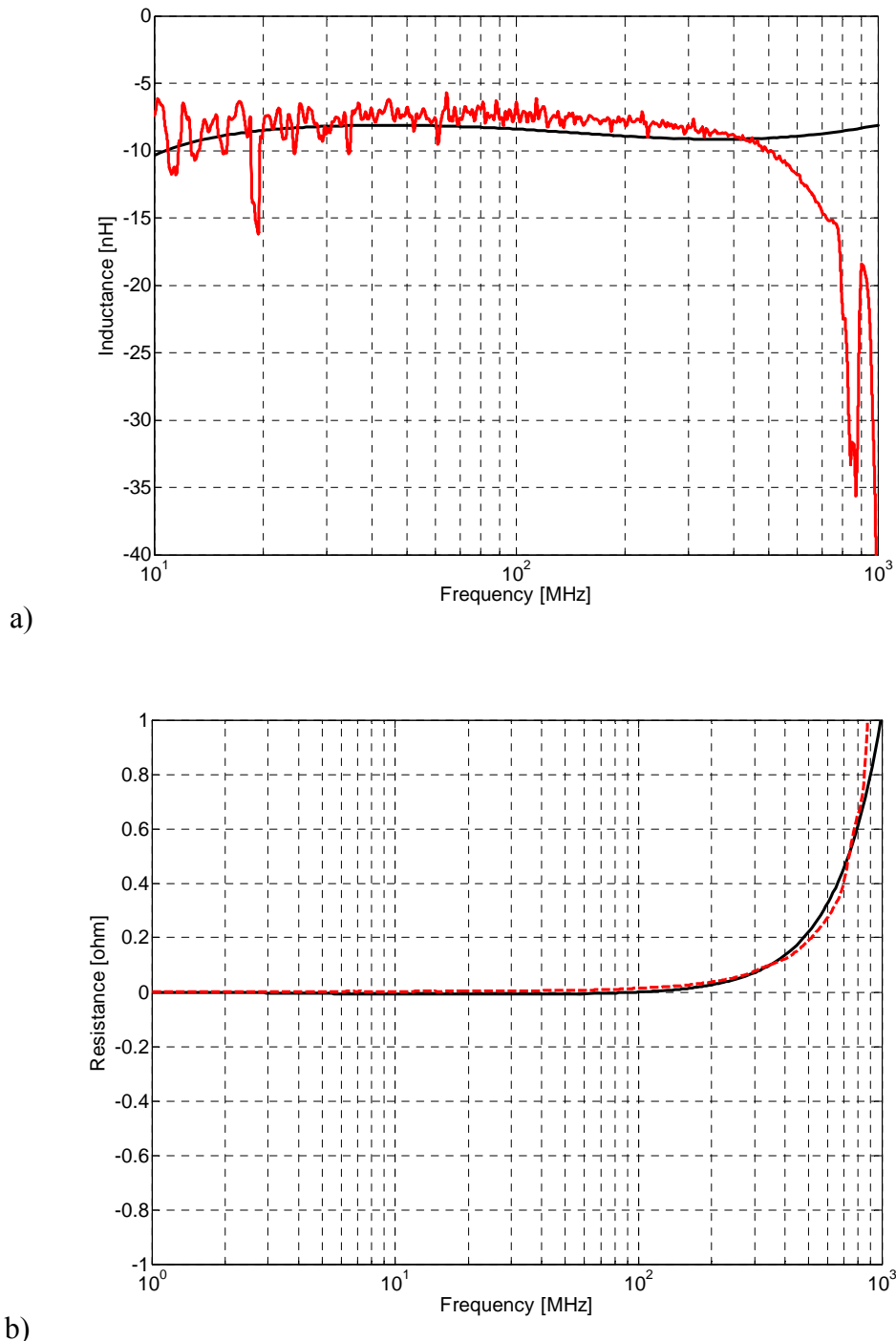


Figure 4-36 Measurements of the design of the negative inductance demonstrator a) generated inductance (solid black – simulations, dashed red - measurements) (measured with the help of an ZVL 8 VNA) b) generated resistance (solid black – simulations, dashed red - measurements) (measured with the help of an ZVL 8 VNA)

4.3.4. The MNZ unit cell

Similarly to the approach in the section 4.2.3. the developed negative inductor was used as a part of a simple experimental 1D MNZ unit cell (Figure 1-5). Extraction of the measured parameters shows that it was possible to obtain an equivalent relative permeability of $0.4 \pm 15\%$ in the frequency band 100 kHz-700 MHz.

4.4. Adding tuneability/reconfigurability feature

In the section 4.3 it was shown possible to build a stable negative capacitor and a negative inductor demonstrators that operate in the frequency band 100 kHz-700 MHz. The demonstrators have been built using cheap, commercially available, ultra-high-speed OPamps that are very convenient for ‘hand-crafting’. Here, we report the efforts towards adding a tuneability feature to the previously developed prototypes. This would enable dynamic control of the effective permittivity and/or effective permeability of the associated ENZ/MNZ metamaterial unit cell. The final goal would be a reconfigurable unit cell that could be simply in-situ ‘programmed’ to have tunable ENG and/or MNG properties. One of the possible applications of this approach could be in cloaking technology [12-14,66,115] that requires many unit cells with different (previously predetermined) ENZ or MNZ behavior.

4.4.1. Basic ideas

There are several simple ways of tuning the generated negative capacitance in the prototypes developed in the section 4.2. The simplest (and cheapest) solution is using varactor diodes that have been used in RF and microwave engineering for many decades. Simply stated, a varactor diode behaves as a capacitor, the capacitance of which can be tuned by the applied reversely polarized bias voltage.

For instance, one might think of a simple replacement of the inverting capacitor in the positive feedback loop of INIC-based negative capacitor with a varactor diode (Figure 4-37). Here, C_o is the inverting capacitor and C_p is the stabilizing capacitor.

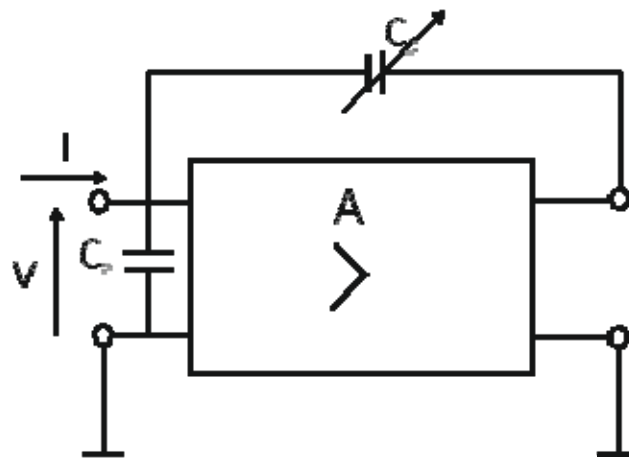


Figure 4-37 Tuning of the negative capacitance: Method I

A Good property of this approach is the linear tuning characteristic that, at least in theory, obtains simple adjustments of the desired value of the equivalent relative permittivity between 0 and 1 (Figure 4-38).

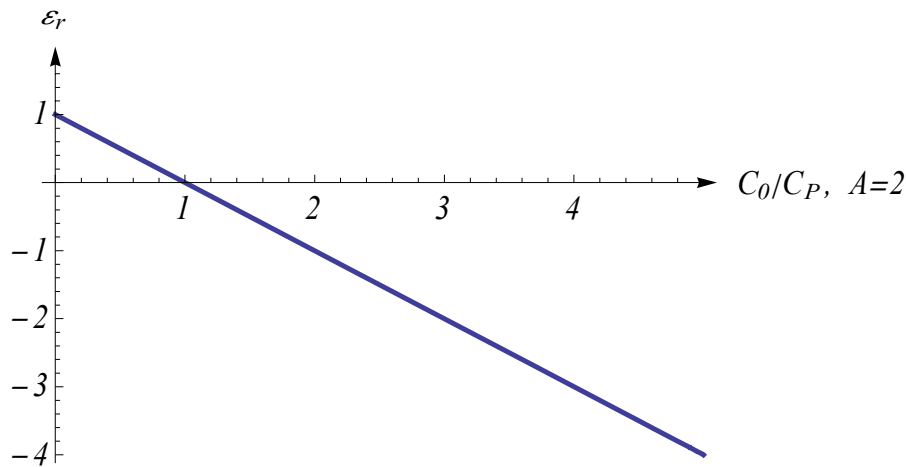


Figure 4-38 Achieved range of the equivalent permittivity: Method I

Of course there are some drawbacks of this approach, as well. At first, it is rather difficult to construct a broadband biasing network (that should be DC decoupled from the amplifier). Secondly, a lot of ultra-fast broadband OPamp are very sensitive to the change of the capacitance in the positive feedback loop. Thus, the tuning of the feedback capacitor might affect the properties of the OPamp and lead to stability problems (this instability is of the OPamp itself, not the insatiability of the negative capacitor as the circuit element).

Another possible way of tuning might be to use a varactor diode as the ‘swamping’ stabilizing capacitor (Figure 4-39). The advantage of this approach lies in the fact that one terminal of the varactor is grounded, which significantly simplifies the construction of the biasing network. The drawback is a non-linear tuning curve (Figure 4-40) that follows the Drude dispersion model.

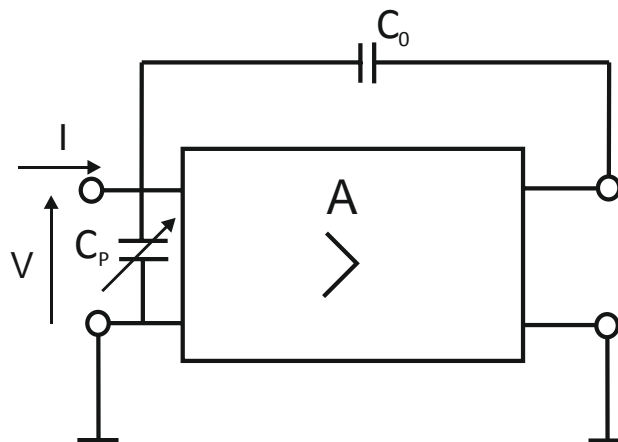


Figure 4-39 Tuning of the negative capacitance: Method II

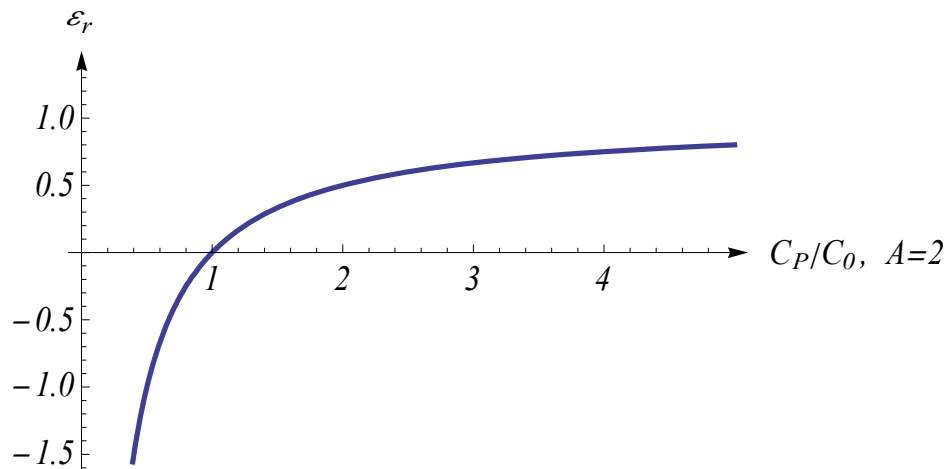


Figure 4-40 Achieved range of the equivalent permittivity: Method II

Yet another possibility is to change the amplifier gain (Figure 4-41). This approach is technologically difficult since there are almost no OPamps with variable gain available in the market. There are several types of so-called gain blocks with this feature, but they are not convenient for the use in non-Foster applications due to a 50 ohm input impedance. One might think of adding a PIN diode to the negative feedback loop. Since the PIN diode behaves (within some range of DC bias voltages) as a resistor, it is possible to use it for the tuning of the gain. Of course, this method is widely used in automatic gain control of commercial communication receivers. From the negative capacitor application point of view, the drawback of this approach is in a complicated bias network. In addition, the tuning curve is non-linear and it follows a Lorentz dispersion model (Figure 4-42).

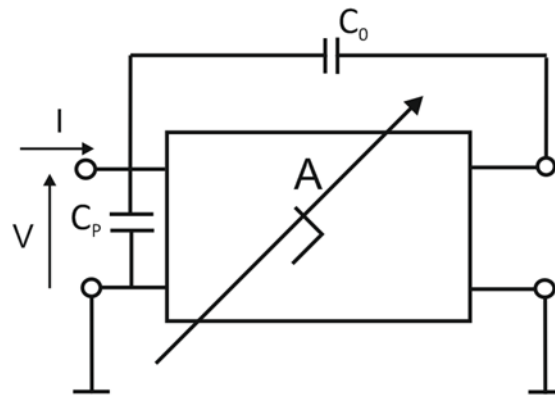


Figure 4-41 Tuning of the negative capacitance: Method III

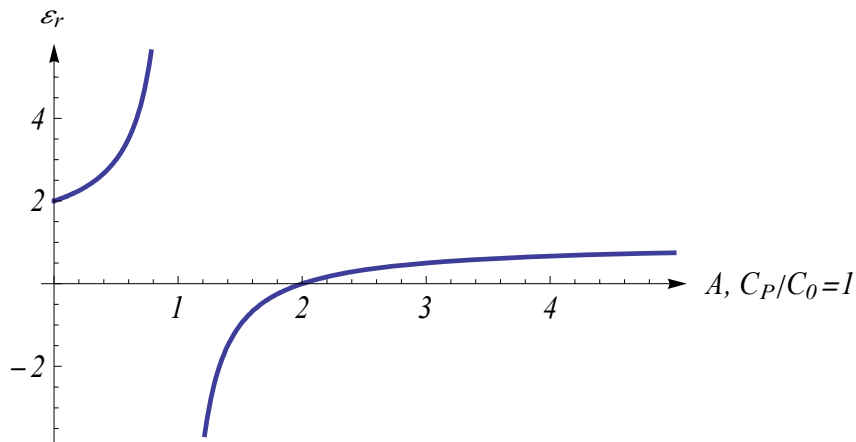


Figure 4-42 Achieved range of the equivalent permittivity: Method III

Let us now analyze the possibility of adding tuning to the INIC-based negative inductors. Since there are no variable inductors that can be adjusted by DC signals, it appears that only (simple) solution is the gain tuning (Figure 4-43). The circuit is almost equal to that proposed in the negative capacitor case (Figure 4-41, L_0 is the inverting inductor with DC decoupling capacitor, C_c and L_p are the stabilizing capacitor and inductor, respectively). As in the previous case, the gain tuning is achieved by changing the bias of the PIN diode). A nice property of this method is a linear tuning curve of the equivalent permeability.

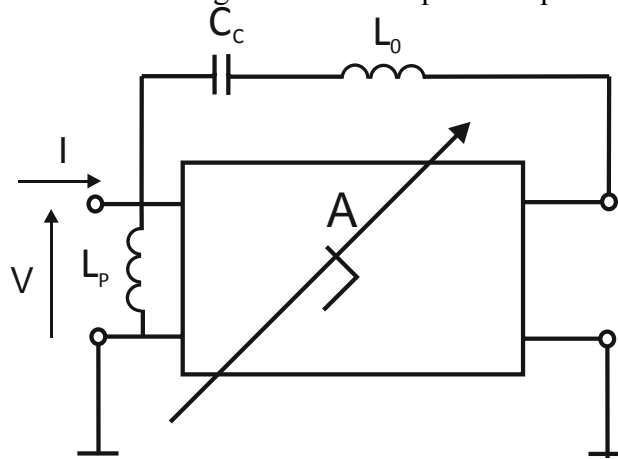


Figure 4-43 Tuning of the negative inductance

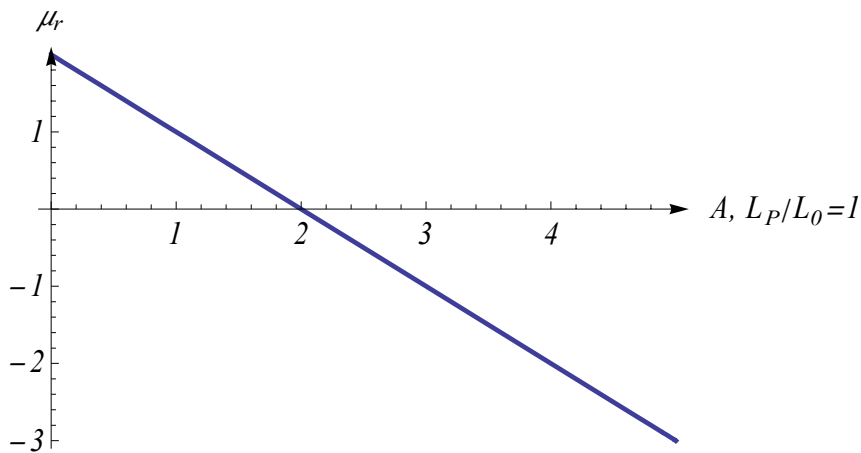


Figure 4-44 Achieved range of the equivalent permeability

4.4.2. OP-amp-based tunable negative capacitor (1 MHz- 40 MHz)

In our previous project, an RF negative capacitor (and associated ENZ metamaterial), operating in 2MHz-40MHz band, was successfully developed and tested [73]. We decided to use that prototype for testing the idea of tuneability by adding a varactor. The negative capacitor (Figure 3-3 a)) was based on the AD8099 OPamp that is sensitive to the change of the capacitance in the positive feedback loop. Thus, the Method II (Figure 4-39) was chosen for the implementation of tuning. In our previous report [73] we developed a prototype of a grounded negative capacitive impedance converter that has been successfully simulated and fabricated. It is a circuit that converts a capacitive impedance from a positive to a negative value. The actual electronic version of the converter is depicted in Figure 4-45.

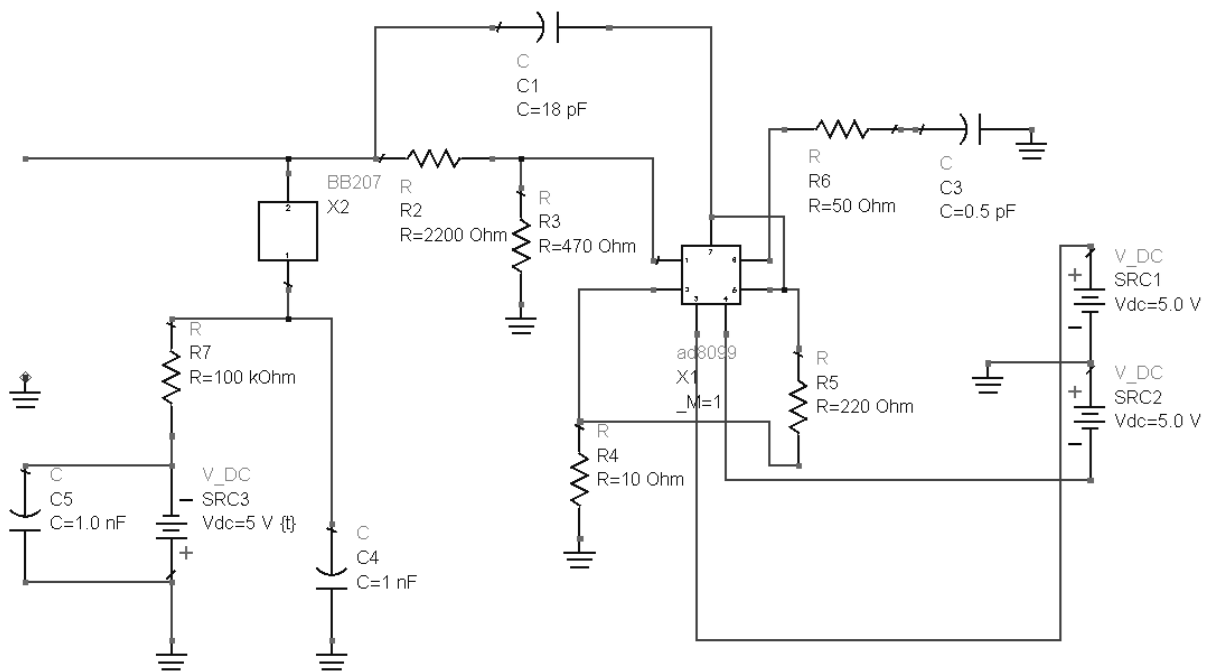


Figure 4-45 Circuit diagram of the AD8099 based tunable negative capacitor

BB207 silicon Varactor diode was chosen for tuning. One of the advantages of the Method II (Figure 4-39) is in a very simple DC bias network. The varactor with a series resistor R_7 (and AC shunting capacitor C_4) was simply connected in shunt across the input port of the negative capacitor. The additional stabilizing capacitor of 56 pF (not shown in Figure 4-45) was connected in shunt to the input terminals of the negative capacitor. In the first step, ADS simulation (with SPICE-based models of both the AD8099 OPamp and BB207 varactor) was performed. A sample of the obtained results is shown in Figure 4-46. It depicts the generated input capacitance as a function of the tuning DC voltage.

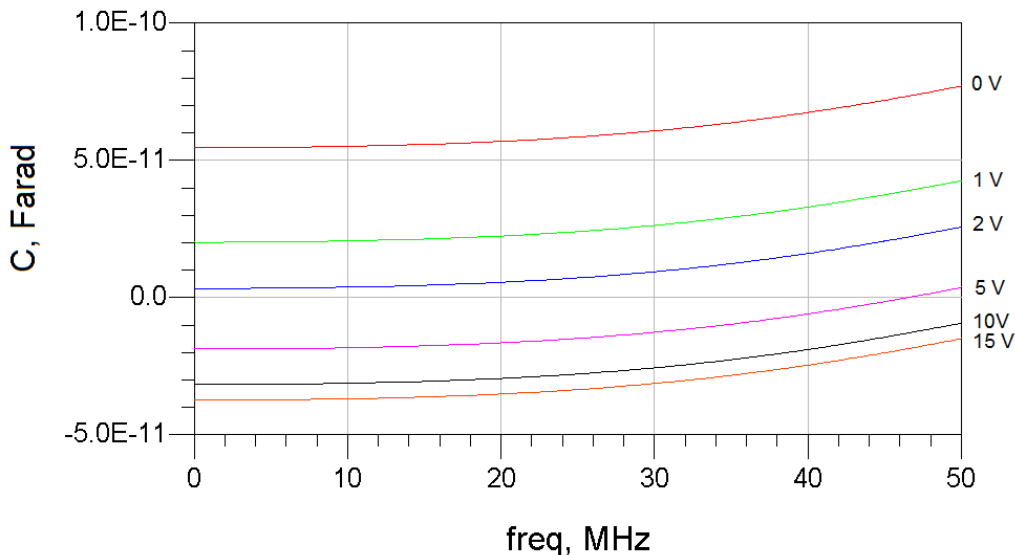


Figure 4-46 Simulated input capacitance of the AD8099 based tunable negative capacitor

It can be seen that it is possible to achieve both positive and negative values of the input capacitance (from + 55pF to -42pF, for the bias voltage 0-10 V, at the frequency of 2 MHz). Possible application of this property may be in a DPS-ENZ unit cell. Another good feature is a weak dispersion of the generated capacitance ($\pm 15\%$ across the range 2-40 MHz). After the simulations, the varactor with the associated DC bias circuit was added to the negative capacitor prototype developed in [73] and the input reflection coefficient was measured with the help of an ZVL8 VNA. The results are shown in Figure 4-47. It shows the net capacitance (input capacitance of the circuit together with the capacitance of the stabilizing capacitor of 56 pF). It can be seen that the generated negative capacitance agrees with the simulation results (Figure 4-46) quite well. The value of the generated negative capacitance (calculated by simple subtraction of the capacitance of stabilizing capacitor) ranged from +54pF to -46 pF, at the frequency of 2 MHz, for the bias voltage 0-10 V.

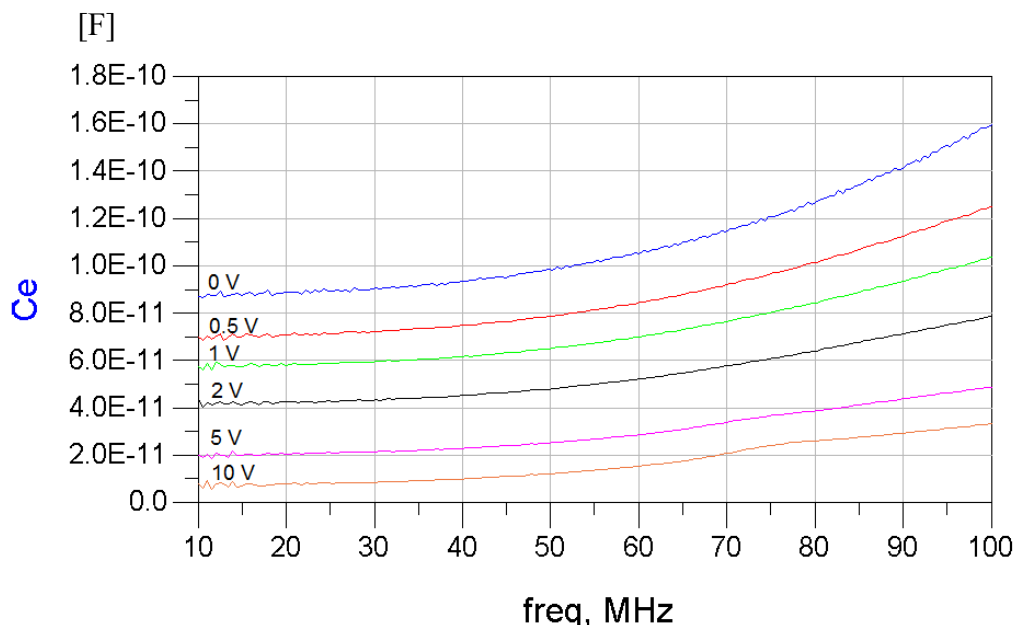


Figure 4-47 Measured net capacitance of the AD8099 based tunable negative capacitor

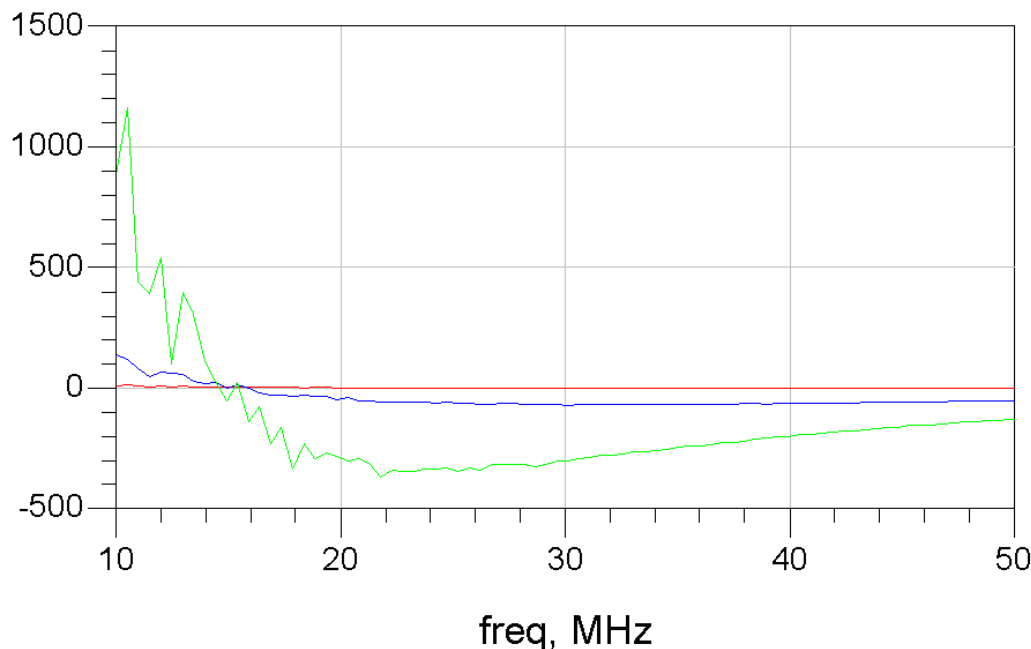
[Ω]

Figure 4-48 Measured input resistance of the AD8099 based tunable negative capacitor (the DC bias is varied, red: 0V, blue: 5V, green: 10V)

Finally, the influence of the DC bias on the losses was investigated. It was done by the extraction of the input resistance from the measured input reflection coefficient (Figure 4-48). It can be seen that the losses depend on the DC bias and that they are not negligible. Equivalent input resistance changes from $+30\ \Omega$ to -50Ω for a 5V DC bias. For a 10 V DC bias, the equivalent input resistance changes from $+1000\ \Omega$ to -39Ω . This bad result is the consequence of the attenuator (R_2 , R_3 in Figure 4-45) that was used due to the inherent instability of the AD8099 OPamp for the gain values lower than 5 [73]. It was envisaged that this loss/gain might be substantially lower if one would use the topology without the attenuator (for instance, the topology of the negative capacitor based on a THS4303 amplifier (Figure 4-4). Therefore, in the next section we report our efforts towards adding the tuneability to the THS4303-based negative capacitor.

4.4.3. OP-amp-based tunable negative capacitor (100 kHz- 700 MHz)

This tunable negative capacitor was designed as a simple upgrade of the THS4303 OPamp-based negative capacitor detailed in the section 4.2.2. (Figure 4-4). BBY53-02 high Q hyperabrupt varactor diode was chosen for tuning. A simple DC bias network with BBY53-02 varactor was added to the circuit from Figure 4-4 (again using Method II from Figure 4-39). The circuit diagram of the designed tunable negative capacitor (with parasitic effects included), used in ADS simulations, is shown in Figure 4-49. It can be seen that the values of the elements in the positive feedback loop were changed, comparing to the previous case (Figure 4-4). This was done in order to achieve better tuning linearity and minimize the

dispersion. The results of simulations (for different DC bias voltages) are shown in Figure 4-50, Figure 4-51, Figure 4-52, Figure 4-54, and Figure 4-55.

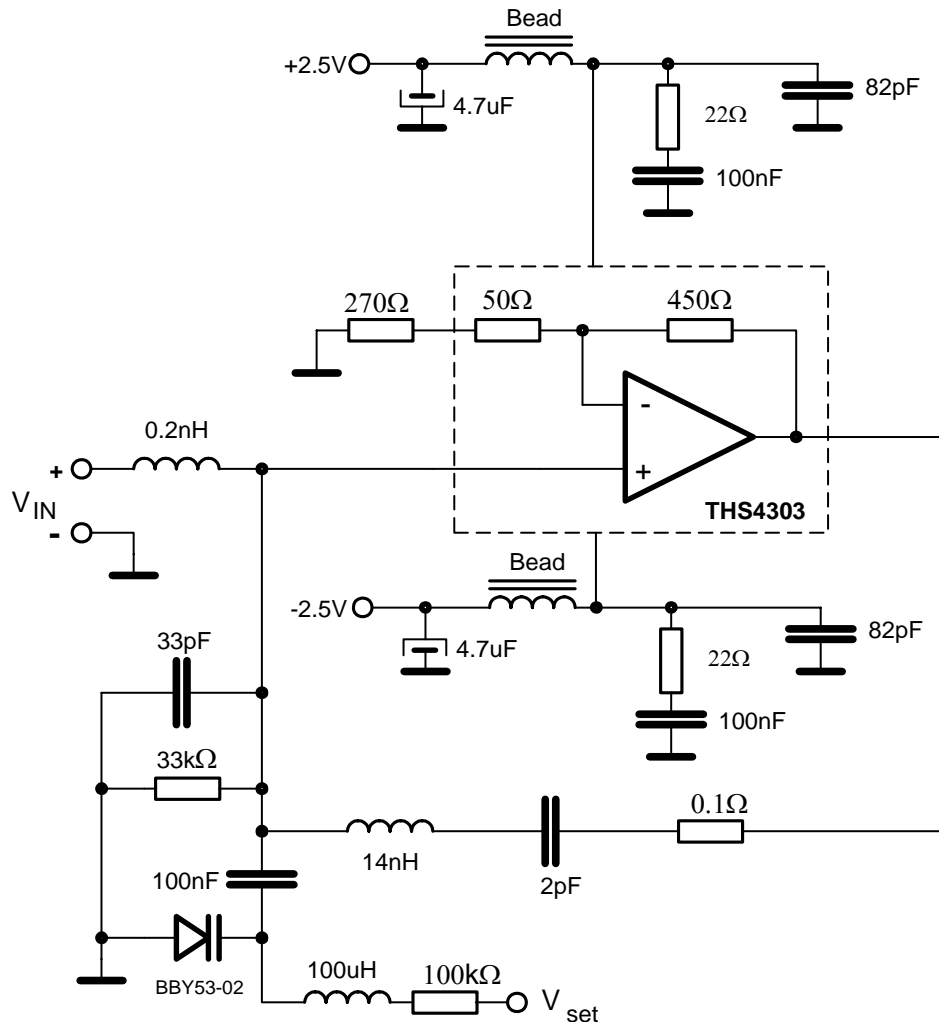


Figure 4-49 Circuit diagram of the tunable negative capacitor (100 kHz – 700 MHz) with parasitic effects included

It can be noted that the generated negative capacitance can be tuned from -2 pF to almost 0 pF, for the DC bias voltages in the range 2-10 V, within the frequency range 100 kHz – 700 MHz. It is important to stress that the losses are indeed negligible (equivalent conductance was smaller than 0.1 mS). Unfortunately, we were not able to test this circuit in practice because the required varactors (BBY53-02) were (at that time) not available in the market. Therefore, we tested the circuit using the MA 45228-30 varactor diode (which was used previously in some other project in our group). The measurement results showed the equivalent capacitance in the range 1.1 pF to -0.8 pF across the range of 300 MHz-700 MHz. It was not possible to observe any tuning capability below for the frequencies below 300MHz. These bad results are solely caused by the properties of the used varactor that is not suitable for this purpose. One should be aware that the SPICE model of the BBY53-02 varactor, obtained from the manufacturer, and the operation of the negative capacitor circuit itself, was successfully verified experimentally in the section 4.2.2. Therefore, we strongly believe that, with the use of the proposed varacor, it is possible to obtain tuneability in the range 100 kHz

– 700 MHz. It will be attempted in the future, providing that the required varactor is available.

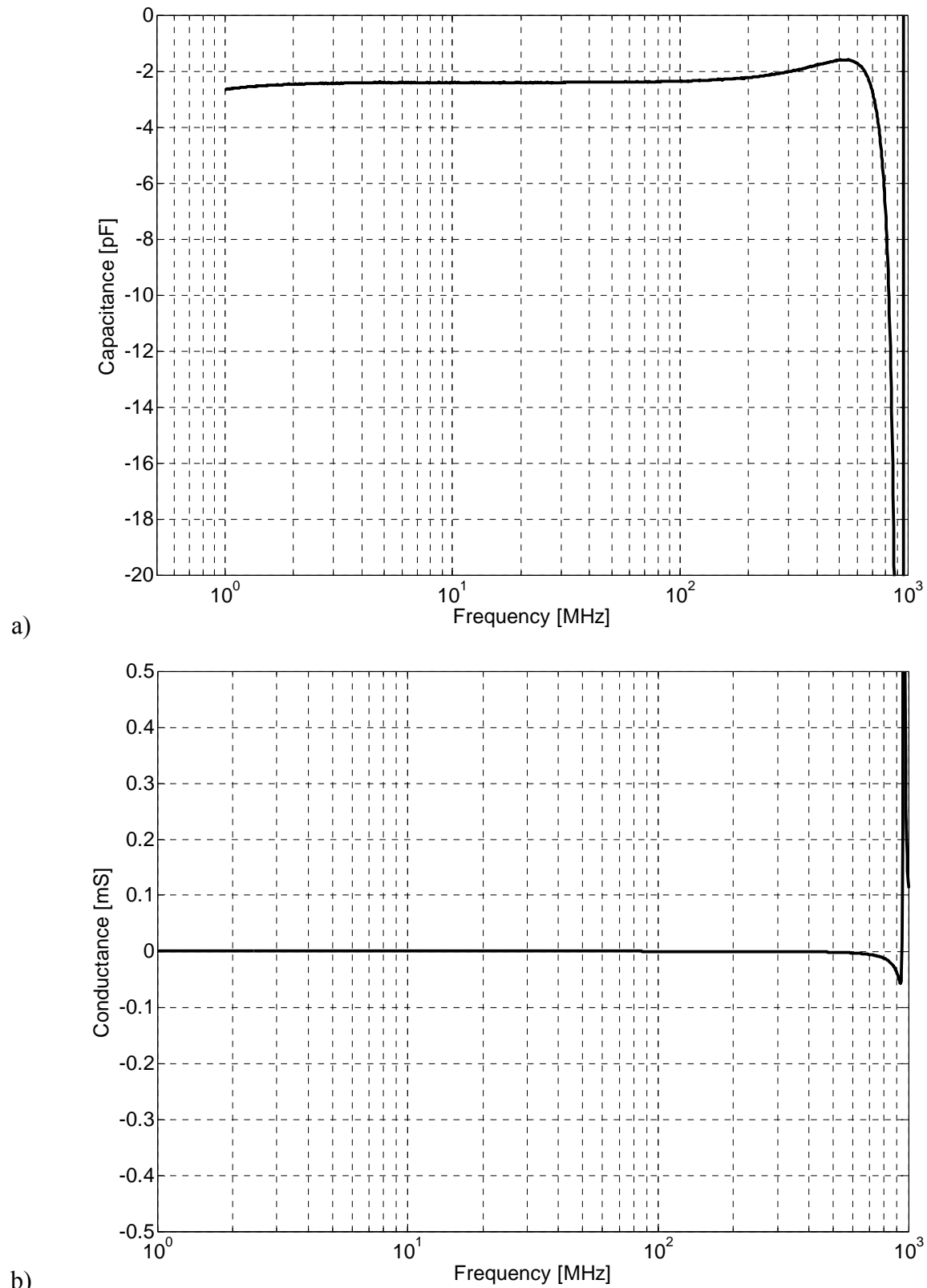


Figure 4-50 Simulations of the tunable negative capacitor ($V_{BIAS} = 10$ V)
 a) generated capacitance b) generated conductance

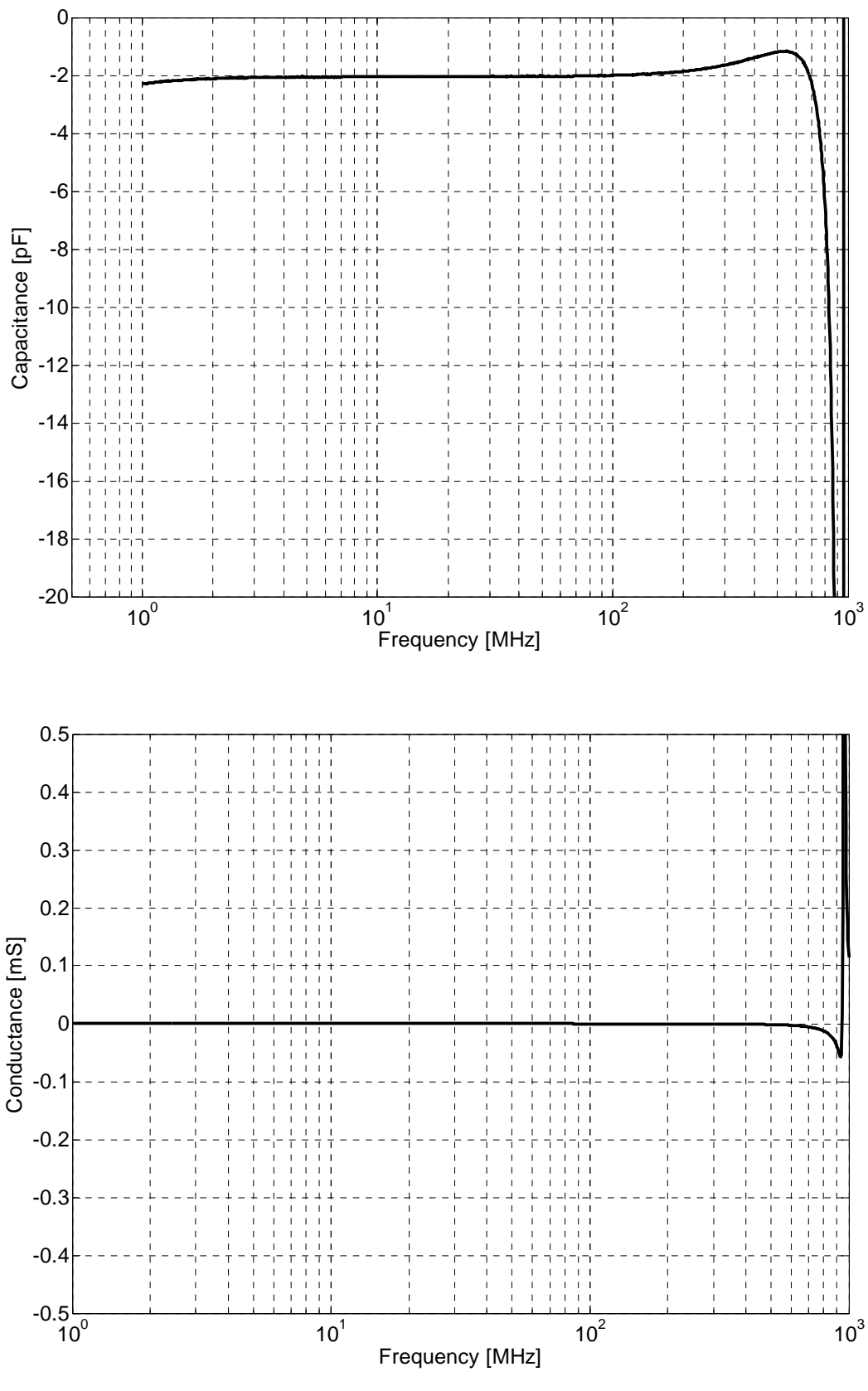


Figure 4-51 Simulations of the tunable negative capacitor ($V_{BIAS} = 7$ V)
a) generated capacitance b) generated conductance

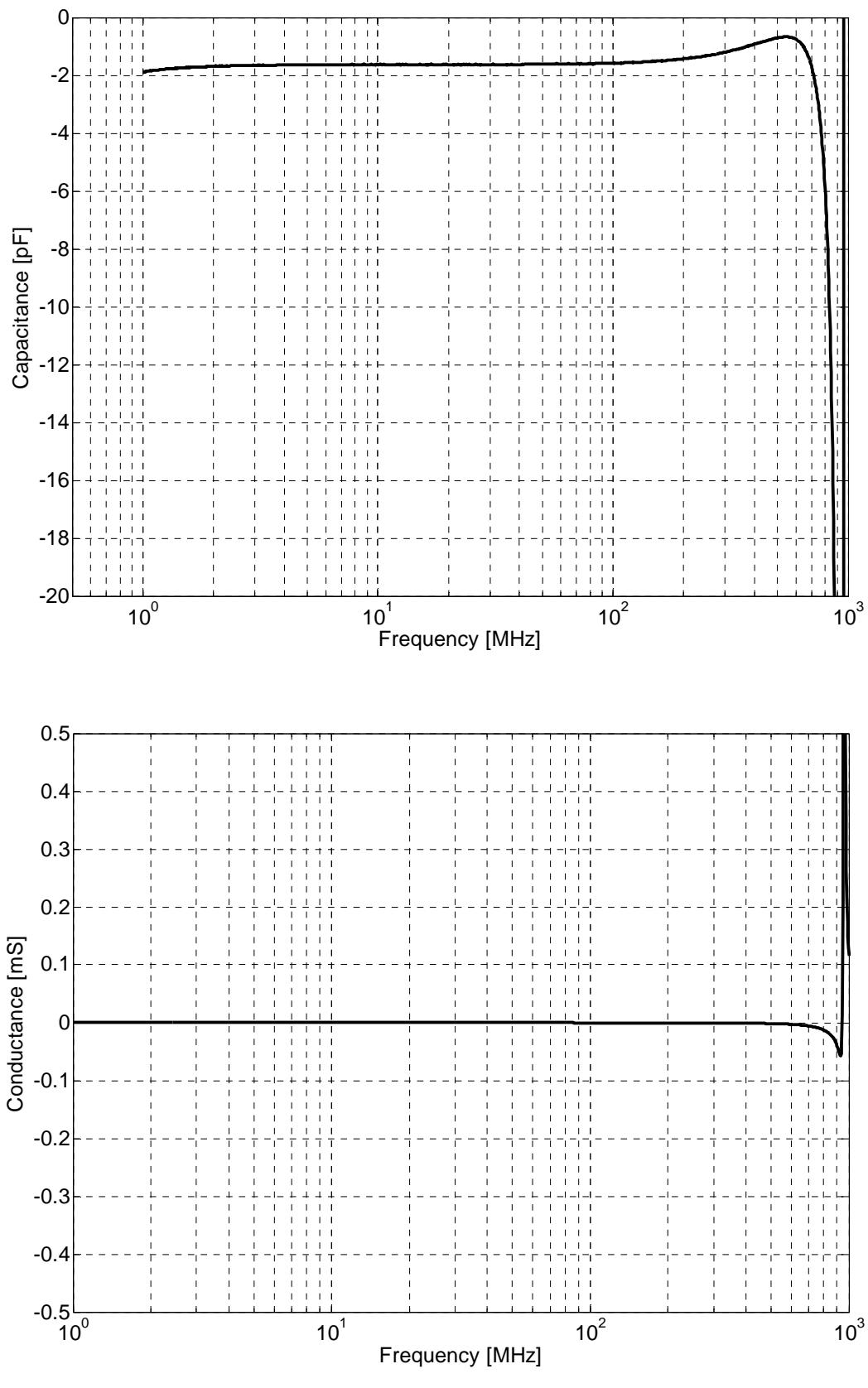


Figure 4-52 Simulations of the tunable negative capacitor ($V_{BIAS} = 5$ V)
a) generated capacitance b) generated conductance

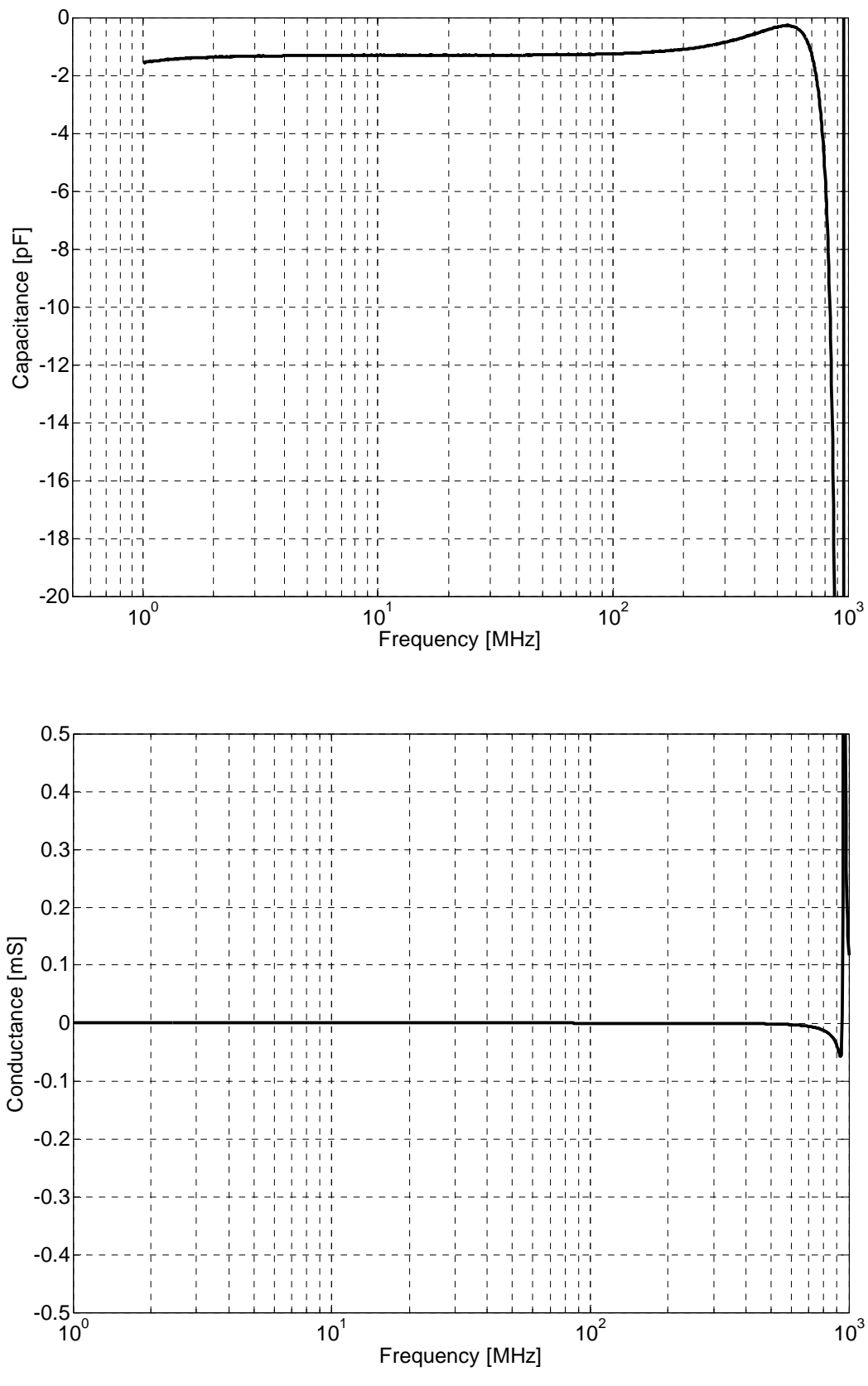
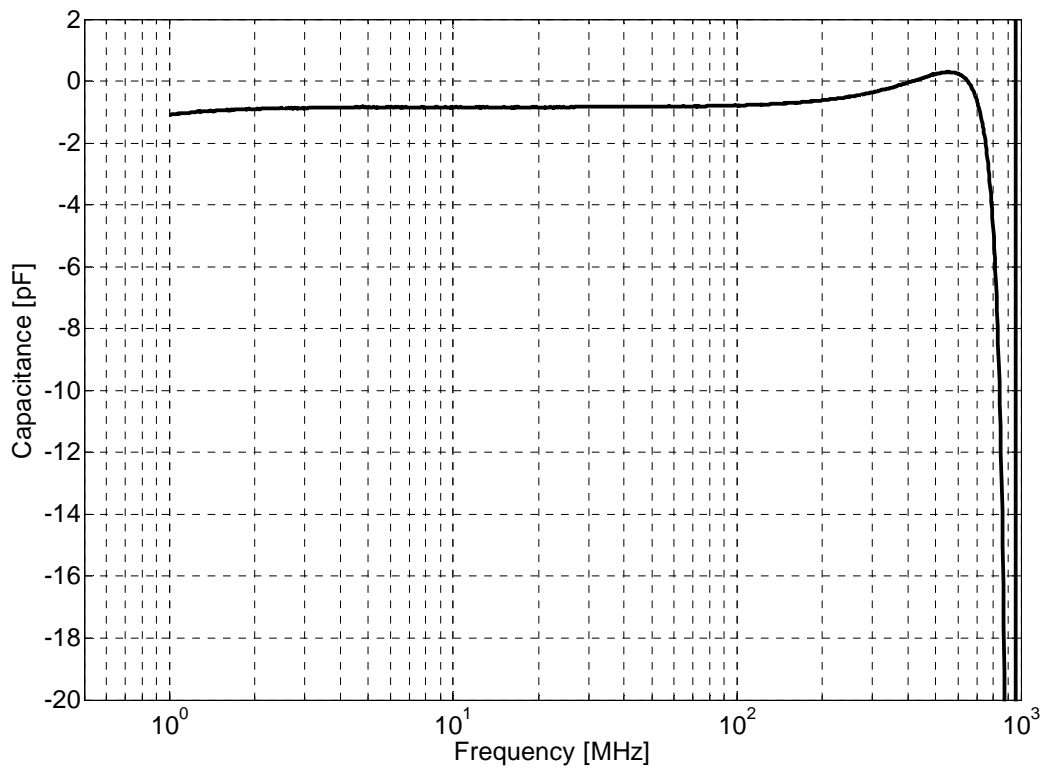
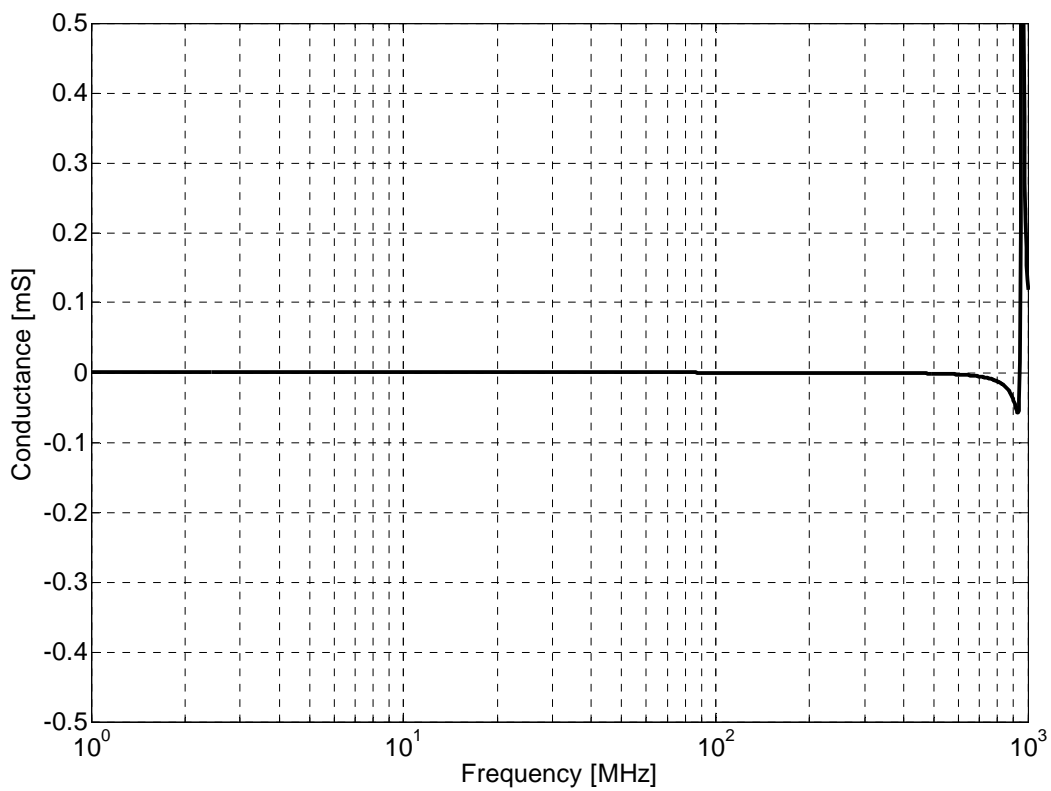


Figure 4-53 Simulations of the tunable negative capacitor ($V_{BIAS} = 4$ V)
a) generated capacitance b) generated conductance



a)



b)

Figure 4-54 Simulations of the tunable negative capacitor ($V_{BIAS} = 3$ V)
a) generated capacitance b) generated conductance

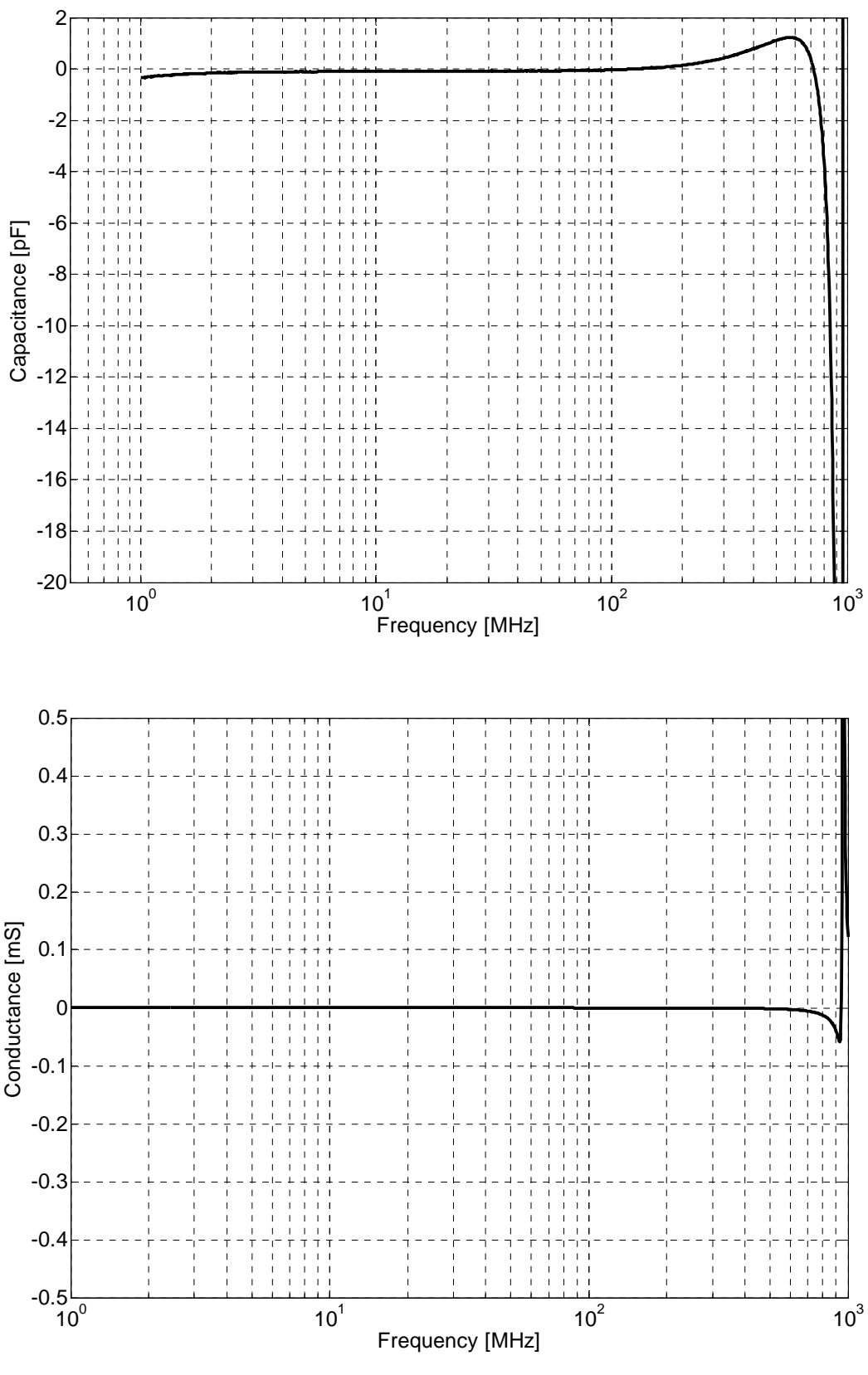


Figure 4-55 Simulations of the tunable negative capacitor ($V_{BIAS} = 2$ V)
a) generated capacitance b) generated conductance

4.4.4. OP-amp-based tunable negative inductor (100 kHz- 700 MHz)

In order to add a tuneability feature to a negative inductor, we used the previously designed circuit from the section 4.3.3 (Figure 4-34) and upgraded it with the PIN-based tuning circuit (Figure 4-56). The PIN diode (BA595) was connected as a (variable) shunt resistance in the negative feedback loop. Furthermore, the PIN diode was biased via a series combination of the choke (270 nH) and the resistor (220 Ω). Since the gain of the amplifier is different than that in the section 4.3.3, it was necessary to change the elements in the positive feedback loop, as well. One of the problems was achieving a large value of a coupling capacitor that is connected in series with the inverting inductor. Therefore, it was decided to use several capacitors for this purpose. In addition, due to the input capacitance of the AD8099 OPamp, it was necessary to choose the values of the stabilizing inductor very carefully (in order to avoid unwanted resonant behavior).

At first, a series of ADS circuit simulations (with the SPICE model of BA595 PIN diode) were performed and the values of the used elements were optimized. After the satisfactory results were achieved (in the range 100 kHz- 700 MHz), the circuit was manufactured (Figure 4-57), and measured with the help of an ZVL8 VNA. The measurement results and the simulations are compared in Figure 4-58, Figure 4-59, Figure 4-60, Figure 4-61, Figure 4-62, and Figure 4-63 (for the DC bias voltages of 0.8 V–5 V). Again, it can be seen that the measured values agree with the simulation results well, up to the frequency of 600 MHz. Above that frequency, the negative inductance becomes dispersive and this dispersion depends on the biasing voltage. Additional thorough investigation revealed that the cause of this behavior is twofold. At first, it was again found that the inductance of an SMA inner pin affects the results. Secondly, this effect is now even more pronounced due to the change of the amplifier gain. In spite of that, dispersion it is still acceptable up to the frequency of 700 MHz.

As far as the tuning is concerned, it can be seen that it was possible to achieve negative inductance from -5 nH to -9 nH within the frequency band of 100 kHz – 600 MHz. Due to the dispersion, the tuning range becomes -10 nH to -15 nH for the frequencies in the range of 600 MHz – 700 MHz. As in the previous case, (section 4.3.3) additional simulations showed that a negative inductor without the SMA connector should have a maximal operating frequency above 700 MHz with moderate dispersion behavior ($\pm 20\%$). In spite of the explained problems these results are promising. To the best of our knowledge there has not been any other successful implementation of a tuneable negative inductor in discrete technology yet. As stated before, we believe that it is very difficult to achieve better results without the use of microelectronic technology.

At this point, it is interesting to compare achieved results with those from the only published successful realization of a tuneable negative inductor [98]. The tuning range obtained in [98] was -40 nH to -60 nH. Although these values are larger than obtained in our prototype (-5 nH to -9 nH), the relative tuning ranges are similar (66% in [98] and 56% in our prototype).

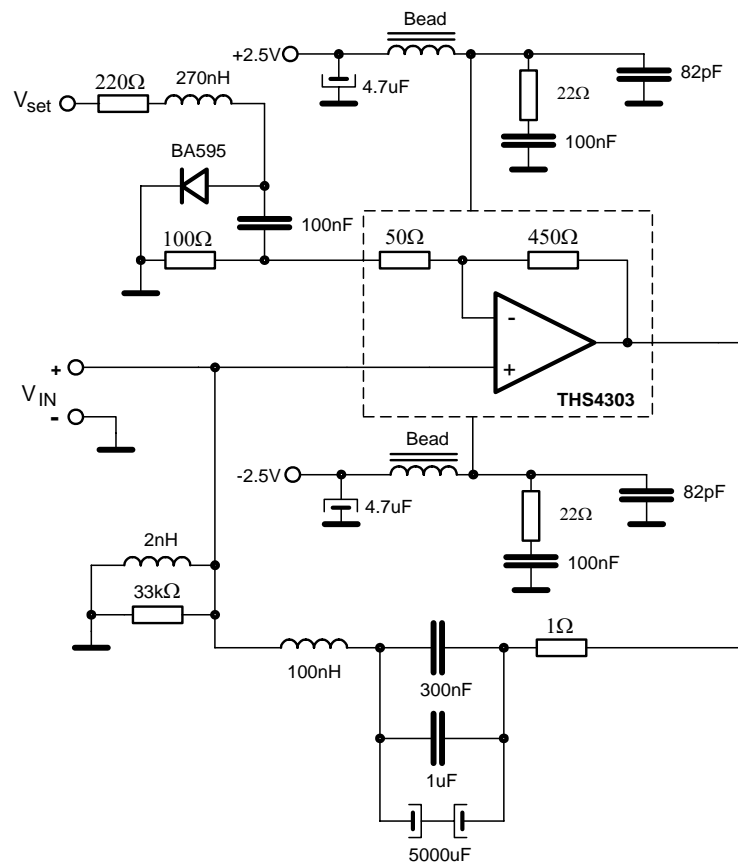


Figure 4-56 Circuit diagram of the tunable negative inductor (100 kHz – 700 MHz)

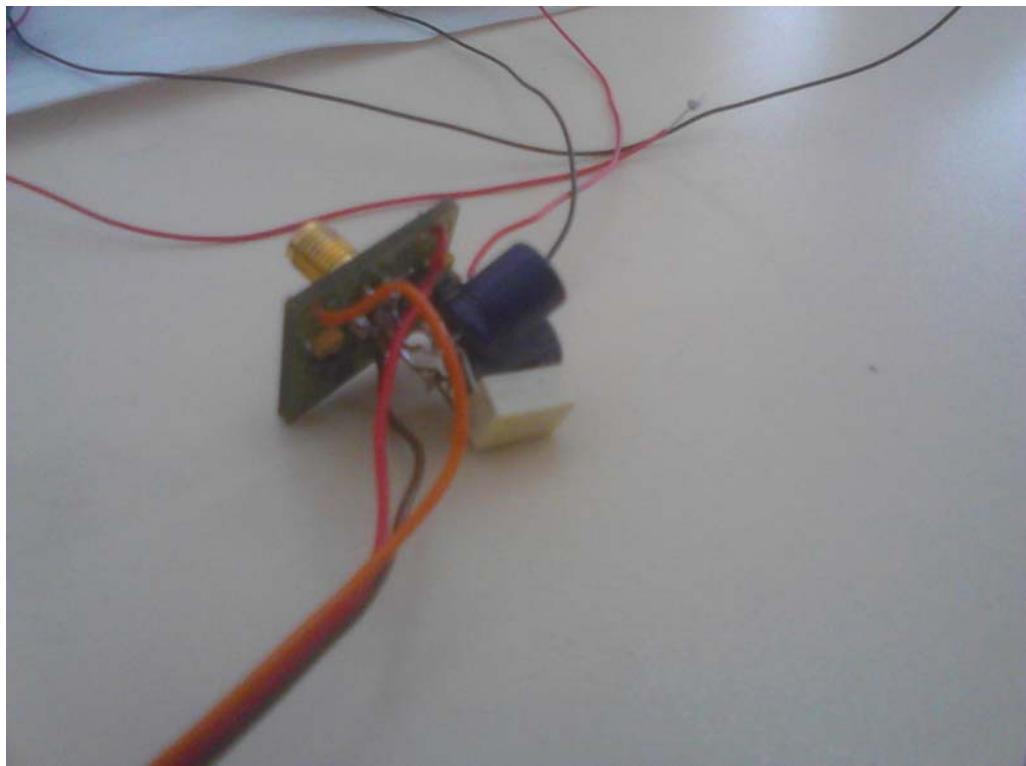


Figure 4-57 The photograph of the tunable negative inductor (100 kHz – 700 MHz)

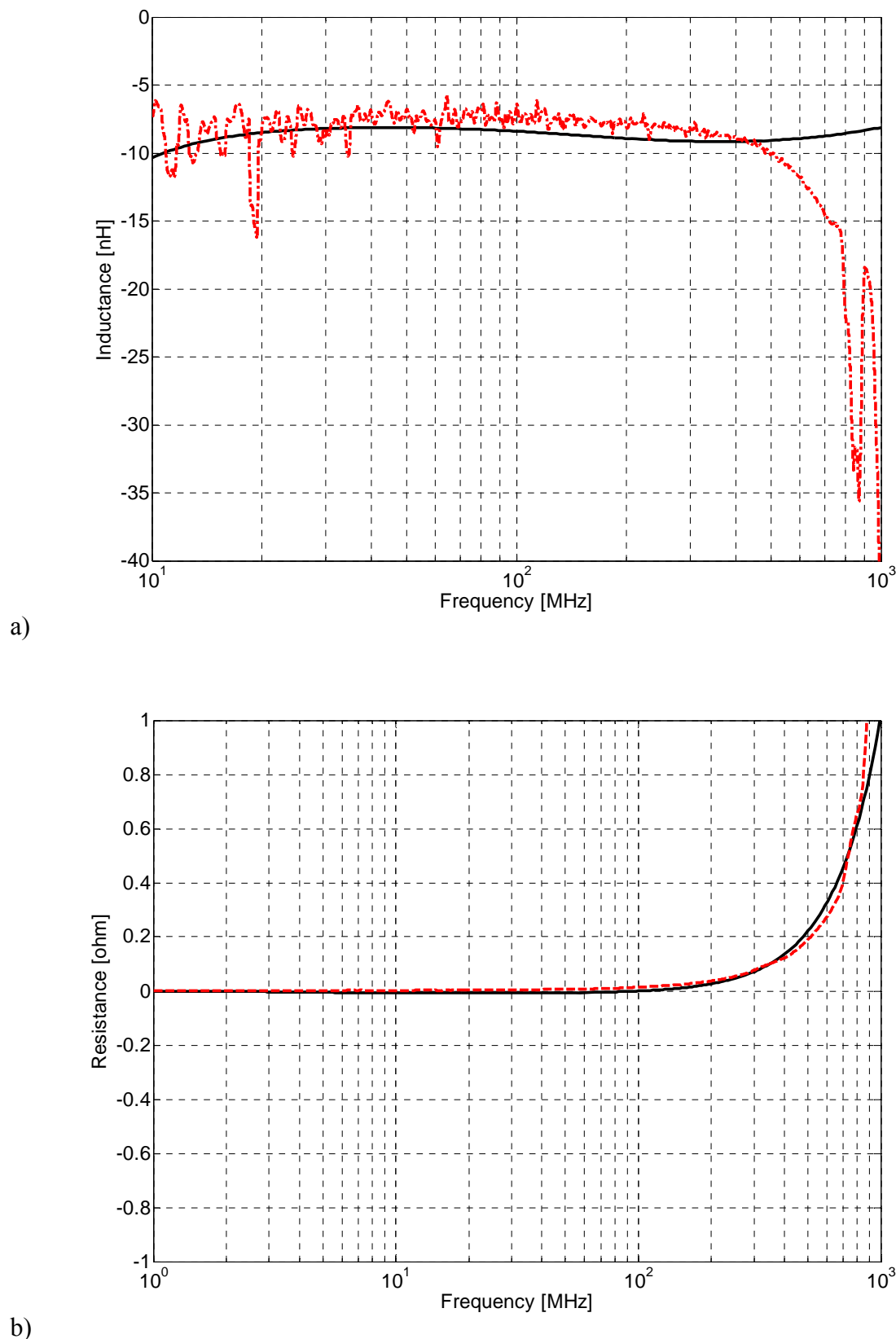


Figure 4-58 Measurements of tunable negative inductor ($V_{BIAS} = 0.8$ V) a) generated inductance (solid black – simulations, dashed red - measurements) b) generated resistance (solid black – simulations, dashed red - measurements)

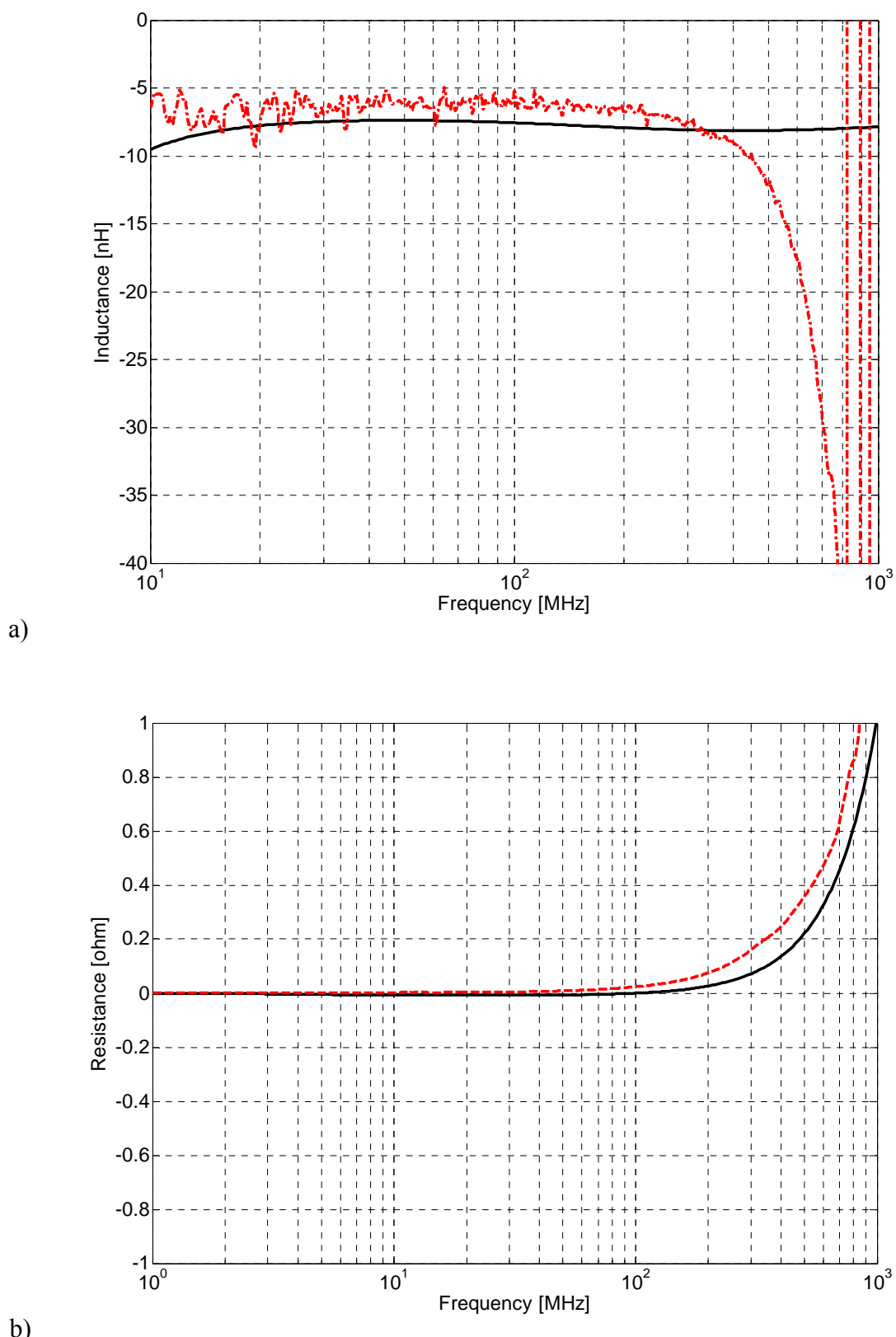


Figure 4-59 Measurements of tunable negative inductot ($V_{BIAS} = 1$ V) a) generated inductance (solid black – simulations, dashed red - measurements) b) generated resistance (solid black – simulations, dashed red - measurements)

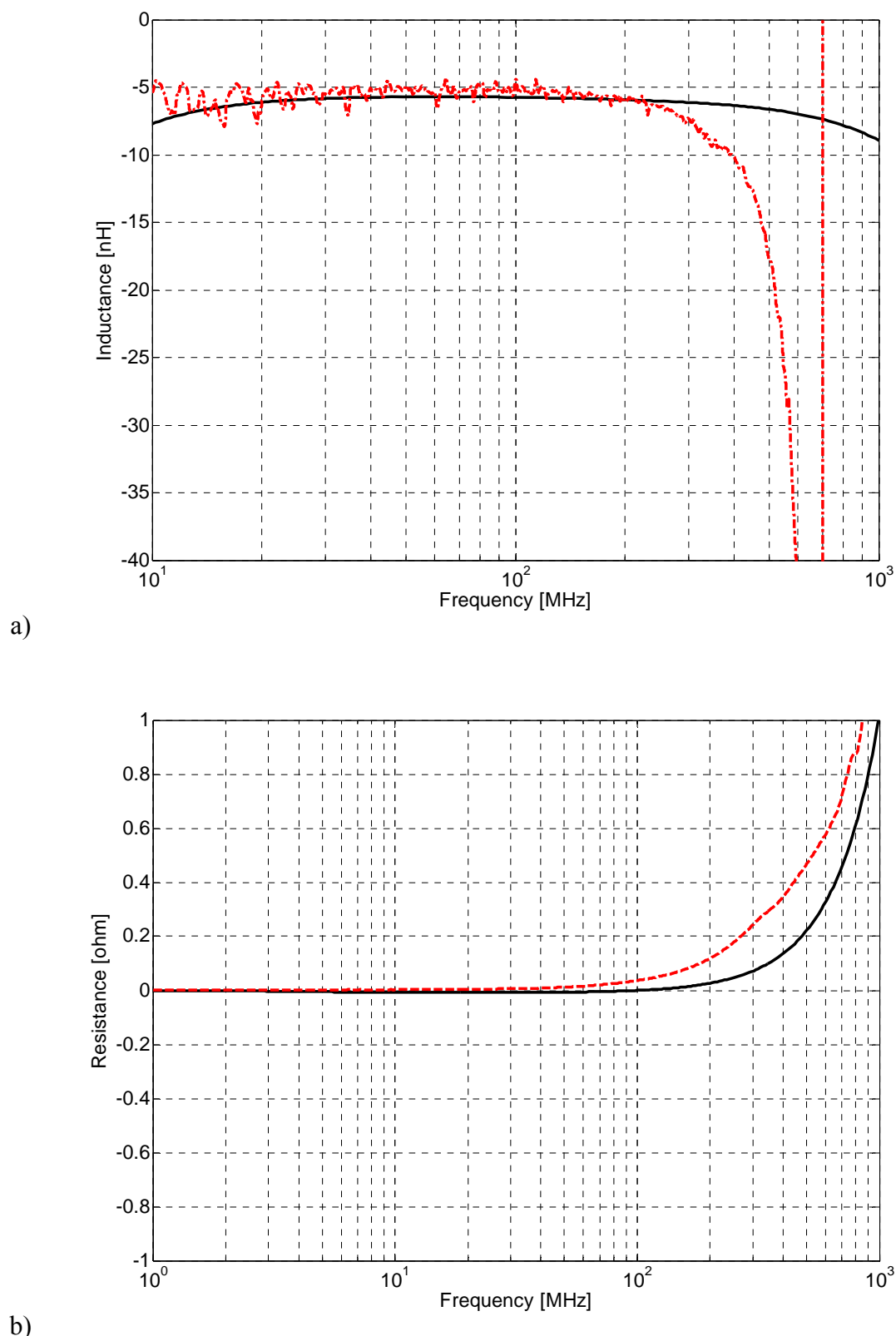


Figure 4-60 Measurements of tunable negative inductot ($V_{BIAS} = 2$ V) a) generated inductance (solid black – simulations, dashed red - measurements) b) generated resistance (solid black – simulations, dashed red - measurements)

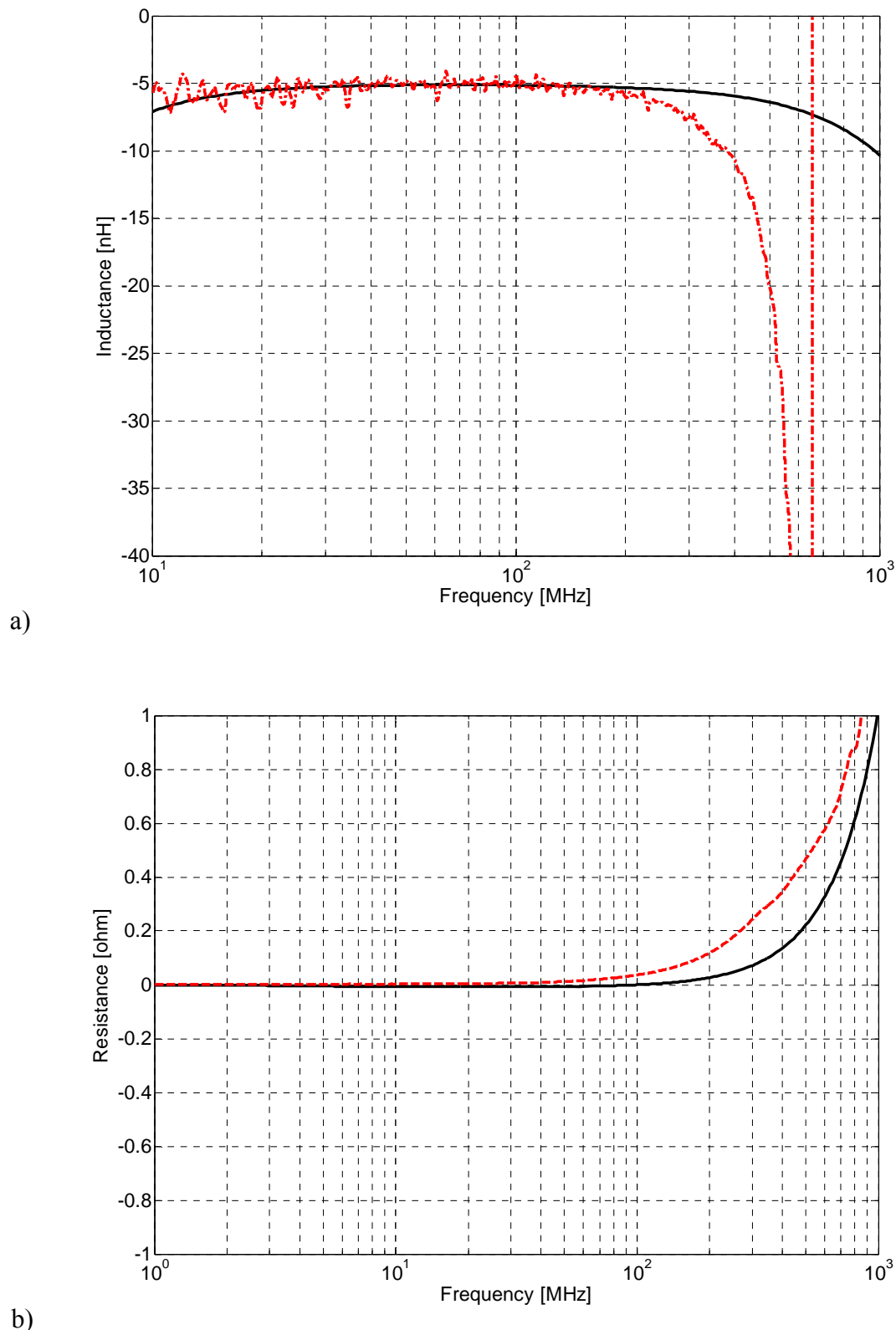


Figure 4-61 Measurements of tunable negative inductot ($V_{BIAS} = 3$ V) a) generated inductance (solid black – simulations, dashed red - measurements) b) generated resistance (solid black – simulations, dashed red - measurements)

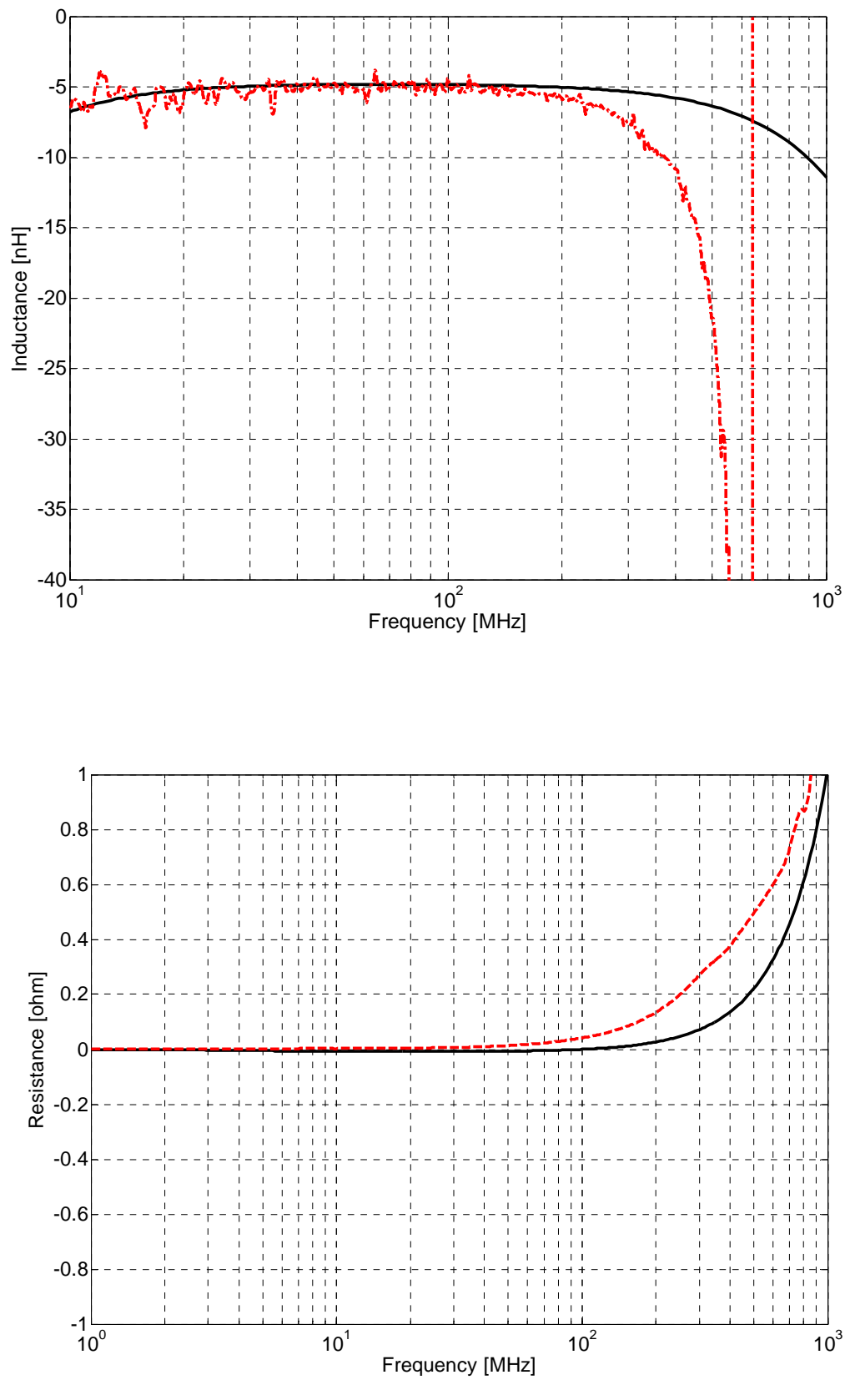


Figure 4-62 Measurements of tunable negative inductance ($V_{BIAS} = 4$ V) a) generated inductance (solid black – simulations, dashed red - measurements) b) generated resistance (solid black – simulations, dashed red - measurements)

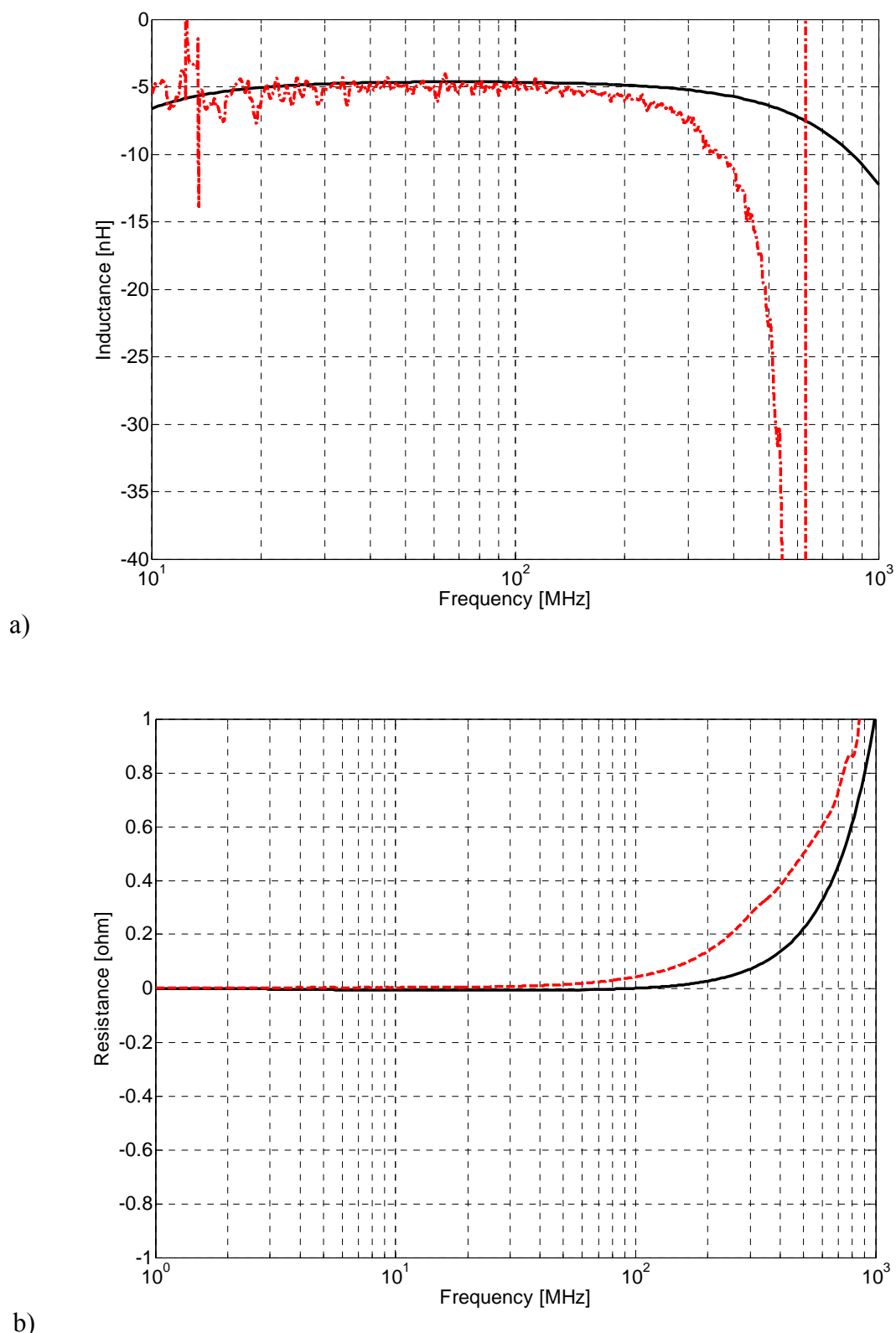


Figure 4-63 Measurements of tunable negative inductance ($V_{BIAS} = 5$ V) a) generated inductance (solid black – simulations, dashed red - measurements) b) generated resistance (solid black – simulations, dashed red - measurements)

4.4.5. Tunable/reconfigurable DPS-ENZ and DPS-MNZ unit cells

We attempted to test the developed tuneable negative capacitors and inductors in a reconfigurable metamaterial unite cells. The construction of all these unit cells was very similar to previously described cases (sections 4.2.3. and 4.3.4). Each unit cell contained either the section of a microstrip transmission line shunted with the negative capacitor, or with the negative inductor connected in series. The following results were obtained after the extraction procedure:

- AD8099-based DPS-ENZ cell: relative permittivity of 0.2 – 1.5 (dispersion \pm 15%, operating bandwidth 2 MHz -40 MHz).
- THS4303-based ENZ cell: relative permittivity of 0.2 – 0.6 (dispersion \pm 20%, operating bandwidth 300 MHz-700 MHz (using a MA 45228-30 varactor). The whole operating bandwidth could not be tested because the optimal varactor diode BBY-53-02 was not available). The simulation of the ENZ unit cell with BBY-53-02 varactor revealed the relative permittivity of 0.2 – 0.8 (dispersion \pm 15%, operating bandwidth 100 kHz-700 MHz).
- THS4303-based MNZ cell: relative permittivity of 0.3 – 0.5 (dispersion \pm 20%, operating bandwidth 100 kHz-700 MHz).

It can be concluded that the feasibility of adding tuneability/reconfigurability to a non-Foster metamaterial unit cells has been demonstrated.

4.5. Towards a microelectronic non-Foster metamaterial unit cell

(*The part of the results presented in the section 4.5 were achieved with the help of Bosko Mrkovic, who is a Ph.D student at University of Zagreb).

In sections 4.2, 4.3. and 4.4. it was shown possible to build a stable tuneable negative capacitors and negative inductors. These devices used cheap OPamp technology and operated in the bandwidth 100 kHz -700 MHz. So the maximal operating frequency lied in the UHF band. We believe that the achieved maximal operating frequency can be hardly improved further without switching to the microelectronic technology (specially designed MMICs).

Microelectronic technology is not available at the University of Zagreb. Therefore, we put some preliminary efforts towards the design of the microelectronic non-Foster metamaterial unit cell. So far, we have studied possible realizations of a negative capacitor. We hope that in the future it would be possible to find a partner with available processing microelectronic facilities.

As the basic element of future microelectronic version of unit cell, we decided to use a negative capacitor with cross-coupled FET-based (Figure 4-64).

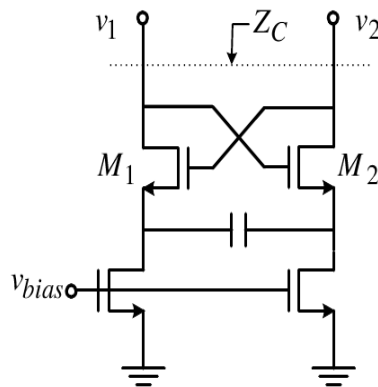


Figure 4-64 Floating NIC with two FET's

This is a floating type of a NIC, which has been used for decreasing the input capacitance of microwave amplifiers [60] and in the construction of an inductorless integrated oscillator [61]. It resembles a relaxation oscillator (without the cross-capacitors) and it inverts the impedance connected between the source electrodes of two FETs. It is interesting that this very recent and popular design is actually a modern version of one of the first vacuum-tube-based NICs proposed back in 1951 [62]. An approximate equation for the input impedance [60] is given by:

$$Z_{in} \approx -\frac{1}{j\omega C} \frac{g_m + j\omega(C_{gs} + 2C)}{g_m}, \quad \omega \ll \omega_t. \quad (4.1)$$

Here, C is the load capacitance and C_{gs} stands for the internal capacitance between the gate and source electrodes, and g_m is the FET transconductance. This circuit is used exclusively in the microelectronic version, which allows extremely broad operating bandwidth (a prototype reported in [60] used 180 nm CMOS technology and generated capacitance of -60 fF in the frequency range 100 MHz – 1.9 GHz). It could be even possible to extend the operating frequency up to more than 20 GHz using modern 90 nm technology. This circuit seems to be a very good candidate for applications in the proposed active ENZ or MNZ metamaterial. The only possible drawback might be the low value of the generated negative capacitance (or inductance).

We attempted to design a similar NIC, operating as a negative capacitor in a very cheap 130nm CMOS technology using the CadenceTM CAD environment. The circuit diagram is sketched in Figure 4-65. Figure 4-66 depicts the simulated input capacitance for three different values of the inverting capacitors. It can be seen that the increase of the capacitance of the inverting capacitor decreases the bandwidth. Input capacitance of -10 pF can be achieved only to the maximal frequency of 10 MHz, while the input capacitance of -1 pF is feasible up to 1 GHz.

In order to overcome this unwanted behavior, it could be possible to use a bank of negative capacitors connected in parallel. This idea is shown in Figure 4-67. It depicts the input capacitance for three different banks of negative capacitors. The banks are designed in such a way that the capacitance of each negative capacitor is scaled down by the number of the capacitors. It assures required net negative capacitance although each NIC generates smaller capacitance. It can be clearly seen that this approach enables broadening of the

bandwidth without sacrificing the value of the generated negative capacitance. For instance, one NIC can generate the capacitance of -5 pF up to the frequency of 10 MHz , while the bank of 50 NICs can generate the capacitance of -5 pF up the frequency of 1 GHz .

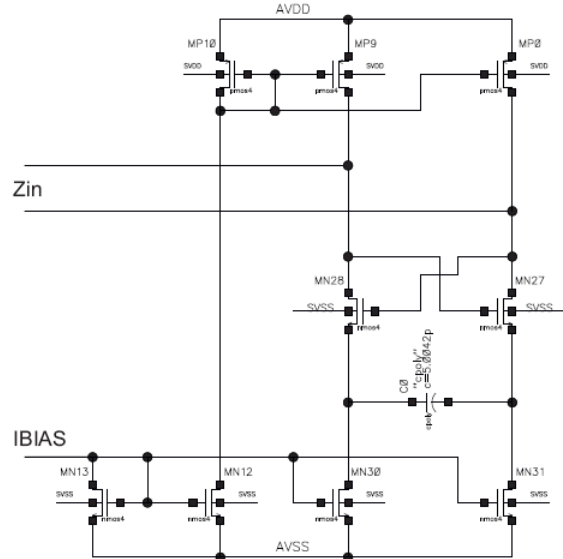


Figure 4-65 A simplified circuit of CMOS negative capacitor

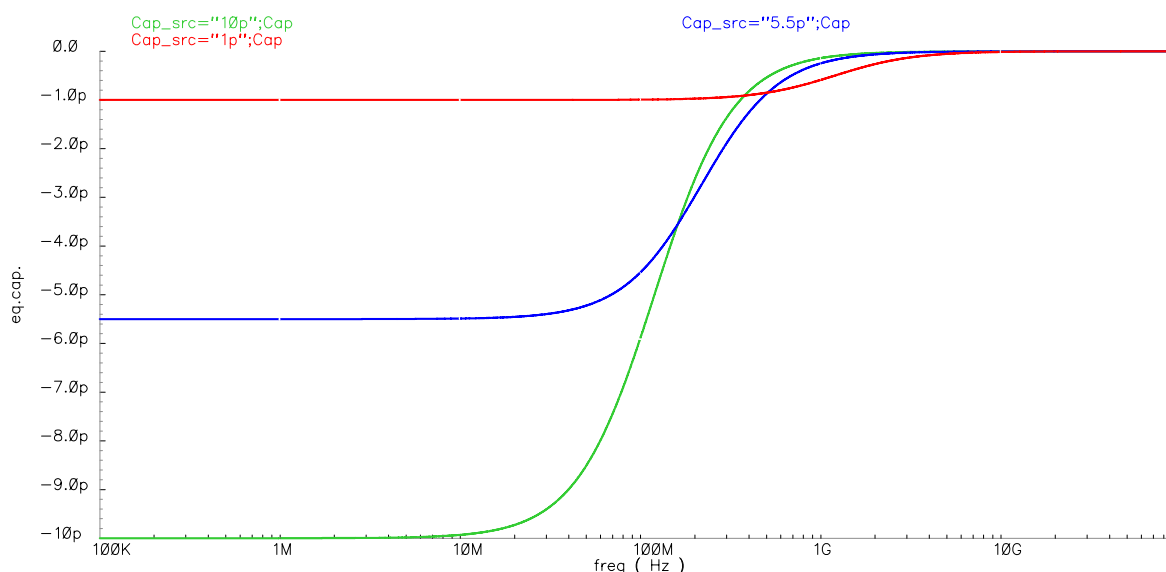


Figure 4-66 Simulated input capacitance of a CMOS negative capacitor (green; $C=-10 \text{ pF}$, blue; $C=-5.5 \text{ pF}$, red $C=-1 \text{ pF}$)

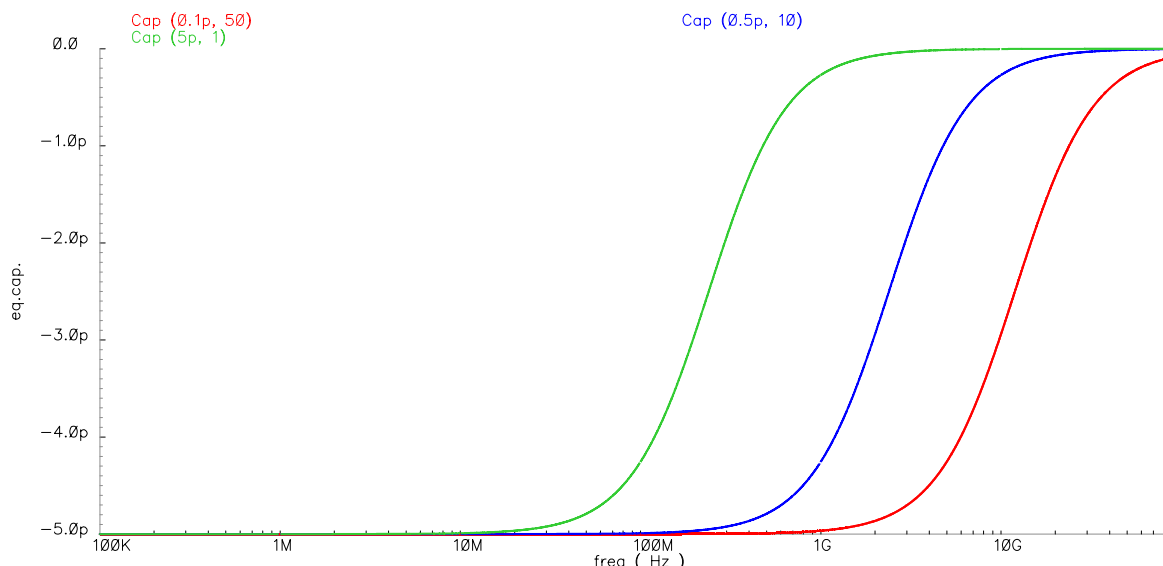


Figure 4-67 Simulated input capacitance of a CMOS negative capacitor (green;5x(-1 pF), blue; green;10x(-0.5 pF), red green;50x(-0.5 pF)

Some additional simulations showed that with the use of a standard 65 nm CMOS technology it should be possible to increase the highest operating frequency into the microwave regime (above 10 GHz). Adding the tuneability feature seems to be very straightforward, by integration of the MOSFET-based varactor as a load in the circuit in Figure 4-64.

Presented results are very preliminary, but they show that the microelectronic approach can significantly increase the versatility of non-Foster elements and their applications in metamaterials. There are several papers that report successful realization of microelectronic negative capacitors, application of which was to decrease the input capacitance of the amplifiers [60,61]. However, possible applications in the metamaterial field (apart from the very recent paper about the application of a variable negative inductance in artificial PMC surface [99] have not been reported so far.

4.6. Towards volumetric non-Foster metamaterials interfaced to free-space

(*The part of the results presented in the section 4.6 were achieved with the help of Iva Malcic, who is a Ph.D student at University of Zagreb).

The first practical realization of a non-Foster 1D metamaterial uses a microstrip transmission line loaded with negative capacitor [74]. The 2D variant of a non-Foster metamaterial has not been reported yet (there was one experimental demonstration of a 2D ENZ unit cell with a possible application in cloaking technology [66]). All these approaches actually use transmission lines, thus they are of a planar nature. They are convenient for the integration into standard microwave planar devices but their use in free-space scattering applications (such as cloaking) needs further investigation.

The basic idea deals with ‘interfacing’ of a transmission-line metamaterial (produced, for instance, in strip-line-like technology) via ‘antenna’ (Figure 4-68). The coupling to free space is achieved by ‘flaring’ the transmission at both its ends. This ‘flarings’ operate as antennas and convert the plane wave that propagates in the free-space into a guided EM wave. Several cases have been investigated by full-wave simulation with the help of a commercial CSTTM Microwave Studio EM solver. At first, three wavelength long empty transmission line,

equipped with two ‘antennas’ was simulated. It can be seen (Figure 4-68) that the EM wave is indeed coupled to the line and converted into the guided wave. In the next step, the model with the transmission line filled with hypothetical ENZ metamaterial was prepared. The simulation showed the increase of the wavelength, which is one of the basic characteristics of an ENZ metamaterials. Finally, the model of the transmission line was loaded with realistic negative capacitors, properties of which were taken from the measurements of developed prototypes (chapter 4). It can be seen that the structure is indeed coupled to the free space and that it shows ENZ behavior.

The drawback of this approach is the fact that the ‘flaring’ should be rather long (in the order of half of the wavelength) in order to minimize the reflections. In addition, the inclusion of the ‘flaring’ inevitably decreases the operating bandwidth.

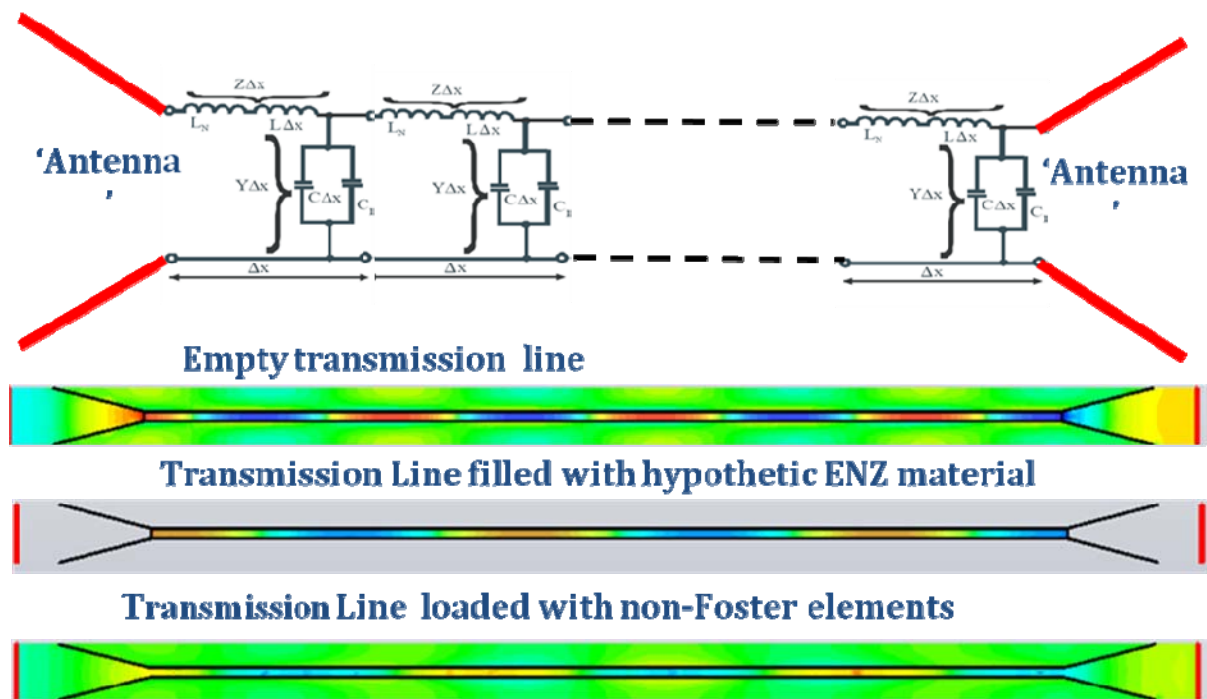


Figure 4-68 Interfacing of the transmission-line non-Foster metamaterial with free-space via ‘antenna’ layer

The next idea might be the use of bare transmission lines loaded with non-Foster elements designed in such a way that they are directly coupled to free space without any reflections [76]. The basic idea is to stack many layers of 2D transmission-line-based metamaterials in such a way that the vector of the incoming plane wave is perpendicular to the layers (Figure 4-69, Figure 4-70). If the transmission line is properly designed, it is possible to convert the incoming plane wave into a guiding wave without any reflection. In such a way, one would have a 2 1/2 D ultra-broadband non-Foster metamaterial.

Very recently, we reported the possible use of this approach in cloaking technology [77]. At first, the 2 1/2 D model of non-Foster anisotropic cloak, based on the idea from Figure 4-69, was prepared in CST Microwave Studio environment. The values of negative capacitors and negative inductors used in the model were taken from the measurements of the prototypes. The results of the simulations of the power scattering ratio (the quantity related to the radar cross-section) clearly shows that the use of a non-Foster metamaterials would yield extremely broad bandwidth (more than two octaves, comparing to the few percent relative bandwidth of a passive cloak).

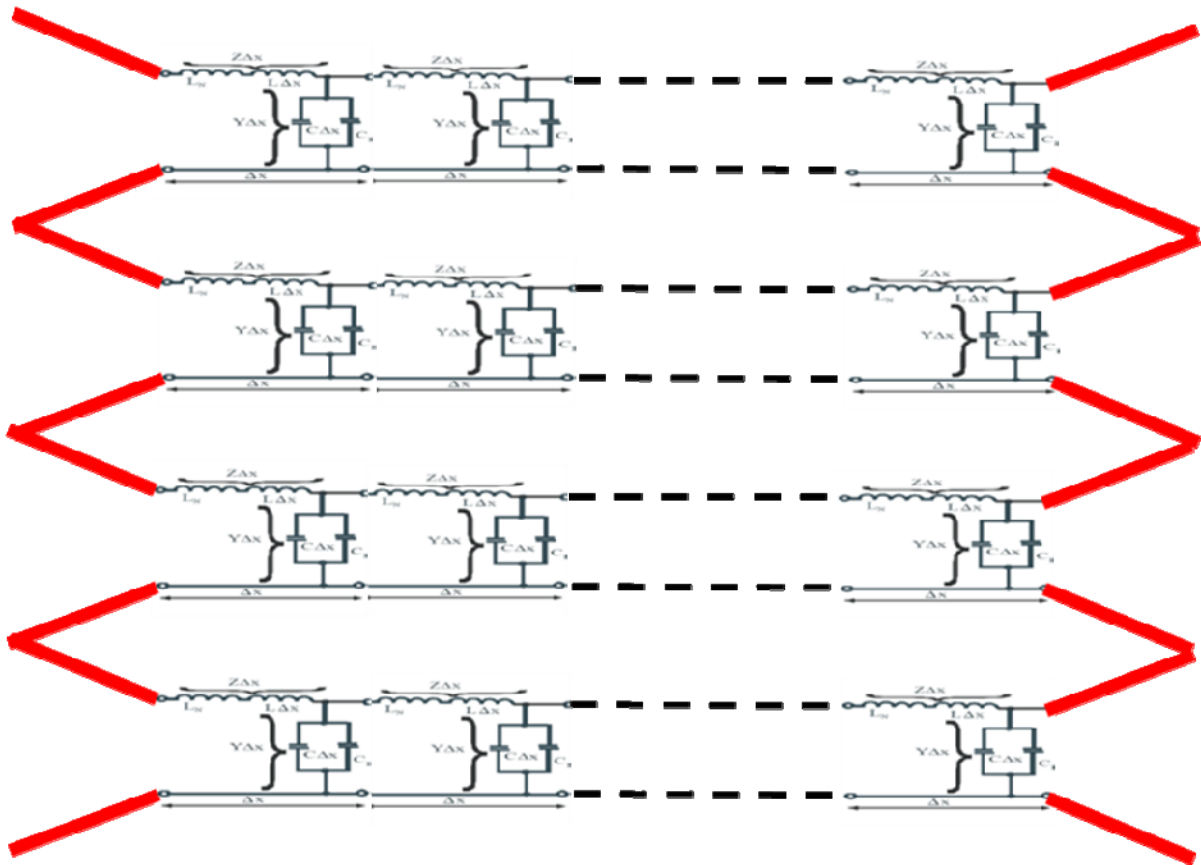


Figure 4-69 Stacking the transmission line non-Foster metamaterials with ‘flarings’

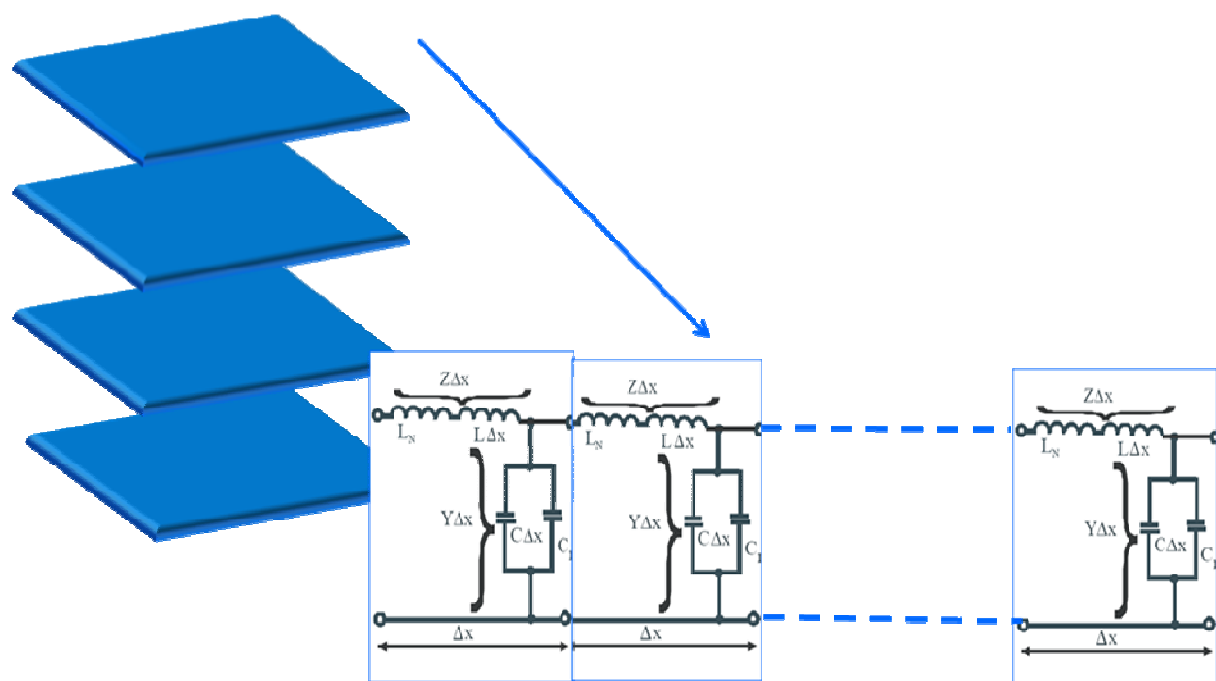


Figure 4-70 An idea of 2 1/2 D non-Foster metamaterial

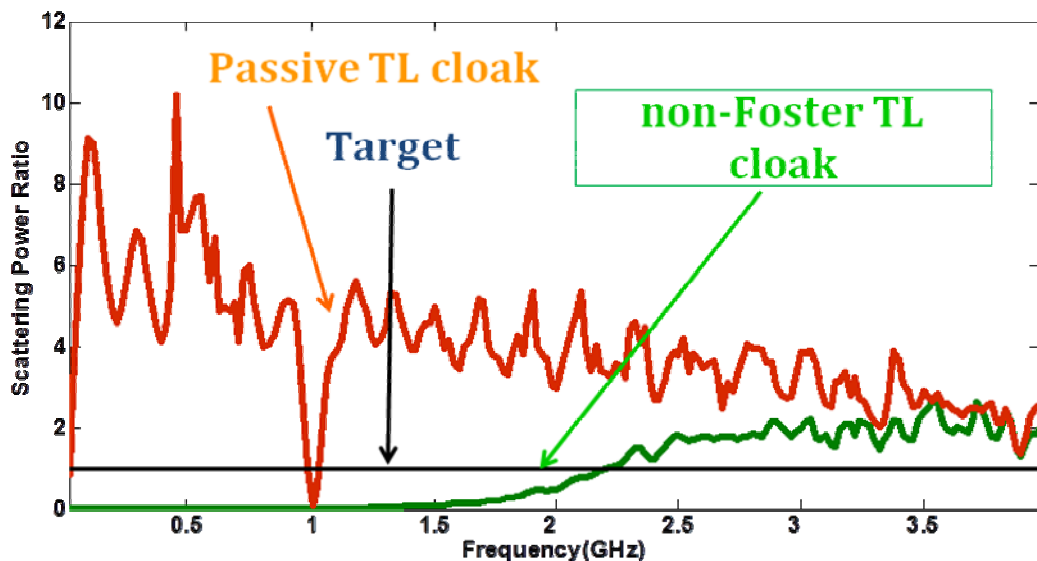


Figure 4-71 The bandwidth comparison between a passive cloak and a cloak based on non-Foster metamaterials

The realization of all presented ideas would be very elegant with the use of tuneable/reconfigurable non-Foster metamaterials. In such a way it would be possible to achieve the desired values of the equivalent permittivity and permeability (thus ENZ, MNZ or DPS behavior) by in-situ tuning. This might pave a way towards the ‘on-the-demand’ metamaterials, properties of which could be tailored for a particular, specific application.

4.7. Summary

In this chapter, the efforts toward increasing the versatility of non-Foster metamaterials have been reported. The most important achievements are summarized below:

- It has been shown possible to increase the highest operating frequency of a non-Foster ENZ metamaterial towards UHF and microwave parts of the EM spectrum. We have designed, simulated and built the prototypes of the active, ultra-broadband, non-Foster ENZ unit cells that operate from 100 kHz to 700 MHz. This bandwidth (1:700 or more than 9 octaves) surpasses the bandwidth of all passive and active metamaterials available at the present state of the art. The main part of the developed unit cell is a negative capacitor based on a commercial ultra-fast OPamp. We believe that the achieved bandwidth can hardly be improved further, without switching to the microelectronic technology (specially designed MMICs).

- We have analyzed a feasibility of construction of a stable RF negative inductor that would enable development of non-Foster MNZ metamaterials. We have designed, simulated and measured two prototypes of negative inductors and associated MNZ unit cells. The first prototype uses a modified Kolev's circuit [59] and generates effective inductance of -60 nH within the bandwidth 1 MHz-50 MHz. The second prototype uses an OPamp and generates effective inductance of -10 nH within the bandwidth 100 kHz-700 MHz. As far as our knowledge goes, these are the best results available at the present state of the art (using technology of discrete components). Further improvement could eventually be possible by the use of the microelectronic technology. Our numerical study showed that it should be possible to increase the highest operating frequency above 10 GHz by the use of standard 65 nm CMOS technology.
- We have analyzed a feasibility of adding tuneability/reconfigurability features to the developed negative capacitors/inductors and the associated unit cells of ENZ/MNZ metamaterials. The capacitance between -25 pF and -100 pF, within the bandwidth of 1 MHz-40 MHz (OPamp-based prototype) was achieved experimentally. The negative inductance prototype achieved the inductance between -5 nH and -10 nH, within the bandwidth of 100 kHz-700 MHz. Finally, we have built an associated reconfigurable DPS-ENZ and DPS-MNZ unit cell and demonstrated its operation.
- We have analyzed a feasibility of extension of the developed planar ENZ/MNZ metamaterials toward volumetric applications. The approach was based on either 'interfacing' the TL structure to free-space via an array of 'antennas' or the use of a properly designed 'bare' transmission lines loaded with non-Foster elements. Full-wave simulations proved correctness of the basic idea.

Chapter 5 CONCLUSIONS AND FUTURE WORK

Conclusions and future work

This study reports a 12-month research effort undertaken to increase the versatility of recently introduced ENZ and MNZ non-Foster metamaterials. Using the non-Foster metamaterials, it is possible to overcome the basic dispersion-energy constraints (and, therefore, to overcome the inherent narrowband operation) of passive metamaterials by incorporation of non-Foster elements into standard transmission-line-based structures. The results published so far revealed almost dispersionless ultra-broad bandwidth of more than four octaves. This bandwidth is considerably wider than the bandwidth of all passive ENZ metamaterials available at present and this clearly proves the correctness of the proposed novel concept. However, almost all published experiments were limited to a maximal operating frequency that lies either in low RF range (up to 100 MHz).

In this project, we have extended the frequency of operation into the UHF region and, at the same time, increased the versatility of non-Foster-element-based metamaterials. It was done by the development of specially designed reconfigurable unit cell. This unit cell is *in-situ* reconfigurable (by external DC control signal) and able to achieve either DPS-ENZ or DPS-MNZ behavior. Using this novel approach, the same unit cell could be inserted into various transmission-line-based structures and (depending on its configuration) enable different applications in RF engineering and antenna technology.

As a short summary, the realized outcomes of the project are:

- We have improved the understanding of the basic physics of a negative capacitance phenomenon by the analysis of a response of a negative capacitor to a pulse excitation. Towards this end, we have developed a low-frequency laboratory demonstrator based on a commercial integrated audio amplifier. Developed model generates large negative capacitance (-1.2 μ F to -0.6 μ F in the frequency range from 1 kHz-25 kHz). All the measurements show that a negative capacitor could be interpreted as a generator/sink.
- We have improved the analysis of stability of the negative-capacitor-based metamaterials. We have developed a realistic one-pole, two-pole and three-pole models of a dispersive negative capacitor. The developed model showed very good agreement with both the SPICE-based simulations and the measurements on the manufactured prototypes across the whole operating bandwidth.
- We have performed a detailed experimental investigation of a recently observed simultaneous superluminal phase and group velocities in a non-Foster ENZ metamaterials and found that, although being counter-intuitive, this behavior is in perfect agreement with the causality requirements.
- We have investigated the basic physics of a negative non-Foster RLC tank circuit. A simple analytical study revealed that this circuit is stable if it is driven by a generator, internal resistance of which is smaller than the absolute value of the negative resistance in the non-Foster RLC tank circuit. We have manufactured the experimental prototype operating in the lower RF region (up to 70 MHz) and the measurements of input reflection coefficient indeed showed a stable behavior. To the best of our

knowledge, this is the first experimental demonstration of stable negative RLC tank circuit.

- We have analyzed the feasibility of increasing the highest operating frequency of a non-Foster ENZ metamaterial towards UHF and microwave parts of the EM spectrum. We have designed, simulated and built the prototypes of an active, ultra-broadband, non-Foster ENZ unit cells that operate in the frequency range 100 kHz -700 MHz. This bandwidth (1:700, or more than 9 octaves) surpasses the bandwidth of all passive and active metamaterials available at the present state of the art. The main part of the developed unit cell is a negative capacitor based on a commercial ultra-fast OPamp. The developed negative capacitor generates a capacitance of -5 pF with negligible losses, across the whole bandwidth. We believe that the achieved bandwidth can be hardly improved further without switching to the microelectronic technology (specially designed MMICs).
- We have analyzed a feasibility of construction of a stable RF negative inductor that would enable development of non-Foster MNZ metamaterials. We have designed, simulated and measured two prototypes of negative inductors and associated MNZ unit cells. The first prototype uses a modified Kolev's circuit and generates effective inductance of -60 nH within the bandwidth 1 MHz-50 MHz. The second prototype uses an OPamp and it generates effective inductance of -10 nH within the bandwidth 100 kHz–700 MHz. As far as our knowledge goes, these are the best results available at the present state of the art (using technology of discrete components). Further improvement could eventually be possible by the use of microelectronic technology.
- We have analyzed a feasibility of adding tuneability/reconfigurability features to the developed negative capacitors/inductors and the associated unit cells of ENZ/MNZ metamaterials. In order to achieve this goal, we have built two prototypes based on two different approaches: tuning based on a variable positive feedback loop and tuning based on a variable negative feedback loop. In the first approach (a case of the negative capacitor), the key element is a varactor diode that allows direct tuning of the effective capacitance (by applying an external DC voltage). Achieved capacitance was between -25 pF and -100 pF within the bandwidth 1 MHz-40 MHz (OPamp-based prototype). In addition, the range between -1 pF to -5 pF within the bandwidth 100 kHz-700 MHz (improved OPamp-based prototype) was designed. In the case of the negative inductor, we used a PIN diode configured as a variable resistor that controls the gain and, therefore, the value of the generated effective inductance. Achieved effective inductance was between -5 nH and -10 nH, within the bandwidth 100 kHz-700 MHz. Finally, we have built an associated reconfigurable DPS-ENZ and DPS-MNZ unit cells and demonstrated their operation.
- We have analyzed a feasibility of extension of the developed planar ENZ/MNZ metamaterials toward volumetric applications. The approach was based on ‘interfacing’ the TL structure to free-space via an array of ‘antennas’. Full-wave simulations proved correctness of the basic idea.

The future research efforts should be devoted to the realization of the reconfigurable ENZ/MNZ non-Foster unit cell in microelectronic technology. This would enable the extension of the maximal operating frequency into the microwave part of the EM spectrum. Integration of developed unit cells in various antenna/scattering devices such as electromagnetic cloaks would enable multi-octave operation, that is not feasible by the use of conventional passive metamaterials.

Chapter 6 BIBLIOGRAPHY

Bibliography

1. Smith, D., Willie J. et. al., 'A Composite Medium with Simultaneously Negative Permeability and Permittivity', *Physical Rev. Lett.*, Vol. 84 , No. 18, pp. 4184-4187, May 2000
2. Engheta, N., Ziolkowsky, R., (ed.), 'Metamaterials: Physics and Engineering Explorations', Wiley 2006
3. Eleftheriades, G. V., Balman, K.G , (ed.), 'Negative Refraction Metamaterials: Fundamental Principles and Applications', Wiley 2005
4. Caloz, C., Itoh, T., 'Electromagnetic Metamaterials: Transmission Line Theory and Microwave Applications', Wiley 2006
5. Hrabar, S.,' Application of Wire Media in Antenna Technology', a chapter in 'Metamaterials and Plasmonics, Fundamentals, Modeling, Applications', (ed. S. Suhdi, A. Sihvola, A.P. Vinogradov), NATO Science for peace and security, Springer, 2009
6. Hrabar, S., Bartolic, J., et al', Experimental Investigation of Subwavelength Resonator based on Backward-wave Meta-material', Proc. on IEEE Antenna and Propagation & URSI Symposium 2004.,pp. 2568-2571, Monterey 2004
7. Hrabar, S. Bartolic, J. et al., 'Waveguide Miniaturization Using Uniaxial Negative Permeability Metamaterial', *IEEE Tran. on Ant. Prop.*, Vol. 53, No. 1. , pp. 110-119, January 2005
8. Hrabar, S., Bartolic, J., Sipus, Z.,'Reply to "Comments on 'Waveguide Miniaturization Using Uniaxial Negative Permeability Metamaterial"', *IEEE Tran. on Antennas and Propagation*, **55**, pp. 1017-1018, May 2007
9. Hrabar, S., Zaluski D., 'Subwavelength Guiding of Electromagnetic Energy in Waveguide Filled with Anisotropic Mu-Negative Metamaterial', *Electromagnetics*, Vol. 28, No. 7. pp. 494-512, October 2008
10. Pendry, J. B.. 'Negative Refraction Makes a Perfect Lens', *Physics Review Letters*, Vol. 85, pp. 3966-1 - 3966-4, 2000
11. Grbic, A., Eleftheriades, J., 'Overcoming the Diffraction Limit with a Planar left-Handed Transmission-line lens', *Physical Review Letters*, Vol. 92, No.11, pp.117403-1 – 117403-4, November 2004
12. Alu, A., Engheta, N. Achieving Transparency with Metamaterial and Plasmonic Coatings, *Physical Review E*, Volume 72, No. 1, pp. 16623-1 - 16623-3, July 2005
13. Schurig, D., Mock, J., et. al.,' Metamaterial Electromagnetic Cloak at Microwave Frequencies', *Science*, pp. 977 -980, November 2006

14. Ivsic, B., Sipus, Z., et. al. , 'Analysis of Uniaxial Multilayer Cylinders Used for Invisible Cloak Realization', IEEE Tran. on Antennas and Prop., Vol 57, No. 5, pp. 1521-1527, April 2009
15. Freire, M. J. ,Marques, R, and Jelinek, L. 'Experimental demonstration of a $\mu = -1$ metamaterial lens for magnetic resonance imaging', Applied Physics Letters, Vo 93, pp. 231108-1 - 231108-3, December 2008
16. Landau, L.D., Lifshitz, E.M. , Pitaevskii, L.P. , 'Electrodynamics of Continuous Media', Butterworth Heinmann , 2002
17. Pozar, D.M. , 'Microwave Engineering', Third Edition. J. Wiley & Sons, 2005
18. Ravel B. et al., 'Synthesis of Broadband Negative Group Delay Active Circuits,' IEEE Int. Microwave Symp. 2007, pp. 2177-2180, Honolulu 2007
19. Gharavi, S., Mojahedi, M., 'Theory and Application of Gain-Assisted Periodically Loaded Transmission Lines with Negative or Superluminal Group Delays', Proc. on IEEE AP-S 2007, pp. 2373-2380, Honolulu 2007
20. Hrabar, S., Bonefacic, D., Muha, D., 'Numerical and Experimental Investigation Of Basic Properties Of Wire Medium-Based Shortened Horn Antennas ', Microwave and Optical Technology Letters, Vol. 51, No. 11, pp. 2748-2753, November 2009
21. Tretyakov, S., 'An Analytical Model of Metamaterials Based on Loaded Wire Dipoles', IEEE Tran. on Antennas and Prop., Vol 51, No. 10, pp. 2652-2658, October 2003
22. Auzanneau, F. ,Ziolkowski, R.W., 'Theoretical Study of Synthetic Bianisotropic Materials', Journal of Electromagnetic Waves and Applications, Vol 12, No 3., pp. 353-370, Jan. 1998
23. Ziolkowski, R.W., 'The Design of Maxwellian Absorbers for Numerical Boundary Conditions and for Practical Applications using Engineered Artificial Materials', IEEE Trans. Antennas Prop., Vol. 45, pp. 656-671, No 4, April 1997
24. Tretyakov S., Kharina, T., ' The Perfectly Matched Layer as a Synthetic Material With Active Inclusions', Electromagnetics, Vol 20, No.2, pp. 155-166, February 2000
25. Tretyakov, S., 'Meta-Materials With Wideband Negative Permittivity And Permeability', Microwave Opt. Technol. Lett. No 3, pp. 163-165, November 2001
26. Tretyakov S., Maslovski S, 'Veselago Materials: What is Possible and Impossible about the Dispersion of the Constitutive Parameters', IEEE Antenna and Prop. Magazine, Vol 49, No. 1, pp. 37-43, February 2007
27. Rajab, K., Yang. H., Di. B., Parini C., Vasquez, J., Philippakis, M., 'Stability of Active Magnetoinductive Metamaterials', J. Appl. Phys. Vol. 108, pp. 054904-054910, September 2010
28. Popa, B. I. and Cummer, S.A. 'An Architecture for Active Metamaterial Particles and Experimental Validation at RF,' Microwave Opt. Technology Lett. No. 49, pp. 2574-2577, October 2007
29. Hrabar, S., Krois, I., Matvijev, M., ' Is It Possible to Overcome Basic Dispersion Constraints and Achieve Broadband Cloaking?', Proc. on. 3rd International Congress

- on Advanced Electromagnetic -Materials in Microwaves and Optics, pp. 408-410, London 2009
30. Linvill, J. G. , 'Transistor Negative Impedance Converters' Proc. IRE, Vol. 41, pp. 725-729, June 1953
 31. Skahill, G., Ruish R.M. , et.al. 'Electrically Small, Efficient, Wide-Band, Low-Noise Antenna Elements', Proc. on the 1998 Antenna Applications Symposium, (in AFRL-SN-RS-TR-1999-86 Final Technical Report), UMAS 1998, pp. 214- 213, UMAS 1998
 32. Aberle, J., Lomak, R., 'Antennas with non-Foster Matching Networks', Morgan & Claypool, 2007
 33. Sussman-Fort, S.E, 'Matching Network Design Using Non-Foster Impedances', Presentation slides, http://www.ieee.li/pdf/viewgraphs/matching_network_design_non_foster_impedances.pdf
 34. Sussman-Fort, S.E, 'Non-Foster Impedance Matching of Electrically-Small Antennas', IEEE Trans. Antennas and Propagation, Vol. 57, No. 8, pp. 2230-2241, August 2009
 35. Sussman-Fort, S.E, 'Matching Network Design Using Non-Foster Impedances', International Journal RF and Microwave CAE, Vol 16, No. 2, pp. 135-142. March 2006
 36. Perry, A.K, 'Broadband Antenna Systems Realized from Active Circuit Conjugate Impedance Matching', Naval Postgraduate School, Monterey, September 1973
 37. Leifso, C.R, 'Design and Analysis of Novel RF Active Impedance Synthesizing Circuits', Ph.D. thesis, Department of Electrical and Computer Engineering, University of Calgary, April 2000
 38. Leifso C, Haslett, J.W, 'Active Tunable Inductor', United States Patent, Patent No: US 6,211,753 B1, April 2001
 39. Bit-Babik Di Nallo, G. C., Svilgelj, J., Faraone , A., 'Small Wideband Antenna with Non-Foster Loading Elements'. Proc. on Int. Conf. on Electromagnetics in Advanced Applications, pp. 105-107, Torino 2007
 40. Sussman-Fort, S. E., Rudish, R.M., 'Non Foster Impedance Matching for Transmit Applications'. Proc.on Int. Conf. On Antenna Technology Small Antennas and Novel Metamaterials, pp. 53-56, March 2006
 41. Sussman-Fort S.E, 'Gyrator-Based Biquad Filters and Negative Impedance Converters for Microwaves', International Journal RF and Microwave CAE, pp. March 1998
 42. Hirvonen, M., Hujanen, A., Holmberg, J, Sten, J.C.E. , 'Bandwidth Limitations of Dipoles Matched with Non-Foster Impedances'. Proc. on Int. Conf. on Antennas and Propagation, pp. 1-5, EuCAP 2007, Edinburgh 2007
 43. Kaja, A. 'High Gain Rectangular Broad Band Microstrip Antenna with Embedded Negative Capacitor and Chip Resistor', PIER, Vol. 78, pp. 421–436, January 2008
 44. Song, K, Rojas, R. 'Electrically Small Wire Monopole Antenna With Non-Foster Impedance Element', Proc on EuCap 2010, pp. 1-4, Barcelona 2010
 45. Hu, Z. , Kelly, J, Song, C, Hall, P, Gardner, P., 'Novel Wide Tunable Dual-band Reconfigurable Chassis-antenna for Future Mobile Terminals', Proceedings of the Fourth European Conference on 2010, pp. 1-5, Barcelona 2010

46. Ugarte-Munoz, E, Hrabar, S, Segovia-Vargas, D., 'Investigation of Stability of Negative Impedances in Active Metamaterials and Antennas', Proc. on Eucap 2011, pp.2059-2063, Rome 2011
47. Sedra A.S, Roberts G.W, Gohh F, 'The Current Conveyor: History, Progress and New Results', IEE Proc. Vol. 137, Pt. G, No. 2, pp. 78-87, April 1990
48. Eyllier, D, 'Outils de Synthèse Originaux pour la Conception de Dispositifs Actifs Microonde Intégrés - Application au Filtrage et à l'Amplification Faible Bruit', Ph.D. thesis, Universite de Limoges, May 2006
49. Jackson, R.W, 'Criteria for the Onset of Oscillation In Microwave Circuits', IEEE Transactions on Microwave Theory and Techniques, Vol. 40, No. 3, pp. 566-569, March 1992
50. -----, 'The FET Constant-Current Source/Limiter', Application Note AN103, Vishay Siliconix, March 1997
51. Cuthbert T.H, 'History of broadband impedance matching', IEEE Global History Network, August 2009
52. http://www.ieeeghn.org/wiki/index.php/History_of_Broadband_Impedance_Matching, November 2009
53. Qadir, A, 'Realization And Study of Current-Mode Filters and Oscillators for Integrated Circuit Implementation', Ph.D. thesis , NED University of Engineering and Technology, Karachi, Pakistan, 2003
54. Kolli K, 'CMOS Current Amplifiers: Speed versus Nonlinearity', Ph.D. thesis, Department of Electrical and Communications Engineering, Helsinki University of Technology, November 2000
55. Eloranta , P. 'Current Conveyors', Postgraduate Course in Electronic Circuit Design II, Helsinki University of Technology, 2004
56. Dolling, G., Enkrich C., Wegener, M. , Soukoulis, C. M., Linden, S., 'Simultaneous Negative Phase and Group Velocity of Light in a Metamaterial', Science, Vol. 312 no. 5775 pp. 892-894, May 2006
57. Bonic, I., 'Design of RF Negative Capacitor based on non-Foster Circuit with Operational Amplifier', Master Thesis, University of Zagreb, 2010
58. Cristal, E.G.,Podell, A., Cohn, S.B, 'Microwave Active Network Synthesis', Technical Report ECOM-0044-F, ECOM and Stanfrod Research Institute, February 1972
59. Kolev, S., Delacressonniere, B., Gautier, J, 'Using a Negative Capacitance to Increase the Tuning Range of a Varactor Diode in MMIC Technology', IEEE Transactions on Microwave Theory and Techniques, Vol. 49, No. 12, pp 2425-2430, December 2001
60. Park, H., Lee, S, Lee, J, Sangwook, N, 'A 0.1-1 GHz CMOS Variable Gain Amplifier Using Wideband Negative Capacitance', IECE Trans. Electron., Vol. E92-C, No.10, pp. 1311-1314, October 2009
61. Kwisung, Y., Mohammed M. et al. , 'Negative Impedance Circuit and Its Application to Inductorless Resonant Oscillators', in Proc. Int. SOC Conference 2007, pp.13-16, Seoul 2007
62. Merril, J.R., 'Theory of Negative Impedance Converter', Bell System Technical Journal, pp. 88-109, January 1951

63. ----- Advance Design System , www.home.agilent.com
64. Bahr, A., J., 'Active Network Techniques for Improving Antenna Performance', Technical report P-13058-EL, Stanford Research Institute, May 1977
65. Hrabar, S., 'Active Dispersionless Metamaterials – a Path towards Broadband Cloaking ', Proc. on 2009 REME Workshop , pp. 108-130, Madrid 2009
66. Hrabar, S. , Krois, I., Kiricenko, A., 'Towards Active Dispersionless ENZ Metamaterial for Cloaking Applications' , Metamaterials, Vol. 4 No. 2-3, pp. 89-97. August-September 2010
67. Hrabar, S., Krois, I., Bonic, I., Kiricenko, A., 'Experimental Investigation of Active Broadband ENZ Transmission line', Metamaterial Congress 2010, pp. 15-17, Karlsruhe 2010
68. Hrabar, S., Krois, I., Bonic, I., Kiricenko, A., 'Basic Concepts of Active Dispersionless Metamaterial based on Non-Foster Elements', Proc. on ICECOM 2010, Dubrovnik, Croatia, pp. S03P05-1-S03P05-4, 2010
69. Bilotti, F. , Tricarico, S. , Vegni, L., 'Plasmonic Metamaterial Cloaking at Optical Frequencies', IEEE Trans. on Nanotechnology' Vol. 9, No. 1, pp. 55–61, Jan. 2010
70. Withayachumnankul, W., Fischer, B.M, Ferguson, B. , Davis, B.R. , Abbott, D. , 'A Systemized View of Superluminal Wave Propagation', Proc. of IEEE, Vol 98, No. 10, pp. 1775-1786, October 2010
71. Siddiqui, O.F , Mojahedi, M., Eleftheriades, G.V, ' Periodically loaded transmission line with effective negative refractive index and negative group velocity', IEEE Trans. on Antennas and Propagation, Vol. 51, No.10, pp. 2619-2615, October 2003
72. Erickson, S.J. Khaja, Mojahedi, M., 'Time- and Frequency-domain Measurements for an Active Negative Group Delay Circuit', Proc. on IEEE AP-S 2005, pp. 790-793, Washington DC, July 2005
73. Hrabar, S., Krois, I., Bonic, I., Kiricenko, A., Munoz, E., 'Broadband Epsilon-Near-Zero (ENZ) and Mu-Near-Zero (MNZ) Active Metamaterial', Final Report for Contract FA 8655-10-1-3030, EOARD/AFRL, August 2011
74. Hrabar, S., Krois, I., Kiricenko, A., Bonic, I., 'Negative capacitor paves the way to ultra-broadband metamaterials', Applied physics letters, Vol. 99, No. 25, pp. 25403-1-25403-4, 2011
75. Hrabar, S., 'Active non-Foster Metamaterials: From Intriguing Background Physics to Real-world Application', A plenary talk, Proc. on Metamaterials Congress, pp. 601-603, Sankt Petersburg, 2012
76. Hrabar, S., Krois, I., Kiričenko, A., Bonić, I., Muha, D., 'New Research Directions in Broadband Active non- Foster RF Metamaterials', Proc. on 6th European Conference on Antennas and Propagation (EUCAP), pp. 312-331, Prague, 2012
77. Hrabar, S., Sipus, Z., Malcic, I., 'Broadening of Cloaking Bandwidth by Passive and Active Techniques', A book chapter in 'Transformation Electromagnetics and Metamaterials', (ed. D. Wernier and D. H. Kwon), Springer 2013
78. Hrabar, S., Krois, I., Kiricenko, A., Bonic, I., 'On Bandwidth of Transmission-line-based and Inclusion-based Non-Foster ENZ Metamaterials', Proc. on IEEE AP-S, Orlando 2013

79. Ugarte-Muñoz, E., Hrabar, S., Segovia-Vargas, D., Kiricenko, A., 'Stability of Non-Foster Reactive Elements for use in Active Metamaterials and Antennas', IEEE Trans. on AP-S, Vol. 60, No. 7, pp. 3490-3494, 2012
80. Hrabar, S., Krois, I., Kiricenko, A., Bonic, I., 'Ultra-broadband simultaneous superluminal phase and group velocities in non-Foster epsilon-near-zero metamaterial', Applied physics letters, Vol. 102, No. 5, pp. 4108-1-4108-5, 2013
81. Hrabar, S., Zidar, D., Krois, I., 'Stability Analysis of Superluminal Metamaterial Transmission Line with Realistic Non-Foster Negative Capacitors', Automatika – Journal for Control, Measurement, Electronics, Computing and Communications, Vol. 53, No. 1, pp. 31-37, 2012
82. Debogovic, T., Hrabar, S., Perrisseau-Carrier, J., 'Broadband Fabry-Pérot radiation based on non-Foster cavity boundary', Electronics letters, Vol. 49, No. 4, pp. 239-240, 2013
83. Hrabar, S., Krois, I., Mostarac, F., Kiricenko, A., Bonic, I., 'Practical Realization of Broadband Reconfigurable non-Foster ENZ /MNZ/DPS Metamaterial', IEEE URSI Antennas and Propagation 2013, (ed. W. Parveen), pp. 133.7-133.7, Orlando, 2013
84. Ramaccia, D., Bilotti, F., Toscano, A., Hrabar, S., 'Restoring the Radiating Performances of Shortened Horn Antennas over a Broad Frequency Range', IEEE URSI Antennas and Propagation 2013, (ed. W. Parveen), pp. 964-965, Orlando, 2013
85. Hrabar, S., Krois, I., Bonic, I., Kiricenko, A., 'Superluminal Propagation in Metamaterials: Anomalous Dispersion versus Non-Foster Approach', Proc. on 7th International Congress on Advanced Electromagnetic Materials in Microwaves and Optics – Metamaterials 2013, (ed. S. Tretyakov), pp. I.2-1-I.2-3, Bordeaux, 2013
86. Malcic, I., Hrabar, S., 'From Planar Transmission-line-based Cloak to Volumetric Cloak', Proceedings on 7th International Congress on Advanced Electromagnetic Materials in Microwaves and Optics – Metamaterials 2013, (ed. S. Tretyakov), pp. IV.1-1-IV.1-3, Bordeaux, 2013
87. Okorn, B., Hrabar, S., Krois, I., 'Investigation of Basic Physics of Non-Foster Negative Capacitance in Time Domain', Proceedings ELMAR-2011, (ed. J. Bozek), pp. 373-376, Zadar, 2013
88. Zaluski, D., Muha, D., Hrabar, S., 'Practical Aspects of DB Metasurfaces- A Brief Review', IEEE URSI Antennas and Propagation 2013, (ed. W. Parveen), pp. 316-317, Orlando, 2013
89. Malčić, I., Hrabar, S., 'Numerical Analysis of Bandwidth of 2D Cylindrical Anisotropic EM Cloaks', Proc. ELMAR-2012, (ed. J. Božek, M. Grgić), pp. 317-320, Zagreb, 2012
90. Muha, D., Hrabar, S., Krois, I., Kiričenko, A., Bonić, I., Zaluški, D., 'Numerical Analysis of Non-Foster-based Leaky-wave Antenna', Proc. ELMAR-2012, (ed. J. Božek, M. Grgić), pp. 325-328, Zagreb, 2012
91. Muha, D., Hrženjak, N., Hrabar, S., Zaluški, D., 'RF ENZ Dielectric Waveguide', Proc. on Metamaterials 2012, pp. 360-362, Sankt Petersburg, 2012
92. Muha, D., Mlakar, M., Hrabar, S., Zaluški, D., 'Practical Realization of Isotropic RF Replica of Plasmonic Sphere', Proc. on 6th European Conference on Antennas and Propagation (EUCAP), pp. 123-127, Prague, 2012
93. Okorn, B., Hrabar, S., Sancho-Parramon, J., 'Circuit-theory Interpretation of Optical Multilayer ENZ Metamaterial with Enhanced Bandwidth', Proc. ELMAR-2012, (ed. J. Božek, M. Grgić), pp. 329-332, Zagreb, 2012

94. Zaluški, D., Muha, D., Hrabar, S., 'Towards Experimental Investigation of Metamaterial - based DB Surface in Waveguide Environment', Proc. on 6th European Conference on Antennas and Propagation (EUCAP), pp. 256-260, Prague, 2012
95. Zaluški, D., Muha, D., Hrabar, S., 'Experimental Verification of Metamaterial-based DB Unit Cell', Proc. ELMAR-2012, (ed. J. Božek, M. Grgić), pp. 321-324, Zagreb, 2012
96. Zaluški, D., Muha, D., Hrabar, S., 'Practical realization of DB unit cell', Proc. on Metamaterials 2012, pp. 499-501, Sankt Petersburg, 2012
97. Zidar, D., Hrabar, S., Krois, I., 'Stability Analysis of Active Broadband ENZ Line', Proc. ELMAR-2012, (ed. J. Božek, M. Grgić), pp. 313-315, Zagreb, 2012
98. White, C.R., May, J.W., Colburn, J.S., 'A variable negative-inductance integrated circuit at UHF frequencies', IEEE Microw. Wireless Compon. Lett., Vol. 22, No. 1, pp. 35–37, January 2012
99. Gregoire, D.J., White, C.R., Colburn, J.S., 'Wideband artificial magnetic conductors loaded with non-Foster negative inductors', IEEE Antennas Wireless Propag. Lett., Vol. 10, pp. 1586–1589, 2011
100. D. F. Sievenpiper, "Superluminal waveguides based on non-foster circuits for broadband leaky-wave antennas," IEEE Antennas Wireless Propag. Lett., vol. 10, pp. 231–234, 2011.